UC Berkeley
UC Berkeley Electronic Theses and Dissertations

Title
Controlling Crystallization and Transport in Metal–Organic Frameworks

Permalink
https://escholarship.org/uc/item/5nz8w40t

Author
Colwell, Kristen A.

Publication Date
2019

Peer reviewed|Thesis/dissertation

eScholarship.org Powered by the California Digital Library
University of California

Controlling Crystallization and Transport in Metal–Organic Frameworks

by

Kristen A. Colwell

A dissertation submitted in partial satisfaction of the

requirements for the degree of

Doctor of Philosophy

in

Chemical Engineering

in the

Graduate Division

of the

University of California, Berkeley

Committee in charge:

Professor Jeffrey R. Long, Chair
Professor Jeffrey A. Reimer
Professor Ting Xu

Summer 2019

Abstract

Controlling Crystallization and Transport in Metal–Organic Frameworks

by

Kristen A. Colwell

Doctor of Philosophy in Chemical Engineering

University of California, Berkeley

Professor Jeffrey R. Long, Chair

This dissertation documents efforts to control and take advantage of crystallization handles in metal–organic framework synthesis. Understanding fundamental processes during synthesis allows for directed, predictable control over crystallite size and shape, which is demonstrated to play a role in intracrystalline diffusion.

Chapter 1 first introduces a summary of crystallization and transport in porous materials, including classical and non-classical models of crystallization, homogeneous and heterogeneous nucleation, and mass transfer resistances. The application of these concepts to metal–organic frameworks is presented alongside common synthetic strategies, coordination modulation and other strategies to control crystallite size and shape, and the potential for non-coordinating bases and buffers to help alleviate some complicating factors common to framework synthesis. Finally, because crystallite size and shape can control intracrystalline path lengths, an introduction to mass transfer resistances is given, including intracrystalline diffusion. Different methods of measuring diffusion in porous materials are presented, including the technique applied in this work, zero-length column chromatography (ZLC).

Chapter 2 details success in deconvoluting solution equilibria during hydrothermal metal–organic framework synthesis. The use of non-coordinating bases and anions allows for generalizable increase in crystallite size. Further, non-coordinating buffers may be used during synthesis to add or subtract individual coordinating anions at a given pH. This strategy allows for tunable and predictable control over aspect ratio in a one-dimensional metal–organic framework.

Chapter 3 describes the discovery and utilization of interfacial effects during hydrothermal synthesis to control crystalline phase and size. Controlling the interface between reaction vessel and solution via silanization is found to decrease morphological distribution, change the phase produced for stock solutions, and in some cases, increase crystallite volume by several orders of magnitude.

Chapter 4 details the assembly and usage of a ZLC instrument capable of differentiating between different mass transfer resistances. Design considerations and instrument improvements are described. The instrument is used to probe CO_2 diffusion within very large crystallites (up to 700 microns in length) of Zn_2(dobdc), where surface resistances and defects are proposed to account for a lower diffusivity measured via ZLC versus pulsed-field gradient NMR. Synthetic control over Co_2(dobdc) path length is demonstrated to bring about improved mass transfer resistances via path length control for the industrially important molecule *m*-xylene.

This dissertation is dedicated to my parents, Ellen and Bob Colwell.

Table of Contents

List of Figures

Chapter 1

Chapter 2

Chapter 3

Chapter 4

List of Tables

Chapter 2

Chapter 4

Acknowledgments

"Look, I made a hat / Where there never was a hat"
-Stephen Sondheim

I came across the song "Finishing the Hat" from the musical "Sunday in the Park with George" as I was writing this dissertation. Sondheim captures perfectly the feeling of stasis, of watching and yet feeling removed from everything around you as you finish some piece of art or writing. It can be easy to feel, as George describes in the song, that the world shrinks to include just you and the vortex of your work. The more I reflect on this, the more it becomes apparent that this sense of isolation is a lie. I have never been alone in this process. The research and the progress I have made has been supported by an enormous network of people. It is a heady and difficult task to attempt to thank everyone who has been essential in getting to this point, and yet I must try.

First, I want to thank Professor Jeffrey Long, my advisor of the last several years. I showed up a naive first year excited at the prospect of doing research that could help save the world. He directed me to projects that would challenge me and help to attack this goal from a fundamental side, and he did so with graceful guidance. He has trained me not only how to do research but how to ask the right questions and, equally crucial, how to communicate the results. I can only strive to be as knowledgeable as he is in such a diverse area of interests. I am proud to have been a member of his group and proud of the standard of research that he enables and demands. Jeff does an exceptional job assembling bright and creative people, and I have been humbled to be around them (more on this later). I also want to thank his wife, Jen, who is one of the kindest people I have ever met, with a rare gift for putting anyone at ease.

Second, I would like to thank my parents, Ellen and Bob Colwell. I have no idea where they find the mind-boggling reserves of love, support, and encouragement they have given me my entire life. I have always known that they each believed I could do absolutely anything, which is how I came to believe I could do anything. My dad, a dazzlingly competent scientist and engineer, always took my questions seriously and taught me the value in building things and doing honest science: at the end of the day, what you build must work. I am an engineer because of his direction and advice and because I observed firsthand from him that engineers can change the world and enact change on a global level. My mom, equally brilliant, has always, always been there for me. From helping with math problems to editing writing, she is an exceptionally empathetic polymath. When I have needed her, she has flown even across the country at the drop of a hat. It is to them that I dedicate this dissertation.

I am also indebted to my siblings. My sister, Kelly, has been a role model for me my entire life. She cares more deeply about helping others than just about anyone I have ever met, and she is exceptionally smart and well-spoken. I have had the good fortune of living with her and her wife, Sheryl, for several years now as they earn their own doctoral degrees in theology. I am so happy to have been able to spend this much time with them, and I will deeply miss both of them, not to mention the coffee they brew every morning, without which this dissertation may never have been written. My brother, Ken, has also been a huge role model for me. I remember thinking when I was growing up that I would never be as cool, as well-liked, or as funny as he is. As it turns out, I was correct; these things are all still true. Still, it sets a standard for which to strive! He has given me so much advice and counsel throughout my life and throughout graduate school, and I would not be the same without it.

Other important role models for me in graduate school have included Professor Jeff Reimer, who served on my qualifying committee and read this thesis. He does an exceptional job as departmental chair and I have always felt supported by him and the department in general. His enthusiasm and cheer are an inspiration to me, and my work in diffusion has included extensive collaboration with a post-doctoral scholar in his research group, Alex Forse. Professors Enrique Iglesia, Clay Radke, and Berend Smit were instrumental to me learning the fundamentals of chemical engineering. I would like to thank Professors Angelica Stacy, Roya Maboudian, and Alex Katz for serving on my qualifying committee and giving excellent suggestions. I thank Professor Ting Xu for reading this dissertation, and for the use of her dynamic light scattering instrument.

In college I had several excellent mentors, both within engineering and without. Professor B. Stuart Trembly was one of the best engineering teachers I ever had. He introduced me to the concept of engineering analogy in distributed systems and fields. I use these concepts (in particular, three-dimensional transport as a result of an applied gradient) every day. Professor Rachel Segalman let me join her lab for a semester in my third year, which introduced me to the chemical engineering department at UC Berkeley and convinced me to come here. Dr. Albert Epshteyn introduced me to inorganic chemistry and let me work in his lab for several summers, setting me up to tackle a project at the intersection of engineering and chemistry (and, in getting me to build a freezer, helping me develop some hands-on engineering!).

I also had several role models outside of engineering and chemistry who have deeply influenced me, particularly in music. Professor Steve Swayne was one of my favorite teachers I have ever had. It is because of him that I have a deep and abiding love of music theory, and that I have come to understand that emotion brought about by music is to be cherished and celebrated, not hidden. Professor Kui Dong helped me develop a sense of color and originality in music composition. I owe my working knowledge of orchestration to the mentorship of Professor Michael Casey. Professor Bob Duff was one of my closest mentors during my time at Dartmouth. I would not be the same person without the deep and abiding love of Bach he inspired. While these topics in music may seem tangential, they are not. When I first started thinking about crystal nucleation, I saw it in music, in motifs, in notes appearing and disappearing. Participating in the arts and music does not detract from time going to scientific research; rather, the arts enhance engineering and science and alter them, and give them meaning.

Lastly, Dr. John Gorman taught me the calculus that is a part of this dissertation. Dr. Darrell Feebeck was the first chemistry teacher I had, without whom I might've chosen an entirely different field. Finally, to Paul Klausenburger, who taught me history: you taught me context and conciseness. Thus, I will stop there.

I have many people at UC Berkeley to thank, the first of which are fellow chemical engineers. Sudi Jawahery has not only been an extremely influential collaborator but also one of my very best friends and a source of constant support. She was involved in nearly every aspect of my research from a computational perspective and provided invaluable perspectives on the processes and equilibria involved. Jamie Lincoff has always been willing to meet and listen to anything I have going on. I consider both Julie Rorrer and Kyle Diederichsen to be among my closest friends and have leaned on them separately and together for emotional support many times over the years. The other members of my class, particularly in our first year together, have also helped me immeasurably in adjusting and learning chemical engineering. I have no doubt they will each go on to do amazing things, just as they have during graduate school.

When I started looking for a lab to join in the fall of 2014, I immediately found a home in the Long Group. My year mate, Rebecca, is an exceptionally competent, intelligent, and kind scientist.

She has always been there to help me, and the lab is not the same now that she has left. There was an exceptionally great group of senior students and post-docs around when I joined the lab. I cannot name them all, lest I spend several chapters here, but they were all immensely supportive and helpful. Dana Levine and Lucy Darago helped guide me and keep me sane. Dana showed me the stock room, listened to me cry, and taught me the usefulness of precise volumetric measurements. Miguel Gonzalez, a brilliant and inexhaustible chemist, took it upon himself to help guide me and went out of his way to mentor and advise. Nearly everything in this dissertation has a topic he's helped me develop in my mind. I have leaned on the year above me, Julia Oktawiec, Mercedes Taylor, and Jon Bachman, to help guide me in my time here. Julia is an untiring source of advice, talking, and cat pictures. Mercedes helped me get through every single subgroup and group meeting until she left. Jon recruited me to the lab in the first place, started the crystallization project, and always provided excellent perspective on what really mattered. I thank Katie Meihaus for her editorial help. Both Phill Milner and Jeff Martell were excellent sources of discussion on sorption kinetics. It has been fun watching them mentor within the Long group and start their own labs. Phill has always been game to work through organic synthesis, discussion of kinetics, alcohol, or just about anything else. Jeff M. was a true joy to work with. I have rarely known anyone so dedicated, competent, and determined to be precisely correct. Both, in their own way, make among the finest professors I've ever met and any student who joins either of their labs will have been lucky to do so.

I also benefitted greatly from the help and support of the students and post-docs who joined the lab after I joined. It has been a real joy watching Ever Velasquez progress and getting to know him. He keeps me sane through subgroup and group meetings and will drop whatever he's doing to grab coffee. That is true friendship. I'm extremely excited by the continuing addition of chemical engineers to the lab, including Surya Parker, Adam Uliana, and Katie Engler. In particular, I want to thank Matt Dods, who has been unfailingly helpful and enthusiastic about continuing kinetics work: I am extremely confident I've left the work in the best possible hands. I can't wait to see direct air capture come about through his work, or a change in the political powers that be in the US, or whatever he puts his mind to. I cannot imagine the lab without the presence of Eugene Kim or David Jaramillo, who are both true sources of joy in my day-to-day life. David gives excellent advice ("oh, something on the instrument is jammed? Have you tried just pushing way harder?") when he is not making the resident group room puppy mad with joy. Eugene, apart from having some sort of magic grip strength the world has never seen before, is a dedicated and thoughtful scientist as well as an invaluable member of team coffee and a discerning craft beverage consumer.

I have loved getting to know and hang around with Naomi Biggins and Maria Paley, who are as excellent sources of support as they are excellent people. I want Naomi to be there in every workplace I ever have. As for Maria, the girl keeps it real. I'll miss her. I am having a hard time imagining my future life without a daily burst of new ideas and enthusiasm from my deskmates in the corner of Lewis 210, Colin Gould and Ryan Murphy. Ryan may be the strangest and most creative mind I've come across in chemistry, and that's saying something. Colin is an exceptional scientist and somehow always knows what's happening, gossip-wise. Henry Jiang has been an incredibly useful source of cat pictures, advice, and unprompted political treatises, although he never changes web browser mouseovers. This is my public shaming of you, Henry. Mike Ziebel is a scarily competent inorganic chemist, and I'm excited to see where he goes in the future. Really, every graduate student who's been in the lab at the same time has been an utter delight to be around. What a group!

I'm grateful that someone as bright, enthusiastic, and well-balanced as Megan Jackson is taking over crystallization. I couldn't have hand-picked someone better if I tried. My only regret is not overlapping with her more before I graduated. Although I am extremely grateful for the support and enthusiasm of basically all of the post-docs who have come through the lab, a few of them in particular have been extremely helpful. Alex Forse is a brilliant and motivated collaborator with whom it has been an utter pleasure to work. He also has excellent spa recommendations. I've also really enjoyed getting to know Ben Snyder and his extremely adorable puppy Ginger, without whom this dissertation may never have been finished. Therapy dog indeed. Finally, Hiroyasu Furukawa is a talented researcher and manager, and we have all benefitted enormously from his presence in lab.

I also want to name-drop a few of my very close friends, including Karina Dracott, Hilary Gross, Torrey Barrett, and Dia Hazra, for their unfailing love and support not only through this process but throughout my entire life. You are all my heart and soul.

The College of Chemistry and the Department of Chemical and Biomolecular Engineering have both been unfailingly helpful during my time here. Carlet Altamirano is an absolute godsend. Jim Breen helped consistently with the bubbler in the zero-length column work. Several times, I had to go to the machine shop in a panic while building the ZLC instrument. I thank Kenna Eames for her administrative assistance in the latter half of my thesis. Without the administration and technical staff in the College of Chemistry, none of us would ever get any research done.

Although I acknowledge the excellent scientists and project leaders at ExxonMobil in every chapter, it is also necessary to thank them here. The project in its current state would certainly not exist without their funding, support, suggestions, and discussions. Both Simon Weston and Joe Falkowski have been exceptional research partners and program leaders throughout my graduate career. They both brought different, invaluable perspectives that may not otherwise have found their way into the crystallization and diffusion work presented here. I also deeply appreciated the opportunity to be able to go on location and give talks to the scientists and engineers there, who I found to be sharp, motivated people truly interested in science. In all, the experience helped me decide to go into industry, hopeful that I will find a similar cohort of bright, motivated people hoping to effect change in the world.

Finally, to my partner of several years, Rodi Torres-Gavosto: I certainly would not be here without you and my work would not have been the same without your support, suggestions, and literal help. I hope you are proud of what we have accomplished, where we have gone, and where we will go in the future. I certainly am.

To everyone else who has been there and helped during this process: thank you. I could not have done it without you.

Chapter 1: Introduction to Crystallization and Transport Properties of Metal–Organic Frameworks

1.1 Introduction

Metal–organic frameworks are hybrid organic-inorganic crystalline solids with high permanent porosity.[1,2] The materials feature zero-dimensional inorganic clusters or one-dimensional inorganic chains linked together by multitopic organic ligands to create scaffold-like structures with resultant open pore space. Through judicious choice of different metals or clusters with different ligands, frameworks can have a wide range of internal pore sizes, shapes, and chemical functionalities available. As a result, the possible applications of the materials are equally vast, including areas as diverse as gas and liquid separations,[1–4] energy storage,[5–9] catalysis,[10–13] biomedical applications and drug delivery,[14–17] and gas sensing.[18–22]

Metal–organic frameworks have the potential to be disruptive technologies in several areas related to the global use of energy. The separation of mixtures of chemicals with similar physical properties into pure or purer forms uses 10-15% of global energy and, in doing so, generates enormous emissions of molecules known to contribute to climate change.[23] Creating and improving ways to cut down on the amount of energy needed to separate industrial chemicals, to capture greenhouse gases from streams that would otherwise add to rising atmospheric levels, and to store clean-burning fuels such as hydrogen in a volume-efficient manner is of vital importance. Metal–organic frameworks are among the most promising materials for all of these energy-centric applications.[4,24,25] However, to fulfill their potential and help to bring about the massive industrial change needed to ameliorate the effects of climate change, these materials must be produced and tailored for applications in large scale. Understanding their formation is a crucial step to achieving this goal.

One privileged group within the field of metal–organic frameworks consists of materials with coordinatively-unsaturated metal ions, also known as open-metal sites.[26,27] In these materials, one or multiple metals within the inorganic node has a solvent bound at a coordination site post-synthesis. For sufficiently stable frameworks, these solvent molecules may be removed through the application of heat and vacuum without framework collapse, leaving a metal center with a coordination site exposed. This exposed highly polarizing site can strongly adsorb guest molecules. Molecules may also be grafted onto these open-metal sites post-synthetically to create chemical functionalities capable of selective gas adsorption; these materials are among the most promising for the capture of carbon dioxide in post-combustion processes.[4,28–30]

The material with the highest density of these open metal sites is the M_2(dobdc)(M = Mg, Mn, Fe, Co, Ni, Cu, Zn, Cd; dobdc^{4-} = 2,5-dioxido-1,4-benzenedicarboxylate) family of materials (Fig. 1.1).[31–34] The structure features helical chains of metal atoms, each of which has one octahedral site available for guest molecule polarization. These chains are bridged by the rigid aryl-based linker, dobdc^{4-}, leading to one-dimensional hexagonal pores. Because of its high density of metal sites, M_2(dobdc) and related frameworks have been examined as potential materials for catalysis,[10,35–37] energy storage,[38–42] gas and liquid separations,[24,43–46] drug delivery,[47] and gas sensing:[48–50] in short, as model materials that span the gamut of metal–organic framework applications.

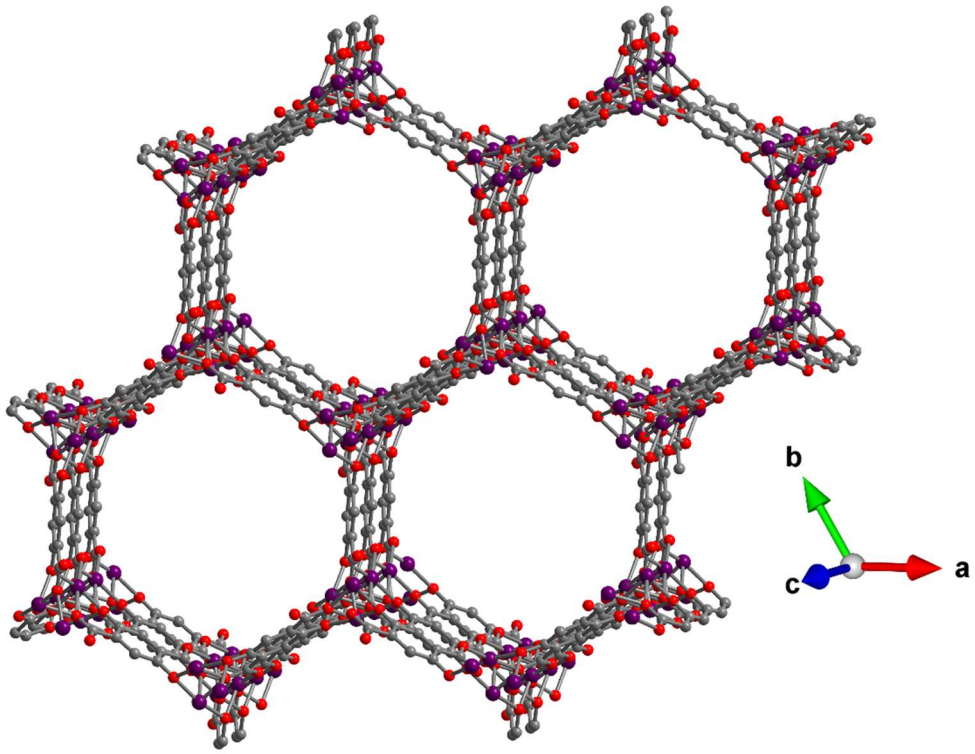

Figure 1.1. The structure of M_2(dobdc), a prototypical metal–organic framework. The hexagonal one-dimensional pore, aligned with the c-direction, is lined with coordinatively-unsaturated metal centers, one at each vertex. Grey atoms are carbon, red atoms are oxygen, and purple atoms are the metal. Hydrogens omitted for clarity.

1.2 Classical and Non-Classical Models of Crystallization

Crystallization History. As metal–organic frameworks are crystalline solids, the process of their assembly requires precursors to self-assemble into a well-defined crystal lattice in order to minimize their total energetic state. This process is known as crystallization. The historical practice of crystallization predates any theoretical understanding of the process; in fact, the oldest chemical engineering unit operation is generally considered to be a crystallizer, used in the process of evaporating sea water and natural brine to produce salt.[51] These early crystallizers can be dated to 2700 B.C. with a Chinese print demonstrating a shallow open tank evaporator. Similar structures are described in Pliny's "Naturalis Historia" in places such as Crete and Egypt, using solar heat to evaporate water and concentrate the solution until salt precipitated.

Crystallization is now a wide-spread process for separation, purification, and production of materials used in industries ranging from semiconductor processing to pharmaceuticals to commodity and specialty chemicals.[52]

Crystallized products must fulfill specific requirements such as specific polymorph or phase, structure stability and shelf-life, and crystallite morphology (geometric shape of each crystallite) and size distribution. All aspects of the crystallites produced are determined by the chosen (or inadvertent) crystallization conditions.[53]

While most industrial crystallizations are from solution,[52] other processes can include crystallization from melts or from neat liquid, crystallization from the vapor phase, or solid-solid conversion processes such as ball-milling. In each case, the process is a phase transition from a state of high free energy to one of lower free energy in the form of a crystalline solid. For solution-based crystallizations, the free energy of the initial solution phase is greater than the sum of the free energies of the crystalline lattice and the final solution phase.[54,55] In this case, crystallization can proceed spontaneously.

Precipitation Thermodynamics. In solution, the driving force which causes crystallization to occur is typically described as supersaturation, where above a critical threshold of solute the material will spontaneously precipitate. A derivation of this concept is a useful exercise in anticipation of applying these concepts in the context of metal–organic framework formation. The change in free energy and the change in chemical potential are related to the activity products.[53,56–58]

Consider the precipitation reaction:

$$a\mathrm{A} + b\mathrm{B} + \cdots + n\mathrm{N} \rightarrow \mathrm{A}_a\mathrm{B}_b \ldots \mathrm{N}_n$$

where components A through N may be ions, reactants, or even metal and ligand. The activity product of the reactants AP and the equilibrium constant K_{sp} are given by:

$$AP = \mathrm{A}^a\mathrm{B}^b \ldots \mathrm{N}^n$$
$$K_{\mathrm{sp}} = [\mathrm{A}]_e^a[\mathrm{B}]_e^b \ldots [\mathrm{N}]_e^n$$

where the subscript e denotes equilibrium. Accordingly, the free energy of solution per molecule Δg_{sol} and the change in chemical potential $\Delta\mu$ are:

$$\Delta g_{\mathrm{sol}} = -k_{\mathrm{B}}T\ln K_{\mathrm{sp}}$$
$$\Delta\mu = k_{\mathrm{B}}T\ln AP - \Delta g_{\mathrm{sol}} = K_{\mathrm{sp}}T\ln\left(\frac{AP}{K_{\mathrm{sp}}}\right)$$

where T is the absolute temperature and k_{B} is the Boltzmann constant. The supersaturation σ is then directly related to the chemical potential in the following way:

$$\Delta\mu = k_{\mathrm{B}}T\ln\sigma$$
$$\sigma \equiv \left(\frac{AP}{K_{\mathrm{sp}}}\right)$$

In this way, the supersaturation relates directly to the driving force. For single-component crystallization, the precipitation may be easily described in terms of the free energy of formation versus the free energy of reactant solvation. For most cases, solution activities are well represented by concentrations. In some cases, σ may be defined as $(C/C_e) - 1$, where C is concentration and C_e is the equilibrium concentration. This uses the common understanding for single-component precipitation where saturation is the amount of solute that may be dissolved in a solvent at a given temperature. Above this level (supersaturation), precipitation will proceed spontaneously, with kinetics dictated by how much more solute is dissolved relative to what is stable in solution.

Note that this definition requires the comparison of the reactant concentration at equilibrium to the activity product of the reactants. A full accounting of the potential inaccuracies using this route for any binary system is provided by Mullin and Sohnel.[56] The common shorthand in metal–organic framework formation literature is to refer to monomer concentration to rationalize crystallization behavior, which is imprecise given that at least two components must combine in ionic or covalent interaction to form the base structure of any metal–organic framework. The use of monomer in this context then suggests that clusters or combinations of metal and ligand are present in solution and add to a crystallite as a single growth unit. It is particularly important to remember that the thermodynamic definition for a precipitation refers to the equilibrium expression of all components and only those components in solution. The solubility of a single reactant refers instead to the precipitation of just that one component from solution and is not the correct parameter to predict crystallization of a multicomponent solid.

Homogeneous Nucleation and Growth. Classical models use two processes to describe a first-order phase transition, such as crystallization. The following model is that of Gibbs-Thomson. Nucleation occurs via the formation of small embryos of the new phase within the larger volume of the old phase. As described above, since the driving force is a chemical potential gradient, the free energy of the product formed is lower than that of the reactants in solution for spontaneous crystallization. This is only strictly true of the bulk phase. At the interface between the solution and the new phase formed, the local energetics are significantly higher, because the molecules at the surface are not bound to their neighbors in all three directions. At the first moments of crystalline formation, most of the molecules in the new phase are on the surface of the crystallite, causing the phase to go through a local maximum in energy. As a result, these nuclei are unstable; adding molecules to the structure causes an increase in the free energy. However, at sufficiently large size, the contribution of the lower bulk energy outweighs the high interfacial energy, and crystallites tend to continue growing. As displayed in Figure 1.2, the balancing of these two free energy contributions leads to the existence of an intermediate size at which the free energy is maximized and either growth or dissolution lowers the energy; this is known as the critical size.

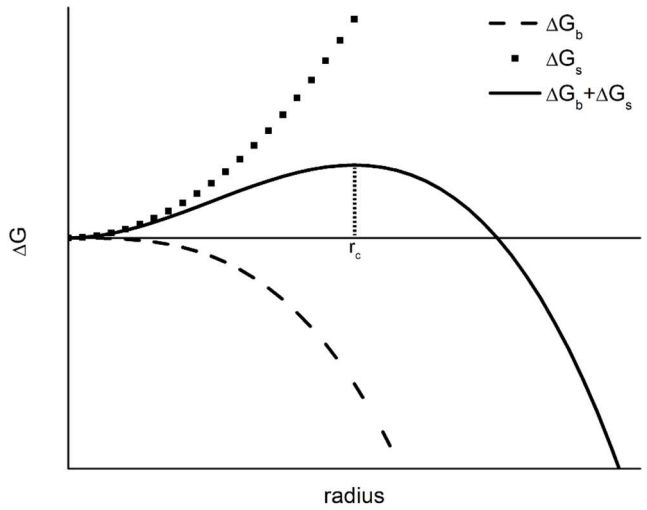

Figure 1.2. A visualization of Gibbs free energy during nucleation. The sum of surface and bulk free energy terms reaches a positive maximum at a radius corresponding to the critical size (labeled r_c). Below this radius, embryos are likely to redissolve; above it, embryos continue growing.

The second process, growth, refers to the adding of reactant molecules to the surface of a crystallite. Growth from solution occurs because the flux of molecules attaching to this surface exceeds the flux of molecules detaching. It is thus a function of many factors, including the concentration of reactants in solution, the exchange rate of molecules at surface sites, and the strength of bonding. Another way of describing equilibrium in crystal growth is the point at which the two fluxes are equal. For covalent frameworks, the bonds between metal and ligands can be very strong, leading to difficulty in applying the thermodynamic equations in the section prior: equilibrium descriptions require equilibrium conditions, and the reactant concentrations present at equilibrium can be vanishingly small. Another way to disrupt growth would be to introduce molecules that can interfere with the incorporation of molecules in flux to the surface, creating additional barriers to monomer addition; this strategy, known as coordination modulation, will be described in a subsequent section.

Heterogeneous Nucleation. The classical model of nucleation assumes that the new phase begins homogeneously, or within the matrix of the old phase. However, if solid surfaces or foreign matter are present, nucleation of the crystalline phase can begin in contact with either of these rather than homogeneously from solution in a process known as heterogeneous nucleation. The barrier to nucleation is that of creating an interface between the old phase and the new phase; often, the interfacial energy between a crystal and a solid substrate is lower than that created between the crystal and the solution, because molecules can form often stronger bonds with the surface than with solvent molecules.

Under the circumstances that either the atomic structure of the surface matches that of the nucleating particle or the substrate has a set of chemical functionalities promoting strong bonding to the nucleus, the total interfacial energy can become significantly lower by including interactions between the substrate and the nucleating particle. Examples of this type of nucleation are common across many different materials formation processes, including pharmaceuticals,[59,60] proteins,[61–63] polymers,[64,65] semiconductors,[66,67] and biomineralization.[53,68] Indeed, heterogeneous nucleation is a prominent feature in not just crystallization but in all first-order phase transitions, including the formation of carbon dioxide bubbles from solution.[69] Further, the presence of heterogeneous nucleation can impede the homogeneous pathway. Nucleation events lower the solution concentration of the precipitating species. As the probability of nucleation is related to that concentration, for a fixed volume, lowering the concentration through heterogeneous pathways decreases the likelihood of homogeneous precipitation. For this reason, heterogeneous nucleation is posited to account for the vast majority of nucleation from solution.[70]

Description of Some Useful Crystal Characteristics. The resulting crystalline products are characterized first by their repeating atomic order in three dimensions. A technique such as X-ray diffraction (XRD) may be used to probe this atomic order. X-ray diffraction is the elastic scattering of X-ray photons by atoms in a periodic lattice. The in-phase scattered X-rays give rise to constructive interference when conditions satisfy Bragg's Law ($n\lambda = 2\ d \sin\theta$, where λ is the X-ray wavelength, d the lattice spacing, and θ the angle of diffraction).[71,72] The generated diffraction pattern then has a reciprocal Fourier transform relationship to the crystalline lattice and thus the unit cell, the base repeating unit within the crystal.

Each crystallite consisting of a given phase then additionally has spatial characteristics of particle size and shape. The geometric shape of the crystallite is also known as the morphology or the crystal habit.[53] Both size and shape have myriad effects on materials usage which differ per material and per application.[73–77] Modification of crystal morphology can greatly influence the

mechanical properties, particularly for elongated habits (needle- or rod-like). Further discussion of the effect of crystallite size and shape for porous materials may be found in Section 1.4.

1.3 Metal–Organic Framework Synthesis

At the simplest level, all metal–organic frameworks can be described as Lewis acidic metal ions or clusters bridged by Lewis basic ligands. The syntheses themselves at bare minimum require the combination of the metal precursors with the ligands to be incorporated in the framework. These reactions are overwhelmingly done in solution, although not exclusively. Other synthetic methods of combining metal cations with ligands include vapor-phase deposition,[78–80] mechanochemistry,[81–83] and crystallization from melts.[84] The category of solution-based synthesis includes a broad range of methods and materials, including solvothermal synthesis,[85–87] hydrothermal synthesis,[88–90] electrosynthesis,[91,92] and various subsets, including sonochemical synthesis[93,94] and microwave synthesis.[95–98]

For nearly all reported frameworks, the organic ligands behave as Brønsted-Lowry acids and/or bases during synthesis. Commonly, the protonation state of the ligand as added to the synthesis is not identical to the state as incorporated into the framework. For example, for the framework M_2(dobdc), the ligand has four separate pK_a values, corresponding to the two carboxylic acid groups and the two phenolic groups. In solvothermal syntheses, the ligand is typically added to the solution mixture as the fully protonated H_4dobdc, where all four protons must be removed according to the framework composition $(M^{2+})_2(dobdc^{4-})$. In room temperature syntheses, the protonation state is generally adjusted through adding either four equivalents of sodium hydroxide[99] or of a different base, such as triethylamine, intending to deprotonate the ligand fully prior to the beginning of framework formation.[100,101] For reactions in which the ligand is fully deprotonated at the beginning of framework synthesis, the product is nanoscale in size and has resultant higher external crystallite surface area, which often leads to differing chemistry than that designed within the pore.[102,103]

The moderation of reaction pH, or pH* in non-aqueous media, can greatly determine synthetic results in framework formation. The solution pH is a description of protonation equilibria with respect to solution species, the solvent, and a reference electrode.[104] In a solvothermal reaction, the acid/base adjustment needed to change the protonation state of the ligand from its initial state when added to that of the ligand in the framework is provided by the decomposition of the solvent, typically, N,N-dimethylformamide (DMF) or N,N-diethylformamide (DEF).[87] DMF and other amide-based solvents will readily decompose at elevated temperatures to yield an amine and either a carbonyl species or a carboxylic acid via thermolysis or hydrolysis, respectively. It is common to include water as a co-solvent with DMF in metal–organic framework synthesis. These solvent choices are generally the result of extensive screening of different combinations.[105] It is likely that including water as a co-solvent changes the solubility of various reactants in solution and also changes the decomposition pathway of the solvent DMF. Since the decomposition pathway dictates the products formed, including the base required to deprotonate Brønsted-acidic ligands, both the composition of the matrix from which embryos of the new phase nucleate and also the rate and availability of the Brønsted base in solution can vary as a function of water in the synthesis.

This complication of co-solvent addition changing both solubility and Brønsted-base availability is but one example of convoluted equilibria in solution, which are at the heart of some of the complexity observed in metal–organic framework synthesis. For a framework assembling

metal ions and ligands out of a solvent, at bare minimum the interactions of both solutes and solvent are required to describe solution dynamics. This diagram is displayed in Figure 1.3. The formation process of the metal–organic framework, while often described as a process of coordination just between the metal cations and ligand, is tempered by the equilibria arising from interactions with the solvent, one of which is the average protonation state of the ligand. The solubility of the metal source as well as the solubility of the ligand are both complex functions of the solvent (and total ion concentration in solution). The solvation of the metal cation is an understudied area of research in phase selection in framework formation, arising from solvent interactions. The solvent can change the coordination geometry of the metal cation in solution,[106–108] which could conceivably lead to differing phase behavior by templating a specific metal cation coordination geometry.

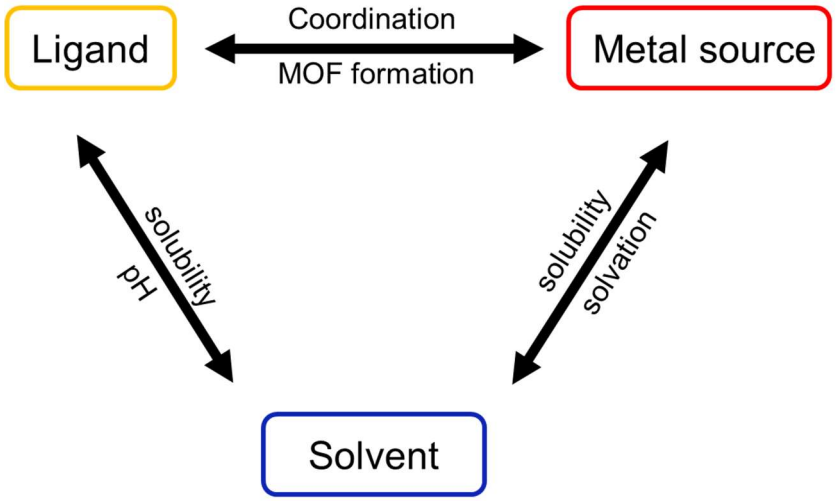

Figure 1.3. A minimum description of solution interactions during metal–organic framework synthesis accounts for multiple equilibria in addition to framework formation, including the precipitation of the ligand or metal source separately, the solvation of the metal source, and the interaction of the Brønsted-Lowry acid/base ligand with the solvent.

Clearly, synthetic variables such as the temperature of the reaction should not only change the energy available to overcome nucleation and growth barriers but also shift chemical equilibria simultaneously. Synthetic choices such as reactant type (i.e., metal salt or metal oxide, initial ligand protonation state) and concentration similarly affect multiple equilibria at once. Using a solvothermal synthesis adds complexity to this base layer of variables intertwined: the hydrolysis of DMF provides both dimethylamine and formate, the latter of which can easily coordinate metal cations. Both solution protonation and coordination are affected simultaneously. The true problem may be stated simply: the variables which may be easily manipulated (such as temperature or solvent) are not the underlying solution handles controlling chemical equilibrium. Each synthetic choice affects multiple equilibria. While results may be plausibly justified after the fact given experimental results, it is difficult to predict which equilibria will matter more for a given system. Indeed, in a review on synthetic strategies, Stock and Biswas find that no general trends can be deduced about the control of crystal size by variation of such compositional parameters.[87] The

inability to predict synthetic results impedes development, optimization, and scale-up of new and current materials.

Coordination Modulation. For the control of the crystallization process, including product variables such as crystallinity and particle size and shape, a number of strategies have been successfully employed in the literature.[87] Some common strategies include compositional or process parameters (as discussed in section 1.3), temperature programs (variation of temperature with time), additives, and surfactant-based methods, such as microemulsions. Of these, the most common by far is the use of additives: additional molecules designed to interfere with some aspect of the crystallization process. This process is generally referred to as coordination modulation, a term coined by Kitagawa et al. wherein molecules are added to the synthetic mixture intended to interfere with the coordination process occurring between the components of the framework.[109] The particle morphology observed of the framework $Cu_3(btc)_2$ (btc^{3-} = 1,3,5-benzenetricarboxylate), also called HKUST-1, changed from octahedral to cuboctahedral to cubic with increasing addition of *n*-dodecanoic acid (colloquially, lauric acid). Like the two linker functionalities, *n*-dodecanoic acid has a carboxylic acid functionality, which Kitagawa et al. proposed could coordinate with the metals on the surface of the crystallite during growth in a competitive fashion.

This strategy has since been extended to control the morphologies of many different framework types and topologies, some of which will be discussed here. Hermes et al. decreased the size of MOF-5 ($Zn_4O(bdc)_3$, bdc^{2-} = 1,4-benzenedicarboxylate) by adding *p*-perfluoromethylbenzoic acid.[110] Cho et al. controlled the aspect ratio of In-MIL-53 via adding equivalents of pyridine (as MIL-53 has no pyridyl functionalities, this is an example of an additive without similar functionality as the ligand).[111] Notably, for the framework HKUST-1 discussed above, Diring et al. used varying amounts of lauric acid to change the size in addition to the morphology.[95] Finally, before being thermolyzed into carbon nanomaterials, Tang and Yamauchi grew Zn_2(dobdc) particles using salicylic acid as a modulator, resulting in nanoscale rods.[112] In several of these examples, both size and shape of crystallites were affected by the addition of modulators.

While the explanation given in all four cases was that the molecules coordinated to the growing crystallite, these modulators are all Brønsted acids capable of participating in protonation equilibria in addition to the coordination equilibria. This necessarily means that their addition influences many solution parameters simultaneously, including pH, ionic strength, and metal coordination in solution: an alternate explanation for the morphological control can be rationalized in terms of acid/base equilibria as easily as coordination equilibria. The complex equilibria displayed in Figure 1.3 becomes yet more complex as additional molecules which play several roles are added.

The role described for these modulators, universally, is that of a capping agent. However, for very similar molecules, this convolution leads to results such as the following: in Hermes et al.'s example, the addition of a capping carboxylate-based additive made MOF-5 crystallite particles smaller, while in Diring et al.'s HKUST-1 work, the addition of a carboxylate-based additive made crystallite particles bigger. The role of the molecules as capping agents thus does not necessarily predict their effect on resultant crystallite size in an easily generalizable way. A large role in this is likely their influence on multiple equilibria. For example, lauric acid can act as a surfactant due to its long hydrocarbon chain.[113] Further, the two molecules have differing pK_a values and thus change solution pH to differing degrees.

Several studies, including that of Diring et al., test the effect of multiple additives, such as acetic acid in the place of lauric acid, which is an indirect probe of the effect of differing additive pK_a values. However, even this change by itself is not enough to deconvolute the intertwined equilibria: metals may also coordinate to acetate.[114] Further, since the pK_a of acetate is different from that of lauric acid, two methods of comparison may be considered. In the first, the same equivalencies of each molecule are added; in this case, the resultant solution pH (or pH*, in non-aqueous media) is different between the two solutions. In the second, different equivalencies are added to force the solution pH to be identical; in this case, different concentrations should bring about different speciation and coordination in solution.

Recognizing these issues, in some cases an attempt was made to counterbalance the lowering of solution pH by adding compensating Brønsted-Lowry acids or bases in addition to the modulators.[115–117] However, this strategy alters another solution variable yet to be discussed, which is the ionic strength of solution, a measure of the total number of ions present. At higher ionic strength, the results are not strictly comparable, as the dramatic increase in ion concentration changes dissociation constants and reactant solubility.[118–120]

Non- and Weakly-Coordinating Bases and Buffers. An outstanding challenge in metal–organic framework synthesis is thus to control pH (and resultant ligand protonation) without participating in metal complexation. One set of appropriate compounds are non-coordinating bases, which are sterically hindered organic bases, often nitrogen heterocycles with steric bulk surrounding the nitrogen atom (some examples of which are displayed in Fig. 1.4).[121] While the nitrogen site may interact with protons, the steric bulk prevents the complexation of larger Lewis acids, allowing for non-coordinating pH control. Another option is that of non-coordinating buffers.

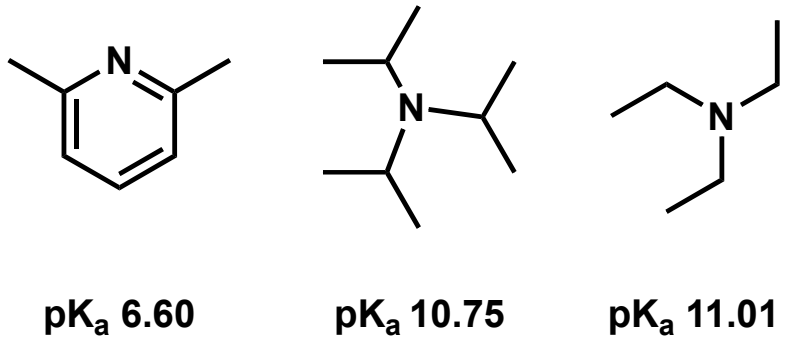

Figure 1.4. Three examples of weakly- or non-coordinating bases, from left: 2,6-Lutidine, N,N-Diisopropylethylamine, triethylamine, with listed pK_a values (room temperature, water).[122]

The challenge of separating the variables of pH and metal ion complexation has long been prevalent for biochemical and biological applications. Studies involving cell metabolism commonly show that pH influences protein structure, metabolic activity and enzymatic rates. Metal ions play fundamental roles in biology by serving as cofactors for a number of different cellular processes involved in homeostasis, but elevated levels can be toxic.[123,124] Thus, studying cellular mechanisms requires pH control without adding molecules which will interfere in metal complexation processes.

In 1966, Good et al. introduced a set of twelve pH buffers to be used in biological studies for control of pH near physiological levels.[125] Controlling pH is necessary for the measurement of physiologically relevant properties, but for processes involving metal ion cofactors it is crucial that the buffer molecules do not form complexes with the metals. Given that metal ion cofactors play an important role in regulating the kinetic and thermodynamic pathways of many biological processes,[126–128] unintended buffer-metal complexation poses a risk of interfering with or fundamentally altering the physiological property being measured. As a result, biological or non-coordinating buffers have become a mainstay in cellular biology studies, and a wide pH range may now be covered with non- or weakly-coordinating buffers.[129,130] These buffers now cover the pH range 3–11 continuously. Applications of both non-coordinating bases and non-coordinating buffers are used in Chapters 2 and 3 of this work. As a final note, the title "non-coordinating" is only accurate within certain ranges that are condition- and metal-dependent; several studies have found appreciable metal-buffer interactions.[131] As a result, it is good to test the effect of including a biological buffer rather than assuming it does not participate in coordination equilibria.

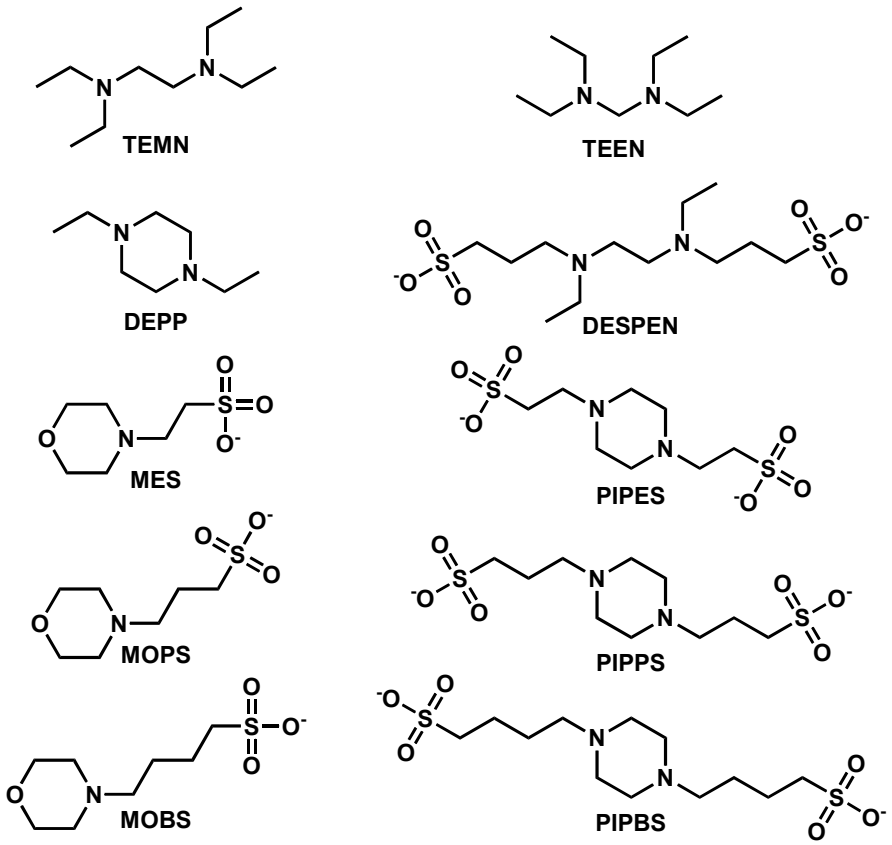

Figure 1.5. Non-complexing tertiary amine buffer compounds. Adapted from Ref. 125. MES and MOPS buffers are used in this work.

1.4 Mass Transport in Porous Materials

Nanoporous materials are prized for their high internal surface area, which can be used to interact with guest molecules. Of equal importance in actual application to the equilibrium adsorption behavior is the process sorption kinetics, the rate at which the materials approach

equilibrium. Achieving very high internal surface areas, required for high capacity or catalytic activity, requires pore sizes at or near the nanometer size regime.[132] Transport through the pores occurs mainly by diffusion, a random-walk process tending towards maximum system entropy. Understanding the process, time scales, and mechanism of diffusion is crucial to the goal of modeling and optimizing nanoporous systems for process development.

Although diffusional processes can control the overall process kinetics, this is not always the case: that is, diffusional behavior is not necessarily identical to the macroscopic adsorption or desorption kinetics. Most adsorbents contain multiple potential resistances to mass transfer: diffusion within the micropores, diffusion between particles or in the macropores, and in some cases a barrier to mass transfer via film resistance. Often, nanoporous materials are formulated as pellets, using a binding agent to improve mechanical properties.[133,134] These materials may generally be modeled as coupled diffusional resistances.[135–137] An example schematic is shown in Figure 1.6. For an adsorbate to interact with the designed sorption sites within the adsorbent crystallite, adsorbates must traverse though the external film, if it exists, through macropores, and then through the micropores of the material. Generally, the process of adsorption at the sites is an extremely rapid process,[138] so the overall rate is generally a function of the mass transport resistances in series. The relative magnitude of these resistances is highly material- and process-dependent.

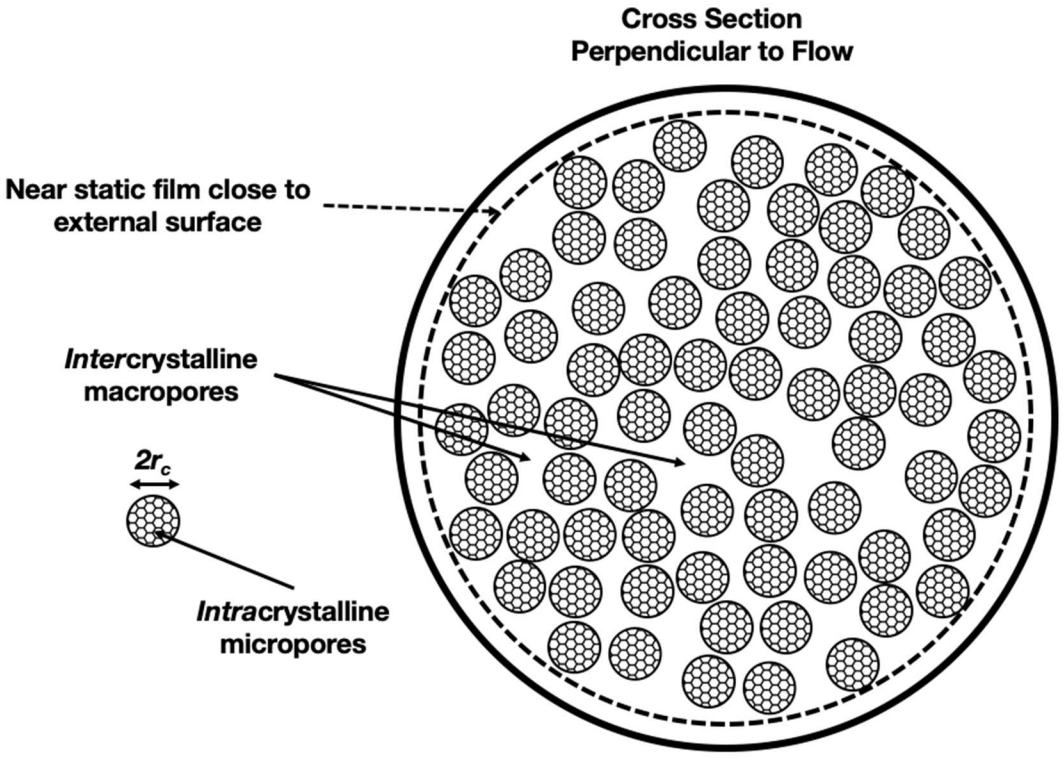

Figure 1.6. In this cartoon of an adsorbent pellet, several mass transfer resistances can occur in series or in parallel. Controlling crystallite path length (via morphology control) has the strongest effect on traversal through the intracrystalline micropores, which may or may not dictate the apparent kinetics observed for a given experiment.

Further, adsorption is generally an exothermic process (examples of endothermic chemisorption exist but are beyond the scope of this chapter).[139] As a result, isothermal operation requires that the rate of heat dissipation via conduction, convection, and/or radiation be high relative to the rate of adsorption, or thermal gradients will develop. For this reason, heat transfer can limit the kinetics of adsorption and indeed is often a very important parameter in adsorption beds. Because metal–organic frameworks are highly porous, their thermal conductivity can be rather low.[140,141] The apparent kinetics of sorption can thus be controlled by a number of mass or heat transfer resistances. Measuring the inherent micropore diffusivity is not as simple as merely measuring the transport sorption kinetics. Instead, a technique that can discern between these different mechanisms of control is required.

Microscopic and Macroscopic Measurements of Diffusion. A wide variety of different techniques have been developed to study diffusional and transport behavior in nanoporous materials across different time and length scales. A few of these techniques will be discussed here. Theoretical and computational methods of studying diffusion in nanoporous materials, which are certainly important techniques allowing for molecular understanding of transport mechanisms, are beyond the scope of this chapter.[142–145]

Macroscopic measurements generally impose a step change in pressure or partial pressure to an adsorbent sample and follow the rates of adsorption, such that the initial and boundary conditions are well-controlled.[146] When the intracrystalline diffusivity is much slower than other mass transfer resistances, the diffusivity may be extracted from the apparent sorption kinetics. As discussed, however, this is frequently an insufficient level of granularity given the intrusion of extra-crystalline mass transfer resistances and heat transfer resistances. Under controlled conditions, macroscopic measurements may discern between different resistances and avoid the encroachment of heat effects. These conditions will be discussed in Section 1.5.

Microscopic methods have also been developed to study diffusivity and indeed can give more detailed information on transport mechanisms. Generally, these either measure transient concentration profiles or follow the mean square displacement of adsorbates over some known time interval. For the former, two common techniques include interference microscopy and infrared microscopy. These techniques directly observe concentration gradients in large crystals (characteristic crystallite dimension ten microns for interference microscopy to tens of microns for infrared microscopy), usually one crystal at a time. For macroscopic methods, information about controlling resistances is inferred using different control tests. Microscopic methods can instead allow direct visualization of guest molecule concentration profiles.

The final technique discussed here is pulsed field gradient nuclear magnetic resonance spectroscopy (PFG-NMR). The interested reader is directed to more detailed reviews of this technique and its use in diffusional studies. In brief, NMR relies upon the fact that nuclei possess a magnetic moment. Under the influence of a magnetic field, nuclei precess with angular frequency around the direction of the magnetic field. The net effect of many nuclei doing so gives rise to rotating magnetization, which induces a voltage in a surrounding coil. Pulsed field gradient NMR utilizes the superposition of magnetic fields at specific time intervals to allow spatial resolution of nuclear spins in a given direction. Variation of time intervals involved can allow study of mean molecular displacements across a wide range of length scales.

Studies of adsorbate transport within metal–organic frameworks have been reported using each of these method categories. In particular, gravimetric studies[147–152] and PFG-NMR studies[153–155] are numerous. One advantage of gravimetric techniques is that there are few limitations on the materials that may be studied. However, many different mass transfer resistances (or combinations

thereof) can lead to identical-looking curves, leading to difficulty in assigning which resistance is controlling. It is similarly difficult to rule out the encroachment of heat effects.

In a study of intracrystalline self-diffusivity, PFG-NMR requires that the root-mean-square displacement of adsorbate molecules be much smaller than the size of the adsorbent crystals and that the adsorbate displacements be large enough to attenuate the NMR signal.[156] This requires both sufficiently large crystallite size and sufficient control over observation time. The former condition is a (sometimes unachievable) requirement for synthetic chemists; the latter condition is a combination of instrument- and system-specific effects. Further, while it is certainly possible to use PFG-NMR with metal–organic frameworks that feature paramagnetic metals, the presence of these metal ions causes wide chemical shifts and broadened signal.[157] Many of the transition metals included in frameworks are correspondingly more difficult to study using this technique.

Zero-Length Column Chromatography. The ZLC technique was developed to overcome some of the disadvantages of macroscopic techniques, in particular to eliminate heating effects from transient kinetics experiments and to develop rigorous control tests that can differentiate between different mass transfer resistances.[158] The desorption curve of a small amount (microgram- to milligram-scale) of adsorbent previously equilibrated with a gas stream is measured. By varying the experimental conditions, such as flow rate of purge gas, crystallite size, and identity of purge gas, the system can be run under equilibrium control or kinetic control. Heat transfer effects are minimized by running the experiments under high flow rates, which prevents large thermal gradients. High flow rates during desorption also work to maintain the adsorbate concentration at the crystallite surface to a low level, approximated as zero. The technique is thus called "zero-length" because it approximates the limit as the adsorbent bed goes to zero size, managing to eliminate the encroachment of thermal and mass transfer bed effects. Because of its small size, the cell is normally approximated as a well-mixed cell and axial dispersion is eliminated.

The concept of equilibrium control versus kinetic control and how tests can differentiate between them will follow a derivation of zero-length column response under ideal circumstances. A discussion of non-idealities will follow. Consider a mass balance across the ZLC cell during a desorption experiment, assuming negligible fluid-phase hold-up (generally applicable for gas and vapor phase):[159]

$$V_s \frac{\mathrm{d}\bar{q}}{\mathrm{d}t} + Fc = 0 \tag{1.4.1}$$

where V_s is the volume of the solid, $\bar{q}$ is the average concentration inside the crystallites, F is the volumetric flow rate, and c is the concentration in the fluid phase. Recall that since the cell is infinitesimally small, the fluid phase has concentration c everywhere within the cell. Assuming spherical crystallites, the diffusion equation is:

$$\frac{\partial q}{\partial r} = \mathrm{D}\left(\frac{\partial^2 q}{\partial r^2} + \frac{2}{r} \cdot \frac{\partial q}{\partial r}\right) \tag{1.4.2}$$

with initial and boundary conditions, assuming a linear equilibrium relationship:

$$q(r,0) = q_0 K c_0;\ c(0) = c_0$$

$$\left(\frac{\partial q}{\partial r}\right)_{r=0} = 0 \tag{1.4.3}$$

The solution to these sets of equations is provided by Crank[160] concerning the problem of diffusion in a sphere with surface evaporation:

$$\frac{M_t}{M_\infty} = 1 - \sum_{n=1}^{\infty} \frac{6L^2 exp(-\beta_n^2 Dt/R^2)}{\beta_n^2[\beta_n^2 + L(L-1)]} \tag{1.4.4}$$

where

$$L = \alpha \mathrm{R/D}$$

and

$$\alpha = \frac{\varepsilon v R}{3(1-\varepsilon)Kz}$$

The more common expression for *L* is:

$$L = \left(\frac{1}{3}\right)\left(\frac{F}{KV_s}\right) / \left(\frac{D}{\mathrm{R}^2}\right) \tag{1.4.5}$$

Thus, L is a ratio between an inverse equilibrium time constant (s^{-1}) and an inverse diffusional time constant (s^{-1}). When L is much greater than 1, the inverse diffusional time constant is significantly lower than the inverse equilibrium adsorption time constant, and the process is kinetically controlled. When L is less than 1, the inverse equilibrium time constant is less than the inverse diffusional time constant, and the process is equilibrium-controlled, which is to say that the adsorbent is equilibrated with the stream at all times. Under these conditions, the kinetics of desorption are merely a function of the volume of purge gas that has gone through the cell, and the time constant is one corresponding to purge gas flow rate. Under kinetic control, the desorption curve instead is controlled by diffusional behavior.

β_n is given by the roots of the equation:

$$\beta_n \cot \beta_n + L - 1 = 0$$

Equation 1.4.4 may be expressed in terms of the effluent concentration:

$$\frac{c}{c_0} = 2L \sum_{n=1}^{\infty} \frac{exp(-\beta_n^2 Dt/R^2)}{[\beta_n^2 + L(L-1)]} \tag{1.4.6}$$

At long times, only the first term of the series is significant, and may be analyzed according to the long-time asymptote:

$$\ln(c/c_0) \sim ln\left[\frac{2L}{\beta_n^2 + L(L-1)}\right] - \beta_n^2 Dt/R^2 \tag{1.4.7}$$

Under terms of kinetic control, by fitting a line to the long-term asymptote or using a full curve, values for the diffusional time constant D/R^2 may be obtained.

Effect of Non-Linear Isotherm. Some pertinent deviations from the assumptions leading to the derivation above are now discussed. Ideally, the experiment would be run in the infinitely dilute region of the isotherm: that is, where the equilibrium relationship between partial pressure and amount adsorbed is linear. In practical terms, this region may not always be accessible, particularly for strongly binding adsorbates. In this case, a different boundary condition must be applied, such as a Langmuir adsorption isotherm, which includes material saturation.[161] The new boundary condition describing equilibrium at the surface for a Langmuir isotherm is:

$$\frac{q(R,t)}{q_s} = \frac{bc}{1+bc} \tag{1.4.8}$$

where q_s is the concentration in the solid at saturation and b is the material and adsorbate-specific Langmuir parameter (m^3/mol). Further, the diffusivity is now concentration-dependent, which must be accounted for in the model. The interested reader is directed to Brandani's work on the theory[161] and experiments[162] of non-linear ZLC.

For the purposes of this text, the following conclusions are relevant. First, the qualitative shape of the curve for linear and non-linear ZLC is the same. Second, the long-time asymptotic slope under kinetic control is the same for linear and non-linear ZLC. During desorption, the concentration in the solid drops until it is at some point low enough to fall into the linear regime of the isotherm. However, the time it takes to approach this point will increase, and the initial drop in concentration at early times will also increase.

Non-Spherical Crystal Morphology. An additional deviation from the assumptions can come from crystal morphology. The above analysis is for isotropic materials with spherical shape. In the case of metal–organic frameworks considered in this work, M_2(dobdc) and M_2(dobpdc), the materials are highly anisotropic, featuring one-dimensional pores and often having long rod morphologies. The diffusion equation instead should be that of one-dimensional diffusion through a parallel-sided slab,[160] and the relevant critical dimension is then not the radius R of a sphere but the path length half-thickness *l*. Correspondingly, the expression for the desorption curve, under kinetic control, is:[163]

$$\frac{c}{c_0} = 2L \sum_{n=1}^{\infty} \frac{exp(-\beta_n^2 Dt/l^2)}{[\beta_n^2 + L(L+1)]} \tag{1.4.9}$$

where $-\beta_n$ is given by the roots of the equation:

$$\beta_n \, tan(\beta_n) \; = \; L \; = \left(\frac{F}{KV_s}\right)\left(\frac{l^2}{D}\right)$$

leading to a long-time asymptote where only the first root β_1 is significant:

$$ln(c/c_0) = ln\left[\frac{2L}{\beta_1^2 + L(L+1)}\right] - \beta_1^2 Dt/l^2 \quad (1.4.10)$$

Alternatively, analysis of crystals of different morphologies can use an equivalent spherical radius, or the radius of a sphere that would give the same behavior as the true sample.[164] This description deviates the most for slab-like diffusion, and the greatest region of error is in the long-time asymptote, which contains the most information about diffusion.[165]

Crystal Size Distribution. While the original derivation contains just one value for R, crystal radius, all syntheses lead to a finite distribution of sizes and resultant distribution of characteristic lengths. Given that the parameter D/R^2 (or D/l^2) is a diffusional time constant, the inclusion of multiple R or *l* values leads to multiple time constants present. While the derivation is not presented here, it can be shown that including such distributions introduces curvature into the linear asymptote region.[166] Analyzing the curves without taking the size distribution into account leads to overestimation of diffusivities and underestimation of the non-dimensional parameter *L*. Unsurprisingly, increasing distribution width leads to increasing error in these parameters.

Several solutions have been presented by Duncan et al. in a review of the effects of including crystal size distributions.[166] First, the crystal radius may be treated as a volume-weighted average radius and substituted directly into Equation 1.4.6 or Equation 1.4.9. A more accurate method, originally suggested by Loos et al., is the use of a superposition of surface area-normalized responses for discrete size fractions, where each fraction is represented by its largest dimension.[165] Second, when the crystal size distribution follows a continuous analytical size distribution, it is possible to solve the diffusion equations analytically. Care must be taken with this approach: with sub-milligram quantities of sample, it can be difficult to obtain a truly representative measurement of crystal size and distribution. As Duncan et al. point out, it is possible to introduce significant error through the attempt to describe a real, non-ideal distribution with an analytical model.

1.5 References

(1) Li, J.-R.; Kuppler, R. J.; Zhou, H.-C. *Chem. Soc. Rev.* **2009**, *38* (5), 1477.
(2) Zhou, H.-C.; Long, J. R.; Yaghi, O. M. *Chem. Rev.* **2012**, *112* (2), 673.
(3) Barnett, B. R.; Gonzalez, M. I.; Long, J. R. *Trends in Chemistry*. **2019**, *1*, 159.
(4) McDonald, T. M.; Mason, J. A.; Kong, X.; Bloch, E. D.; Gygi, D.; Dani, A.; Crocella, V.; Giordanino, F.; Odoh, S. O.;Drisdell, W.; Vlaisavljevich, B.; Dzubak, A. L.; Poloni, R.; Schnell, S. K.; Planas, N.; Lee, K.; Pascal, T.; Wan, L. F.; Prendergast, D.; Neaton, J. B.; Smit, B.; Kortright, J. B.; Gagliardi, L.; Bordiga, S.; Reimer, J. A.; Long, J. R. *Nature* **2015**, *519* (7543), 303.
(5) Wang, L.; Han, Y.; Feng, X.; Zhou, J.; Qi, P.; Wang, B. *Coord. Chem. Rev.* **2016**, *307*, 361.
(6) Suh, M. P.; Park, H. J.; Prasad, T. K.; Lim, D.-W. *Chem. Rev.* **2012**, *112* (2), 782.
(7) Ma, S.; Zhou, H.-C. *Chem. Commun.* **2010**, *46* (1), 44.
(8) Mason, J. A.; Oktawiec, J.; Taylor, M. K.; Hudson, M. R.; Rodriguez, J.; Bachman, J. E.; Gonzalez, M. I.; Cervellino, A.; Guagliardi, A.; Brown, C. M.; Llewellyn, P. L.; Masciocchi, N.; Long, J. R. *Nature* **2015**, *527* (7578), 357.
(9) Rosi, N. L.; Eckert, J.; Eddaoudi, M.; Vodak, D. T.; Kim, J.; O'Keeffe, M.; Yaghi, O. M. *Science* **2003**, *300* (5622), 1127.
(10) Xiao, D. J.; Bloch, E. D.; Mason, J. A.; Queen, W. L.; Hudson, M. R.; Planas, N.; Borycz,

J.; Dzubak, A. L.; Verma, P.; Lee, K.; Bonino, F.; Crocella, V.; Yano, J.; Bordiga, S.; Truhlar, D. G.; Gagliardi, L.; Brown, C. M.; Long, J. R. *Nat. Chem.* **2014**, *6* (7), 590.
(11) Yang, D.; Gates, B. C. *ACS Catal.* **2019**, *9* (3), 1779.
(12) Corma, A.; García, H.; Llabrés i Xamena, F. X. *Chem. Rev.* **2010**, *110* (8), 4606.
(13) Lee, J.; Farha, O. K.; Roberts, J.; Scheidt, K. A.; Nguyen, S. T.; Hupp, J. T. *Chem. Soc. Rev.* **2009**, *38* (5), 1450.
(14) Levine, D. J.; Gonzalez, M. I.; Legendre, C. M.; Runčevski, T.; Oktawiec, J.; Colwell, K. A.; Long, J. R. *ChemMedChem* **2017**, *12*, 1739.
(15) Levine, D.J.; Runčevski, T.; Kapelewski, M. K.; Keitz, B. K.; Oktawiec, J.; Reed, D. A.; Mason, J. A.; Jiang, H. Z. H.; Colwell, K. A.; Legendre, C. M.; FitzGerald, S. A.; Long, J. R. *J. Am. Chem. Soc.* **2016**, *138*, 10143.
(16) Horcajada, P.; Serre, C.; Vallet-Regí, M.; Sebban, M.; Taulelle, F.; Férey, G. *Angew. Chemie Int. Ed.* **2006**, *45* (36), 5974.
(17) Horcajada, P.; Chalati, T.; Serre, C.; Gillet, B.; Sebrie, C.; Baati, T.; Eubank, J. F.; Heurtaux, D.; Clayette, P.; Kreuz, C.; Chang, J-S; Hwang, Y.K.; Marsaud, V.; Bories, P-N.; Cynober, L.; Gil, S.; Férey, G.; Couvreur, P.; Gref, R. *Nat. Mater.* **2010**, *9* (2), 172.
(18) Gassensmith, J. J.; Kim, J. Y.; Holcroft, J. M.; Farha, O. K.; Stoddart, J. F.; Hupp, J. T.; Jeong, N. C. *J. Am. Chem. Soc.* **2014**, *136* (23), 8277.
(19) Chen, L.; Ye, J.-W.; Wang, H.-P.; Pan, M.; Yin, S.-Y.; Wei, Z.-W.; Zhang, L.-Y.; Wu, K.; Fan, Y.-N.; Su, C.-Y. *Nat. Commun.* **2017**, *8* (1), 15985.
(20) Campbell, M. G.; Sheberla, D.; Liu, S. F.; Swager, T. M.; Dincă, M. *Angew. Chemie Int. Ed.* **2015**, *54* (14), 4349.
(21) Kreno, L. E.; Leong, K.; Farha, O. K.; Allendorf, M.; Van Duyne, R. P.; Hupp, J. T. *Chem. Rev.* **2012**, *112* (2), 1105.
(22) Lu, G.; Hupp, J. T. *J. Am. Chem. Soc.* **2010**, *132* (23), 7832.
(23) Oak Ridge National Laboratory. *Materials for Separation Technologies: Energy and Emission Reduction Opportunities* (2005).
(24) Bloch, E. D.; Queen, W. L.; Krishna, R.; Zadrozny, J. M.; Brown, C. M.; Long, J. R. *Science* **2012**, *335* (6076), 1606.
(25) Murray, L. J.; Dincă, M.; Long, J. R. *Chem. Soc. Rev.* **2009**, *38* (5), 1294.
(26) Chen, B.; Eddaoudi, M.; Reineke, T. M.; Kampf, J. W.; O'Keeffe, M.; Yaghi, O. M. *J. Am. Chem. Soc*. **2000**, *122*, 11559.
(27) Chui, S. S.-Y.; Lo, S. M.-F.; Charmant, J. P. H.; Orpen, A. G.; Williams, I. D. *Science* **1999**, *283* (5405), 1148.
(28) Siegelman, R. L.; McDonald, T. M.; Gonzalez, M. I.; Martell, J. D.; Milner, P. J.; Mason, J. A.; Berger, A. H.; Bhown, A. S.; Long, J. R. *J. Am. Chem. Soc.* **2017**, *139*, 10526.
(29) Milner, P. J.; Siegelman, R. L.; Forse, A. C.; Gonzalez, M. I.; Runčevski, T.; Martell, J. D.; Reimer, J. A.; Long, J. R. *J. Am. Chem. Soc.* **2017**, *139* (38), 13541.
(30) Milner, P. J.; Martell, J. D.; Siegelman, R. L.; Gygi, D.; Weston, S. C.; Long, J. R. *Chem. Sci.* **2018**, *9* (1), 160.
(31) Rosi, N. L.; Kim, J.; Eddaoudi, M.; Chen, B.; Yaghi, O. M. *J. Am. Chem. Soc.* **2005**, *127*, 1504.
(32) Rowsell, J. L. C.; Yaghi, O. M. *J. Am. Chem. Soc.* **2006**, *128* (4), 1304.
(33) Caskey, S. R.; Wong-Foy, A. G.; Matzger, A. J. *J. Am. Chem. Soc.* **2008**, *130* (33), 10870.
(34) Díaz-García, M.; Sánchez-Sánchez, M. *Microporous Mesoporous Mater.* **2014**, *190*, 248.
(35) Fu, Y.; Sun, D.; Qin, M.; Huang, R.; Li, Z. *RSC Adv.* **2012**, *2* (8), 3309.

(36) Yang, D.-A.; Cho, H.-Y.; Kim, J.; Yang, S.-T.; Ahn, W.-S. *Energy Environ. Sci.* **2012**, *5* (4), 6465.
(37) Gadipelli, S.; Ford, J.; Zhou, W.; Wu, H.; Udovic, T. J.; Yildirim, T. *Chem. – A Eur. J.* **2011**, *17* (22), 6043.
(38) Peng, Y.; Krungleviciute, V.; Eryazici, I.; Hupp, J. T.; Farha, O. K.; Yildirim, T. *J. Am. Chem. Soc.* **2013**, *135* (32), 11887.
(39) Kapelewski, M. T.; Runčevski, T.; Tarver, J. D.; Jiang, H. Z. H.; Hurst, K. E.; Parilla, P. A.; Ayala, A.; Gennett, T.; FitzGerald, S. A.; Brown, C. M.; Long, J. R. *Chem. Mater.* **2018**, *30* (22), 8179.
(40) Sumida, K.; Brown, C. M.; Herm, Z. R.; Chavan, S.; Bordiga, S.; Long, J. R. *Chem. Commun.* **2011**, *47* (4), 1157.
(41) Aubrey, M. L.; Ameloot, R.; Wiers, B. M.; Long, J. R. *Energy Environ. Sci.* **2014**, *7* (2), 667.
(42) Aubrey, M. L.; Long, J. R. *J. Am. Chem. Soc.* **2015**, *137* (42), 13594.
(43) Britt, D.; Furukawa, H.; Wang, B.; Glover, T. G.; Yaghi, O. M. *Proc. Natl. Acad. Sci. U. S. A.* **2009**, *106* (49), 20637.
(44) Bachman, J. E.; Smith, Z. P.; Li, T.; Xu, T.; Long, J. R. *Nat. Mater.* **2016**, *15* (8), 845.
(45) Bachman, J. E.; Kapelewski, M. T.; Reed, D. A.; Gonzalez, M. I.; Long, J. R. *J. Am. Chem. Soc.* **2017**, *139* (43), 15363.
(46) Gonzalez, M. I.; Kapelewski, M. T.; Bloch, E. D.; Milner, P. J.; Reed, D. A.; Hudson, M. R.; Mason, J. A.; Barin, G.; Brown, C. M.; Long, J. R. *J. Am. Chem. Soc*. **2018**, *140*, 3412.
(47) Hu, Q.; Yu, J.; Liu, M.; Liu, A.; Dou, Z.; Yang, Y. *J. Med. Chem.* **2014**, *57* (13), 5679.
(48) Yuan, H.; Tao, J.; Li, N.; Karmakar, A.; Tang, C.; Cai, H.; Pennycook, S. J.; Singh, N.; Zhao, D. *Angew. Chemie Int. Ed.* **2019**. https://doi.org/10.1002/anie.201906222.
(49) Strauss, I.; Mundstock, A.; Treger, M.; Lange, K.; Hwang, S.; Chmelik, C.; Rusch, P.; Bigall, N. C.; Pichler, T.; Shiozawa, H.; Caro, J. *ACS Appl. Mater. Interfaces* **2019**, *11* (15), 14175.
(50) Pentyala, V.; Davydovskaya, P.; Pohle, R.; Urban, G.; Yurchenko, O. *Procedia Engineering* **2014**, *87*, 1071.
(51) Schoen, H. M.; Grove, C. S.; Palermo, J. A. *J. Chem. Educ.* **1956**, *33* (8), 373.
(52) *Industrial Crystallization*; Mullin, J. W., Ed.; Springer US: Boston, MA, 1976.
(53) De Yoreo, J. J.; Vekilov, P. G. *Rev. Mineral. Geochemistry* **2003**, *54* (1), 57.
(54) Gibbs, J. *Trans Connect Acad Sci* **1876**, *3*, 108.
(55) Gibbs, J. *Trans Connect Acad Sci* **1878**, *16*, 343.
(56) Mullin, J. W.; Söhnel, O. *Chem. Eng. Sci.* **1977**, *32*, 683.
(57) Mullin JW. *Crystallization*, 4th ed.; Butterworths: Oxford.
(58) Johnson, D. *Some Thermodynamic Aspects of Inorganic Chemistry*; Cambridge University Press: Cambridge, 1982.
(59) Cox, J. R.; Ferris, L. A.; Thalladi, V. R. *Angew. Chemie Int. Ed.* **2007**, *46* (23), 4333.
(60) Diao, Y.; Myerson, A. S.; Hatton, T. A.; Trout, B. L. *Langmuir* **2011**, *27* (9), 5324.
(61) Chayen, N. E.; Saridakis, E.; Sear, R. P. *Proc. Natl. Acad. Sci. U. S. A.* **2006**, *103* (3), 597.
(62) McPherson, A.; Shlichta, P. *Science* **1988**, *239* (4838), 385.
(63) McPherson, A.; Gavira, J. A. *Acta Cryst*. **2014**, *F70*, 2.
(64) Chatterjee, A. M.; Price, F. P.; Newman, S. *J. Polym. Sci. Polym. Phys. Ed.* **1975**, *13* (12), 2369.
(65) Schonhorn, H. *Macromolecules* **1968**, *1* (2), 145.

(66) Treat, N. D.; Nekuda Malik, J. A.; Reid, O.; Yu, L.; Shuttle, C. G.; Rumbles, G.; Hawker, C. J.; Chabinyc, M. L.; Smith, P.; Stingelin, N. *Nat. Mater.* **2013**, *12* (7), 628.
(67) Lee, S. S.; Muralidharan, S.; Woll, A. R.; Loth, M. A.; Li, Z.; Anthony, J. E.; Haataja, M.; Loo, Y.-L. *Chem. Mater.* **2012**, *24* (15), 2920.
(68) Nancollas, G. H.; Wu, W. *J. Cryst. Growth* **2000**, *211* (1–4), 137.
(69) Jones, S. F.; Evans, G. M.; Galvin, K. P. *Adv. Colloid Interface Sci.* **1999**, *80* (1), 27.
(70) Myerson, A. S. *Handbook of Industrial Crystallization*; Butterworth-Heinemann, 2002.
(71) Bragg, W. H.; Bragg, W. L. *Proc. R. Soc. A Math. Phys. Eng. Sci.* **1913**, *88* (605), 428.
(72) Bragg, W. L. *Atomic Structure of Minerals*; Cornell University Press, 1937.
(73) Garekani, H. A.; Sadeghi, F.; Badiee, A.; Mostafa, S. A.; Rajabi-Siahboomi, A. R.; Rajabi-Siahboomi, A. R. *Drug Dev. Ind. Pharm.* **2001**, *27* (8), 803.
(74) Stoica, C.; Verwer, P.; Meekes, H.; Van Hoof, P. J. C. M.; Kaspersen, F. M.; Vlieg, E. *Cryst. Growth Des.* **2004**, *4* (4), 765.
(75) Li, S.; Li, J.; Dong, M.; Fan, S.; Zhao, T.; Wang, J.; Fan, W. *Chem. Soc. Rev*. **2019**, *48*, 885.
(76) Round, C. I.; Hill, S. J.; Latham, K.; Williams, C. D. *Microporous Mater.* **1997**, *11* (3–4), 213.
(77) Teketel, S.; Lundegaard, L. F.; Skistad, W.; Chavan, S. M.; Olsbye, U.; Lillerud, K. P.; Beato, P.; Svelle, S. *J. Catal.* **2015**, *327*, 22.
(78) Stassen, I.; De Vos, D.; Ameloot, R. *Chem. - A Eur. J.* **2016**, *22* (41), 14452.
(79) Holopainen, J.; Heikkilä, M. J.; Salmi, L. D.; Ainassaari, K.; Ritala, M. *Microporous Mesoporous Mater.* **2018**, *267*, 212.
(80) Reif, B.; Somboonvong, J.; Fabisch, F.; Kaspereit, M.; Hartmann, M.; Schwieger, W. *Microporous Mesoporous Mater.* **2019**, *276*, 29.
(81) Friščić, T.; Reid, D. G.; Halasz, I.; Stein, R. S.; Dinnebier, R. E.; Duer, M. J. *Angew. Chemie Int. Ed.* **2010**, *49* (4), 712.
(82) Friščić, T.; Halasz, I.; Beldon, P. J.; Belenguer, A. M.; Adams, F.; Kimber, S. A. J.; Honkimäki, V.; Dinnebier, R. E. *Nat. Chem.* **2013**, *5* (1), 66.
(83) Klimakow, M.; Klobes, P.; Thünemann, A. F.; Rademann, K.; Emmerling, F. *Chem. Mater.* **2010**, *22* (18), 5216.
(84) López-Cabrelles, J.; Romero, J.; Abellán, G.; Giménez-Marqués, M.; Palomino, M.; Valencia, S.; Rey, F.; Mínguez Espallargas, G. *J. Am. Chem. Soc.* **2019**, *141* (17), 7173.
(85) Chen, B.; Eddaoudi, M.; Hyde, S. T.; O'Keeffe, M.; Yaghi, O. M. *Science* **2001**, *291* (5506), 1021.
(86) Eddaoudi, M.; Kim, J.; Rosi, N.; Vodak, D.; Wachter, J.; O'Keeffe, M.; Yaghi, O. M. *Science* **2002**, *295*, 469.
(87) Stock, N.; Biswas, S. *Chem. Rev.* **2012**, *112* (2), 933.
(88) Yaghi, O. M.; Li, H. *J. Am. Chem. Soc.* **1995**, *117* (41), 10401.
(89) Lu, J. Y. *Coord. Chem. Rev.* **2003**, *246* (1–2), 327.
(90) Schlichte, K.; Kratzke, T.; Kaskel, S. *Microporous Mesoporous Mater.* **2004**, *73* (1–2), 81.
(91) Al-Kutubi, H.; Gascon, J.; Sudhölter, E. J. R.; Rassaei, L. *ChemElectroChem* **2015**, *2* (4), 462.
(92) Campagnol, N.; Van Assche, T. R. C.; Li, M.; Stappers, L.; Dincă, M.; Denayer, J. F. M.; Binnemans, K.; De Vos, D. E.; Fransaer, J. *J. Mater. Chem. A* **2016**, *4* (10), 3914.
(93) Yang, D.-A.; Cho, H.-Y.; Kim, J.; Yang, S.-T.; Ahn, W.-S. *Energy Environ. Sci.* **2012**, *5*

(4), 6465.
(94) Israr, F.; Chun, D.; Kim, Y.; Kim, D. K. *Ultrason. Sonochem.* **2016**, *31*, 93.
(95) Diring, S.; Furukawa, S.; Takashima, Y.; Tsuruoka, T.; Kitagawa, S. *Chem. Mater.* **2010**, *22* (16), 4531.
(96) McDonald, T. M.; Lee, W. R.; Mason, J. A.; Wiers, B. M.; Hong, C. S.; Long, J. R. *J. Am. Chem. Soc.* **2012**, *134* (16), 7056.
(97) Klinowski, J.; Almeida Paz, F. A.; Silva, P.; Rocha, J. *Dalton Trans*. **2011**, *2*, 321.
(98) Ni, Z.; Masel, R. I. *J. Am. Chem. Soc.* **2006**, *128* (38), 12394.
(99) Sánchez-Sánchez, M.; Getachew, N.; Díaz, K.; Díaz-García, M.; Chebude, Y.; Díaz, I. *Green Chem.* **2015**, *17*, 1500.
(100) Bae, T.-H.; Long, J. R. *Energy Environ. Sci.*, **2013**, *6*, 3565.
(101) Bachman, J. E.; Smith, Z. P.; Li, T.; Xu, T.; Long, J. R. *Nat. Mater.* **2016**, *15*, 845.
(102) Gonzalez, M. I.; Oktawiec, J.; Long, J. R. *Faraday Discuss.* **2017**, *201*, 351.
(103) Majewski, M. B.; Noh, H.; Islamoglu, T.; Farha, O. K. *J. Mater. Chem. A,* **2018**, *6*, 7338.
(104) Rondinini, S. *Anal. Bioanal. Chem.* **2002**, *374* (5), 813.
(105) Moosavi, S. M.; Chidambaram, A.; Talirz, L.; Haranczyk, M.; Stylianou, K. C.; Smit, B. *Nat. Commun.* **2019**, *10* (1), 539.
(106) Libuś, W.; Puchalska, D.; Walczak, M. *Nature*. **1967**, *214*, 480.
(107) Libuś, W. On the Formation of Tetrahedral Cobalt(II) Complexes in Solution. In *Theory and Structure of Complex Compounds*; 1964; pp 537–550.
(108) Ohtaki, H. *Pure Appl. Chem.* **1987**, *59* (9), 1143.
(109) Umemura, A.; Diring, S.; Furukawa, S.; Uehara, H.; Tsuruoka, T.; Kitagawa, S. *J. Am. Chem. Soc.* **2011**, *133* (39), 15506.
(110) Hermes, S.; Witte, T.; Hikov, T.; Zacher, D.; Bahnmüller, S.; Langstein, G.; Huber, K.; Fischer, R. A. *J. Am. Chem. Soc.* **2007**, *129* (17), 5324.
(111) Cho, W.; Lee, H. J.; Oh, M. *J. Am. Chem. Soc.* **2008**, *130* (50), 16943.
(112) Pachfule, P.; Shinde, D.; Majumder, M.; Xu, Q. *Nat. Chem.* **2016**, *8* (7), 718.
(113) Schumann, K.; Siekmann, K. *Soaps in Ullman's Encyclopedia of Industrial Chemistry*; 2000.
(114) Edwards, D. A.; Hayward, R. N. *Transition Metal Acetates*; 1968; Vol. 46.
(115) Guo, H.; Zhu, Y.; Wang, S.; Su, S.; Zhou, L.; Zhang, H. *Chem. Mater.* **2012**, *24* (3), 444.
(116) Shan, B.; James, J. B.; Armstrong, M. R.; Close, E. C.; Letham, P. A.; Nikkhah, K.; Lin, Y. S.; Mu, B. *J. Phys. Chem. C* **2018**, *122* (4), 2200.
(117) Zhao, Y.; Zhang, Q.; Li, Y.; Zhang, R.; Lu, G. *ACS Appl. Mater. Interfaces* **2017**, *9* (17), 15079.
(118) Barthel, J. M. G.; Krienke, H.; Kunz, W. *Physical Chemistry of Electrolyte Solutions: Modern Aspects*; Steinkopff, Darmstadt, and Springer: New York, 1998.
(119) *Activity Coefficients in Electrolyte Solutions*, 2nd ed.; Pitzer, K. S., Ed.; CRC Press: Boca Raton, FL, 2018.
(120) Kielland, J. *J. Am. Chem. Soc.* **1937**, *59* (9), 1675.
(121) Anslyn, E.V.; Dougherty, D. A. Modern Physical Organic Chemistry. University Science Books: Sausalito, California, 2006.
(122) *Ullmann's Encyclopedia of Industrial Chemistry*; Wiley, 2000.
(123) Frausto da Silva, J. J. R.; Williams, R. J. P. *The Biological Chemistry of the Elements*; Oxford University Press: Oxford, UK, 1991.
(124) Lippard, S. J.; Berg, J. M. *Principles of Bioinorganic Chemistry*; University Science

Books: Mill Valley, CA, 1994.
(125) Good, N. E.; Winget, G. D.; Winter, W.; Connolly, T. N.; Izawa, S.; Singh, R. M. M. *Biochemistry* **1966**, *5* (2), 467.
(126) Holm, R. H.; Kennepohl, P.; Solomon, E. I. *Chem. Rev.* **1996**, *96* (7), 2239.
(127) Åqvist, J.; Warshel, A. *J. Am. Chem. Soc.* **1990**, *112* (8), 2860.
(128) Åqvist, J.; Warshel, A. *J. Mol. Biol.* **1992**, *224* (1), 7.
(129) Yu, Q.; Kandegedara, A.; Xu, Y.; Rorabacher, D. B. *Anal. Biochem.* **1997**, *253* (1), 50.
(130) Kandegedara, A.; Rorabacher, D. B. *Anal. Chem.* **1999**, *71* (15), 3140.
(131) Ferreira, C. M. H.; Pinto, I. S. S.; Soares, E. V.; Soares, H. M. V. M. *RSC Adv.* **2015**, *5* (39), 30989.
(132) *Practical Gas Chromatography*; Dettmer-Wilde, K., Engewald, W., Eds.; Springer Berlin Heidelberg: Berlin, Heidelberg, 2014.
(133) Kärger, J.; Ruthven, D. M. *New J. Chem.* **2016**, *40* (5), 4027.
(134) Rezaei, F.; Webley, P. *Chem. Eng. Sci.* **2009**, *64* (24), 5182.
(135) Ruckenstein, E.; Vaidyanathan, A. S.; Youngquist, G. R. *Chem. Eng. Sci.* **1971**, *26* (9), 1305.
(136) Lee, L. K. *AIChE J.* **1978**, *24* (3), 531.
(137) Ma, Y. H.; Lee, T. Y. *AIChE J.* **1976**, *22* (1), 147.
(138) Kärger, J.; Ruthven, D. M.; Theodorou, D. N. *Diffusion in Nanoporous Materials*; Wiley-VCH: Weinheim, Germany, 2012.
(139) Thomas, J. M. *J. Chem. Educ.* **1961**, *38* (3), 138.
(140) Huang, J.; Xia, X.; Hu, X.; Li, S.; Liu, K. *Int. J. Heat Mass Transf.* **2019**, *138*, 11.
(141) Babaei, H.; McGaughey, A. J. H.; Wilmer, C. E. *Chem. Sci.* **2017**, *8* (1), 583.
(142) Skoulidas, A. I.; Sholl, D. S. *J. Phys. Chem. B* **2005**, *109* (33), 15760.
(143) Amirjalayer, S.; Tafipolsky, M.; Schmid, R. *Angew. Chemie Int. Ed.* **2007**, *46* (3), 463.
(144) Canepa, P.; Nijem, N.; Chabal, Y. J.; Thonhauser, T. *Phys. Rev. Lett.* **2013**, *110* (2), 026102.
(145) Smit, B.; Maesen, T. L. M. *Chem. Rev.* **2008**, *108* (10), 4125.
(146) Kärger, J.; Ruthven, D. M.; Theodorou, D. N. *Diffusion in Nanoporous Materials*. Weinheim, Germany, 2012.
(147) Shi, J.; Zhao, Z.; Xia, Q.; Li, Y.; Li, Z. *J. Chem. Eng. Data* **2011**, *56* (8), 3419.
(148) Xian, S.; Li, X.; Xu, F.; Xia, Q.; Li, Z. *Sep. Sci. Technol.* **2013**, *48* (10), 1479.
(149) Zhao, Z.; Li, X.; Huang, S.; Xia, Q.; Li, Z. *Ind. Eng. Chem. Res.* **2011**, *50* (4), 2254.
(150) Zhao, Z.; Li, X.; Li, Z. *Chem. Eng. J.* **2011**, *173* (1), 150.
(151) Lee, C. Y.; Bae, Y.-S.; Jeong, N. C.; Farha, O. K.; Sarjeant, A. A.; Stern, C. L.; Nickias, P.; Snurr, R. Q.; Hupp, J. T.; Nguyen, S. T. *J. Am. Chem. Soc.* **2011**, *133* (14), 5228.
(152) Zhao, Z.; Li, Z.; Lin, Y. S. *Ind. Eng. Chem. Res.* **2009**, *48* (22), 10015.
(153) Forse, A. C.; Gonzalez, M. I.; Siegelman, R. L.; Witherspoon, V. J.; Jawahery, S.; Mercado, R.; Milner, P. J.; Martell, J. D.; Smit, B.; Blümich, B.; Long, J. R.; Reimer, J. A. *J. Am. Chem. Soc* **2018**, *140*, 1663.
(154) Hertel, S.; Wehring, M.; Amirjalayer, S.; Gratz, M.; Lincke, J.; Krautscheid, H.; Schmid, R.; Stallmach, F. *Eur. Phys. J. Appl. Phys.* **2011**, *55* (2), 20702.
(155) Wehring, M.; Gascon, J.; Dubbeldam, D.; Kapteijn, F.; Snurr, R. Q.; Stallmach, F. *J. Phys. Chem. C* **2010**, *114* (23), 10527.
(156) Kärger, J.; Freude, D.; Haase, J. *Processes* **2018**, *6* (9), 147.
(157) Drago, R. S. *Physical Methods for Chemists*; Saunders College Pub, 1977.

(158) Eic, M.; Ruthven, D. M. *Zeolites* **1988**, *8* (1), 40.
(159) Brandani, S.; Ruthven, D. M. *Adsorption* **1995**, *50* (13), 2055.
(160) Crank, J. The Mathematics of Diffusion, Second Edition. *Oxford Univ. Press* **1975**.
(161) Brandani, S. *Chem. Eng. Sci.* **1998**, *53*, 2791.
(162) Brandani, S.; Jama, M. A.; Ruthven, D. M. *Chem. Eng. Sci.* **2000**, *55* (7), 1205.
(163) Ruthven, D. M.; Eic, M.; Richard, E. *Zeolites* **1991**, *11* (7), 647.
(164) Jennings, B. R.; Parslow, K. *Proc. R. Soc. A Math. Phys. Eng. Sci.* **1988**, *419* (1856), 137.
(165) Loos, J.-B. B. W. P.; Verheijen, P. J. T.; Moulijn, J. A. *Chem. Eng. Sci.* **2000**, *55* (1), 51.
(166) Duncan, W. . L.; Möller, K. P. *Chem. Eng. Sci.* **2002**, *57* (14), 2641.

Chapter 2: Deconvoluting Solution Variables During Metal–Organic Framework Crystallization

2.1 Introduction

Metal–organic frameworks are a promising class of hybrid organic–inorganic porous coordination solids with numerous prospective industrial applications, including gas and liquid separations,[1–4] catalysis,[5,6] drug delivery,[7,8] and energy storage.[9–13] Different combinations of metal cations and clusters with ligands can yield controllable pore sizes, shapes, and functionalities within a unit cell, which have been utilized to design chemical interactions ideally suited for a given application[14]. Successful implementation of this class of materials on an industrial scale, however, demands additional control over macroscale characteristics such as crystallite size and shape. Pelletization processes,[15,16] incorporation into mixed-matrix membranes,[17,18] and use in packed beds[19] are highly dependent on both crystal size and shape distribution. For an individual crystallite, morphology defines surface-area-to-volume ratios and intracrystalline mass transfer resistances.[20] As crystallite size and shape are consequences of the crystallization process, precise understanding and control over the variables involved are required to optimize metal–organic frameworks for future applications.

Controlling solution-based syntheses requires balancing many intertwined equilibria and variables. The ligands, which link metal ions or metal clusters, act during synthesis not only as Lewis bases but also as Brønsted acids, and they thus participate simultaneously in pH and coordination equilibria. The most common previous strategy to control crystallite size and morphology is generally referred to as coordination modulation, first described by Kitagawa et al., wherein molecules are added to the synthetic mixture intended to interfere with the crystallization process without being incorporated in the structure.[21] Since then, the morphologies of many different framework types and topologies have been successfully altered by adding modulators.[22–25] These modulators often feature one or more of the same chemical functionalities as are present on the organic linker.[26] These molecules are intended to be able to bind in similar ways, competing with the linker during growth and thus imposing kinetic limitations on the growth rate in different crystallographic directions. However, the addition of these molecules can lead to unpredictable results, as they, too, participate in multiple equilibria.

To probe new strategies of understanding and controlling variables during synthesis, I used the model framework family M_2(dobdc) (M = Mg, Mn, Fe, Co, Ni, Cu, Zn, Cd; dobdc^{4-} = 2,5-dioxido-1,4-benzenedicarboxylate), a material of significant fundamental and practical interest because of its unparalleled high density of coordinatively-unsaturated metal sites.[27–29] Solvothermal M_2(dobdc) syntheses are generally the combination of a metal(II) salt, often the nitrate or the chloride, with the ligand in some solvent mixture that contains an amide, most commonly N,N-dimethylformamide.[28] Seeking deliberately to separate the equilibria pertaining to metal coordination from that of solution protonation, I created a "greener" synthetic platform where the use of non-coordinating bases and buffers may be used to control pH independently from coordination. Here I show that this may be used to control size and shape of M_2(dobdc) crystallites, as well as uncover mechanisms of competitive coordination in solution for the case study of the cobalt analogue.

2.2 Experimental and Computational Methods

General Procedures, Materials, and Reagents. Laboratory powder X-ray diffraction patterns were collected using a Bruker AXS D8 Advance diffractometer with Cu Kα radiation (λ = 1.5418 Å). All synthetic manipulations were carried out under air, unless otherwise noted. All water used came from a Milli-Q water purification system. With the exception of synthesized cobalt(II) salts, all other reagents and solvents were obtained from commercial suppliers at reagent grade purity or higher and were used without further purification. The ligand H_4dobdc was purchased from Sigma-Aldrich. Elemental analyses for C, H and N were performed at the Microanalytical Laboratory of the University of California, Berkeley. SEM images were taken using a JEOL JSM - 6340F SEM. All samples were prepared by drop-casting particles dispersed in methanol onto a silicon chip, then sputter coating a layer of gold approximately 3 nm thick to reduce sample charging. Crystals were imaged at 5 keV/12 μA.

Synthesis of Cobalt(II) Salts. Synthesis of cobalt(II) chloroacetate, $Co(CClH_2COO)_2$: 19.845 g (0.210 mol) of chloroacetic acid was added dropwise to a stirred suspension of 11.895 g (0.100 mol) cobalt carbonate powder in 50 mL of water in a 250 mL round bottomed flask in a 0 °C ice bath. The flask was stoppered with a rubber septum with a needle to vent and left stirring at 0 °C for 3 hours. The resulting dark pink solution was filtered to remove unreacted metal carbonate and insoluble impurities. The filtrate was rotovapped to a dry resin then dissolved in 50 mL of anhydrous methanol and rotovapped again. This process was repeated twice more with methanol and then the resulting resin was triturated with 50 mL of chloroform, decanted, and dried under dynamic vacuum over 16 hours to yield 23.8 g (0.097 mol 97 % yield) $Co(CClH_2COO)_2$ as a purple solid (Anal. Calcd for $Co(CClH_2COO)_2$: C, 19.54; H, 1.64. Found: C, 19.16; H, 1.74.).

Synthesis of cobalt(II) trichloroacetate, $Co(CCl_3COO)_2$: Cobalt trichloroacetate was synthesized following the procedure for cobalt chloroacetate but with 13.091 g (0.080 mol, 2 equivalents) of trichloroacetic acid dissolved in 100 mL water added dropwise to 5.241 g (0.044 mol, 1.1 equivalents) of cobalt carbonate dissolved in 50 mL water. Additionally, while using a rotary evaporator, the solution was not heated above 50 °C (to minimize the detrimental haloform reaction of trichloroacetate with water to yield carbonate and chloroform). Lastly, the addition of chloroform, after 3 methanol washes, resulted in dissolution of the resin and was subsequently rotovapped before drying under dynamic vacuum for 16 hours to yield 14.69 g (0.0383 mol 96 % yield) $Co(CCl_3COO)_2$ as a pink solid (Anal. Calcd for $Co(CCl_3COO)_2$: C, 13.96; H, 0.50. Found: C, 13.85; H, 0.84.).

Synthesis of Co(OOCR): The aforementioned strategy was found to be generally applicable to other acetate derivatives such as pivalate and propionate.

Glassware Silanization. All syntheses were performed in glassware which had been silanized. The glassware is heated to 160 °C in an oven for several hours, along with a separate glass jar. With the glassware still hot, a solution of 1% chlorotrimethylsilane in toluene by volume was made in the glass jar and then added to the synthesis glassware. The reaction vessel containing the silane solution was then agitated using a Vortex-Genie 2 Lab Mixer for thirty seconds and allowed to sit for 12 hours. The vessel was then rinsed twice with acetone and heated in a 160 °C oven to remove trace acetone.

Reaction 2.1-Co, Ni, Zn: Aqueous Ethanol Synthesis of M_2(dobdc), M = Co, Ni, Zn. The ligand H_4dobdc (10.0 mg, 0.050 mmol) was dissolved in 5 mL ethanol using sonication and cobalt(II) acetate tetrahydrate (44.0 mg, 0.175 mmol), nickel(II) acetate tetrahydrate (44.0 mg, 0.175 mmol), or zinc(II) acetate dihydrate (39.0 mg, 0.175 mmol) was dissolved in 5 mL H_2O

using sonication. The two solutions were combined into a silanized 20 mL vial and agitated for a few seconds using a Vortex-Genie 2 Lab Mixer. The vials were then sealed and suspended into an oil bath already set to 75 °C. After at least two hours, the vials are removed from heat and allowed to cool, after which the supernatant solution was decanted. The crystals were soaked three times in 20 mL of water for six hours at 80 °C, followed by soaking three times in 20 mL of N,N-dimethylformamide (DMF) at 120 °C for six hours, followed by soaking three times in 20 mL of methanol at 60 °C for six hours. After each wash, the solution is decanted and replaced. Fully desolvated M_2(dobdc) crystallites were obtained by heating at 180 °C under dynamic vacuum for 24 h.

Reaction 2.1-Mn: Aqueous Ethanol Synthesis of Mn_2(dobdc). Manipulations involving manganese(II) salts and Mn_2(dobdc) were performed air-free using Schlenk techniques and the reaction was run at four times higher concentration of all reactants relative to M_2(dobdc) synthesis (M = Co, Ni, Zn). The ligand H_4dobdc (40.0 mg, 0.050 mmol) was dissolved in 5 mL ethanol using sonication and manganese(II) acetate tetrahydrate (172.8 mg, 0.70 mmol) was dissolved in 5 mL H_2O. The two solutions were combined into a 50 mL Schlenk flask under inert atmosphere. The flask was suspended into an oil bath already set to 75 °C. After no more than twenty minutes, the flask was removed from heat, allowed to cool, and the supernatant solution was decanted under inert atmosphere. At longer time periods, a different phase can begin forming.

Reaction 2.1-Fe: Aqueous Ethanol Synthesis of Fe_2(dobdc). Manipulations involving iron(II) salts and frameworks were performed in a glovebox equipped for water chemistry. The ligand H_4dobdc (10.0 mg, 0.050 mmol) was dissolved in 5 mL ethanol using sonication and iron(II) acetate tetrahydrate (43.4 mg, 0.175 mmol) was dissolved in 5 mL H_2O. The two solutions were combined into a 20 mL vial. The vial was then sealed, removed from the glovebox and suspended into an oil bath already set to 75 °C. After at least two hours, the vials are removed from heat, allowed to cool, and brought back into the glovebox, after which the supernatant solution was decanted.

Reaction 2.2: Non-Coordinating Base Synthesis of M_2(dobdc), M = Co, Ni, Zn. The ligand H_4dobdc (10.0 mg, 0.050 mmol) was dissolved in 5 mL ethanol using sonication and cobalt(II) tetrafluoroborate hexahydrate (60.2 mg, 0.175 mmol), nickel(II) tetrafluoroborate hexahydrate (60.1 mg, 0.175 mmol), or zinc(II) tetrafluoroborate hydrate (60 mg, 0.2 mmol) was dissolved in 5 mL H_2O using sonication for the synthesis of Co_2(dobdc), Ni_2(dobdc), or Zn_2(dobdc), respectively. The two solutions were combined into a silanized 20 mL vial and agitated for a few seconds using a Vortex-Genie 2 Lab Mixer. The vials were then sealed and suspended into an oil bath already set to 75 °C. After at least two hours, the vials are removed from heat and allowed to cool, after which the supernatant solution was decanted.

Reaction 2.3: Non-Coordinating Buffer Synthesis of Co_2(dobdc). First, the buffer 3-(N-morpholino)propanesulfonic acid (MOPS) (0.419 mg, 2.0 mmol) was dissolved in 3 mL water using sonication. 1M KOH was added (1.204 mL, 1.204 mmol) to raise the solution pH to 7. Finally, 0.796 mL water was added to bring the total amount of water to 5 mL. The ligand H_4dobdc (10.0 mg, 0.050 mmol) was dissolved in 5 mL ethanol using sonication and cobalt(II) acetate tetrahydrate (44 mg, 0.175 mmol), cobalt(II) formate (33 mg, 0.175 mmol), cobalt(II) chloroacetate (43 mg, 0.175 mmol) or cobalt(II) trichloroacetate (67.8 mg, 0.175 mmol) was dissolved in 5 mL of the pH 7 solution using sonication. The metal salt should be added to the buffered solution at the correct pH, lest the addition of 1M KOH precipitate local cobalt hydroxide at regions of high pH. The metal salt solution and ligand solution were combined into a silanized 20 mL vial and agitated for a few seconds using a Vortex-Genie 2 Lab Mixer. The vials were then

sealed and suspended into an oil bath already set to 75 °C. After at least two hours, the vials are removed from heat and allowed to cool, after which the supernatant solution was decanted. The crystals were soaked three times in 20 mL of water for six hours at 80 °C, followed by soaking three times in 20 mL of N,N-dimethylformamide (DMF) at 120 °C for six hours, followed by three days of Soxhlet extraction with methanol replaced daily. After each wash, the solution is decanted and replaced. Fully desolvated M_2(dobdc) crystallites were obtained by heating at 180 °C under dynamic vacuum for 24 h. Langmuir surface areas calculated from N_2 77K isotherms using Micromeritics software were found to be 1293 m^2/g, 1389 m^2/g, 1302 m^2/g, and 1414 m^2/g for Co_2(dobdc) synthesized using cobalt(II) acetate, cobalt(II) formate, cobalt(II) chloroacetate, and cobalt(II) trichloroacetate, respectively.

Gas Adsorption Measurements. Gas adsorption isotherms with pressures in the range 0−1 bar were measured using a volumetric method on a Micromeritics ASAP 2420 instrument. Samples were transferred under a N_2 atmosphere to tared analysis tubes and then capped with a Transeal. The samples were evacuated at the original activation temperature until the outgas rate was <1 μbar/min, at which point the tube was weighed to determine the mass of the activated sample. The tube was transferred to the analysis port of the instrument, and the outgas rate was again checked to ensure that it was below 1 μbar/min. Ultrahigh purity N_2 was used for all adsorption measurements. For all isotherms, warm and cold free spaces were measured using He. The N2 isotherms at 77 K were measured in liquid nitrogen baths. Oil-free vacuum pumps and oil-free pressure regulators were used for all measurements. Langmuir surface areas were determined using Micromeritics software.

Density Functional Theory Calculations. The 106-atom cluster proposed by Verma et al. for Fe_2(dobdc) was extended to a larger 125-atom cluster calculations.[30] An analogous Co_2(dobdc) cluster was cut out of the periodic M_2(dobdc) structures optimized with periodic DFT by Lee et al.[31] All linkers in the 125-atom cluster were modeled as salicylate, compared to some truncated salicylates in the 106-atom cluster. Five additional water molecules were also added to the cluster model to fill the open-metal sites along the helix since our objective is to model the MOF during synthesis and not during gas adsorption after evacuation. The effect of replacing a terminal or middle-helix ligand with the target binding molecule (or combination of molecules) was computed. The protonation states of non-coordinating oxygen atoms on ligands were chosen to maintain an overall charge neutral cluster. For each binding energy calculation, the formation energy of three structures was computed and used: 1) the metal helix without the truncated ligand molecule; 2) the target binding molecule(s) and 3) the metal helix with the target binding molecule(s). The target binding group was either acetate or a combination of acetate and water. Calculations for this cluster were performed with the def2-TZVP basis set and the M06-L functional as implemented in the Gaussian 09 software package.[32,33]

2.3 Results and Discussion

I began my investigation of the crystallization behavior of the M_2(dobdc) series of frameworks (Fig. 1.1) by replicating the literature solvothermal syntheses of Co_2(dobdc)[28] and Zn_2(dobdc).[27] As reported, the syntheses produce crystals best described as a polydisperse set of long rods. An example SEM image of Co_2(dobdc) following literature single-crystal synthesis is displayed in Figure 2.1. In fact, all reported syntheses for M_2(dobdc) generate either long rod morphologies or very polycrystalline particles.[34–43] Previous work on Co_2(dobdc) and Zn_2(dobdc) has determined via single crystal analysis that the structure pore direction (that is, the *c*-axis in Fig. 1.1) aligns

with the long axis of the morphology.[35] This is undesirable for several reasons, all arising from the inherent material anisotropy. For very long crystallites, the one-dimensional path length is very long: per volume, higher aspect ratio (defined here as crystal length to crystal width) crystallites have fewer pores, maximizing the negative effects of any defects or pore blockages. Any external faces of the crystallite that are parallel to the one-dimensional pores are expected to have significantly lower transport rates for guest molecules into the crystallite, relative to external surfaces that intersect (and thus are open to) the one-dimensional channels. The validity of this assumption is tested in Chapter 5, but it is worth noting that the literature precedent for the expanded-pore variant Zn_2(dobpdc) has orders of magnitude faster transport along the one-dimensional channels than perpendicular to the channel direction, even with measurable defect-induced transport through the pore walls.[44]

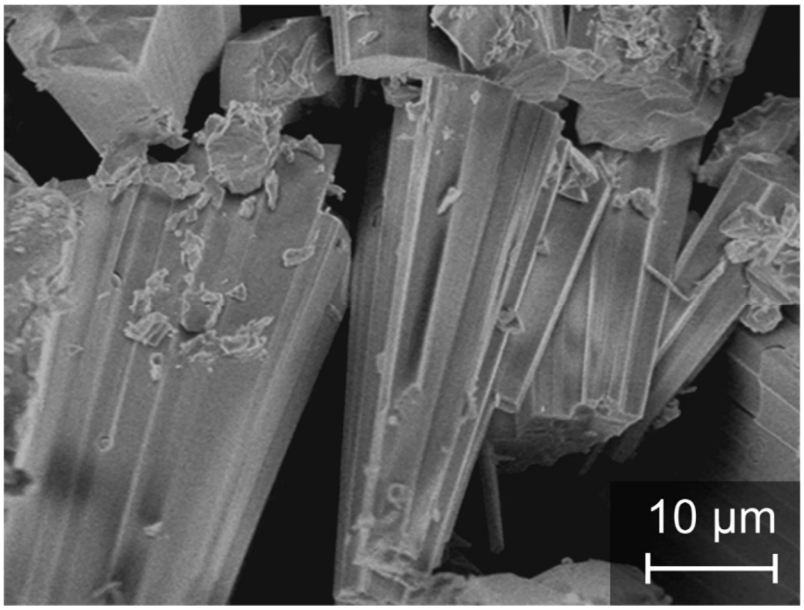

Figure 2.1. SEM micrograph of Co_2(dobdc) crystallites synthesized solvothermally, featuring long rod-like domains.

Predicted Morphology for Co_2(dobdc). It is thus worth examining why single-crystalline, high-quality M_2(dobdc) tends to grow into long needles, and what factors may be able to provide alternate growth habits. As discussed in Chapter 1, there are several popular theories for crystal habit prediction. While the Wulff construction can provide equilibrium morphologies, it requires a priori knowledge of the surface energy relating to various facets and is only strictly applicable to very small crystallites.[45] As a result, for microscale crystallites, it is assumed that the faces present on a crystallite are determined by the kinetics of growth: the faces that are slowest to grow are the faces represented in the final morphology. Hartman and Perdok's periodic-bond chain theory can generate theoretical morphologies based off predicted slower kinetics but requires the determination of lattice and slice energies for a crystal.[46] An easier construction is the Bravais-Friedel-Donnay-Harker (BFDH) crystal morphology, an approximation based solely on the geometrical considerations of the unit cell parameters and symmetry operators.[47,48] I used the software package Mercury[49] to generate a BFDH shape for Co_2(dobdc), displayed in Figure 2.2. The resultant shape is a truncated rod of lower aspect ratio than the observed solvothermal growth.

The largest factor missing in this predicted morphology is that of the environmental growth medium. It is thus crucial to describe solution effects to be able to understand the typical growth habits of M_2(dobdc) grown from solution. Of note, the synthesis (and, indeed, metal–organic framework syntheses in general) does not need to be performed in solution. Other synthetic options include ball-milling[50,51] or crystallization from melts.[52] However, as the vast majority of metal–organic framework syntheses are solution-based,[26] I chose to pursue an understanding of the fundamental solution variables, so that the work will be as widely applicable as possible. Gaining an understanding of the way solution variables interacts has the potential to influence and improve processing for an enormous number of different materials.

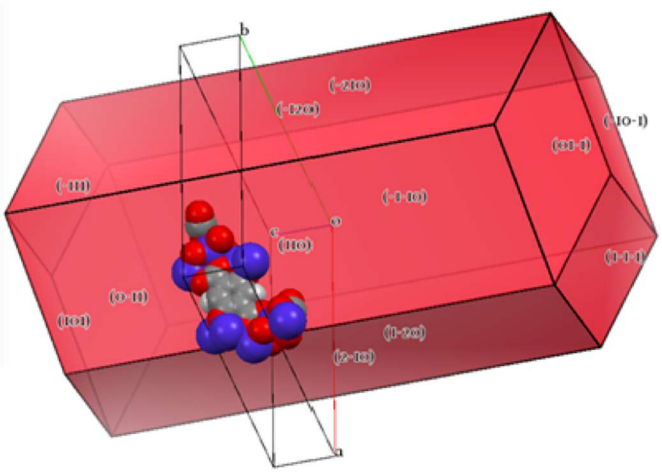

Figure 2.2. The predicted morphology for Co_2(dobdc) has a significantly truncated, dodecahedral morphology where each facet is tetragonal. Predicted BFDH faces are listed.

Synthetic Design Choices. Systematically modifying a solvothermal reaction did not appear to be the best route to studying crystallization behavior. At the simplest level, all metal–organic frameworks can be described as Lewis acidic metal ions or clusters bridged by Lewis basic ligands. For the vast majority of reported frameworks, the organic ligands also behave as Brønsted-Lowry acids and/or bases during synthesis. For the specific example of the formation of M_2(dobdc), the ligand must go from its initial protonation state to fully deprotonated during the synthesis. The typical solvothermal reaction of a metal nitrate or chloride with the fully protonated ligand requires the thermal decomposition of N,N-dimethylformamide (DMF) to provide a base.[27] This decomposition process introduces species into solution, the concentrations of which vary as a function of time.[53,54] Further, the solvent is expensive and toxic,[55] and its usage in synthesis generates significant organic waste. Fundamentally, solvent decomposition adds an unnecessary layer of complexity to the crystallization process. Practically speaking, developing good methods of synthesizing metal–organic frameworks without the use of expensive organic solvents could conceivably lead to the adoption and development of environmentally-friendly industrial synthesis procedures. Replacing DMF with water as the main solvent of choice allows the additional benefit of utilizing pre-existing quantitative understanding of pH. However, the solubility of the linker H_4dobdc in water is quite low, severely limiting the maximum concentration of reactants in solution.[56] By including ethanol as a co-solvent, we may retain a quantitative understanding of pH

while allowing better solubility of all reactants.[57,58] Without the decomposition of DMF to provide dimethylformamide, the synthesis must include a Brønsted base; to this end, I chose to utilize cobalt(II) acetate as the metal source, both for simplicity and availability. This is a synthesis designed to have as few different types of molecules as possible, consisting of metal cations, acetate anions, the ligand, and solvent molecules. By including the Brønsted base in the metal salt itself, I intended to simplify the reaction space and the types of molecules involved.

Aqueous Ethanol Synthesis. For reasons described above, as a comparison to the single crystal synthesis displayed in Figure 2.1, I created an analogous synthesis in 1:1 water:ethanol using cobalt acetate and H_4dobdc, yielding readily dispersible orange particles. Powder X-ray diffraction of the precipitated solid is consistent with expected phase, Co_2(dobdc) (Fig. 2.3). Optical microscopy of the particles indicates that they have similar size and morphology. Uniform reflectance or transmittance of polarized light across entire crystallites indicates they are single crystals (Fig. 2.S1). Furthermore, SEM imaging of the crystallites displays monodisperse polyhedra with clearly defined facets (Fig. 2.4).

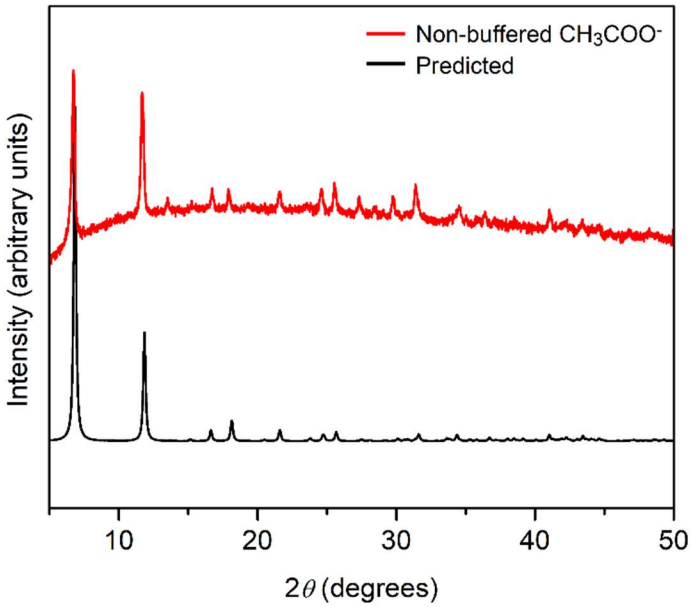

Figure 2.3. The powder X-ray diffraction pattern confirms that the new non-solvothermal water:ethanol synthetic route yields single-phase Co_2(dobdc) crystallites.

These Co_2(dobdc) crystallites clearly exhibit different morphology from the solvothermally grown material in Figure 2.1 or the predicted BFDH morphology displayed in Figure 2.2. In addition to their dramatically short, truncated shape, they appear to have pentagonal facets. While current image recognition software are capable of differentiating shapes and assigning faces to common polyhedra,[59,60] such as cubes, the faces and geometry of these Co_2(dobdc) crystallites are uncommon and cannot be readily analyzed by available high throughput software. A new method was needed to enable reconstruction of the three-dimensional shapes from two-dimensional images for arbitrary facets. Using the raw image data and a symmetry-based shape generator[61], these polyhedra were found to be pentagonal dodecahedra that are elongated along a 3-fold axis (Fig. 2.4). The symmetry of the morphology is consistent with the S_6 point group of the framework's

space group: $R\bar{3}$. The only three-fold axis of symmetry observed in the crystal morphology corresponds to the only three-fold axis found in $R\bar{3}$, namely the *c*-axis. A self-consistent set of Miller indices can be generated with symmetry operators and the correct choice of one of each of the side faces and the top face. Here, the {1 0 0} family of planes and the {4 0 1} family of planes can describe the morphology of the pentagonal dodecahedra (Fig. 2, at left). The full set of planes generated is a set of six indices to describe the facets parallel to the *c*-axis, {(1 −1 0), (–1 1 0), (1 0 0), (−1 0 0), (0 1 0), (0 −1 0)} and a set of six indices describing facets which intersect the *c*-axis to cap the crystallite {(4 0 1), (−4 0 –1), (0 −4 1), (0 4 −1), (4 –4 1), (4 −4 −1)} (blue and purple, respectively, in Fig. 2.4).

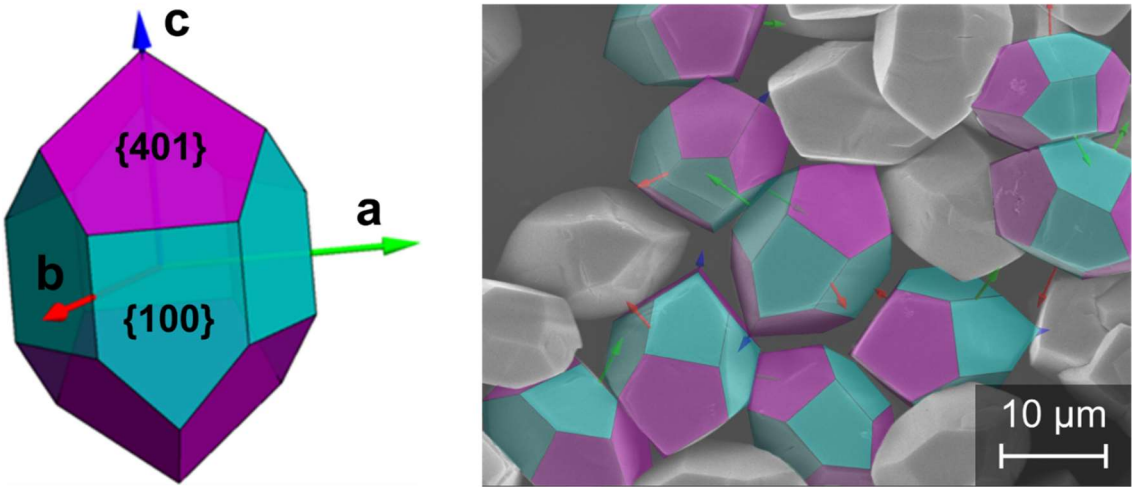

Figure 2.4. At left, the pentagonal dodecahedra morphology with axes and generating faces overlaid; at right, this morphology projected onto a set of Co_2(dobdc) crystallites arranged at different angles.

Geometric overlaying from multiple angles allows assignment of morphology but it does not provide information about specific surface chemistry, merely recreation of the three-dimensional shape. Some care must be taken with this approach, as the method reconstructs polyhedra from two-dimensional projections of crystals oriented at many angles relative to the viewing axis. For example, nearly all information about faces intersecting the *c*-axis is lost when the crystals are aligned directly along the three-fold axis (Figure 2.S2–2.S3). Given enough randomly distributed particles, crystallite morphology may be reconstructed with confidence. The low morphological polydispersity and truncated shape of the rods indicated that some variable not normally present in solvothermal syntheses is controlling the crystal shape. One possible contender is the high concentration of acetate anions in solution, which are normally absent in solvothermal syntheses. Previous literature on coordination modulation across a variety of different frameworks has found that acetate can modulate synthesis by interacting with metals as a Lewis base, which can in turn influence the interactions between the metals and ligands. By design, acetate here also acts as a Brønsted base to deprotonate the ligand. It is impossible to know a priori if the presence of acetate is important for the synthesis of monodisperse, low aspect ratio crystallites without eliminating acetate from the system while still allowing the reaction to proceed. If the presence of acetate is required for monodisperse crystallites, it could be acting in either a coordinating manner, such that interactions between acetate and metal ions regulate crystallite shape, or a pH-controlling manner,

such that the extent of linker deprotonation resulting from the presence of acetate is optimal for the shape of the observed crystallites. Either role could be the controlling solution handle. Discriminating between these two proposed roles requires removing acetate from solution while letting the reaction proceed and without introducing additional molecules which could coordinate to metal cations. Thus, a control test removing the coordinating acetate requires a non-coordinating method of pH control.

Weakly-Coordinating pH Control. The first non-coordinating method of pH control attempted was the addition of a weakly-coordinating base, 2,6-Lutidine.[62] A non-coordinating version of the synthesis was formed by using a tetrafluoroborate as an anion in the place of acetate and adding 2,6-Lutidine at the concentration that acetate is present in the original reaction. This control test yields very different morphologies between the two syntheses: the crystal monodispersity is absent for the non-coordinating version, and the average crystal aspect ratio is much longer (Fig. 2.5). However, the comparison is not perfect. The pK_a of 2,6-Lutidine is around 6.6[63] while that of acetate is 4.76[64], so at an equal number of equivalents of 2,6-Lutidine versus acetate, the non-coordinating version of the reaction is run at higher pH.

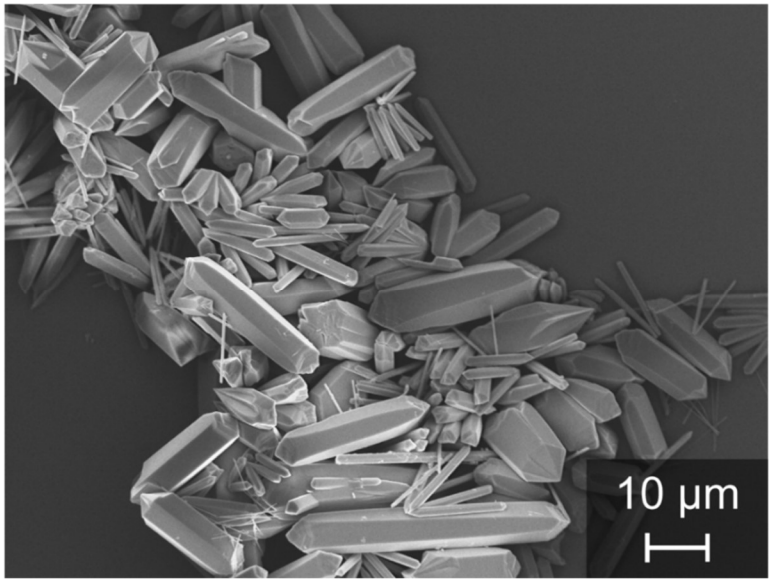

Figure 2.5. The set of Co_2(dobdc) crystallites synthesized in water:ethanol with 2,6-Lutidine acting as a deprotonation agent instead of acetate leads to polydisperse, high aspect ratio crystallites.

A stricter comparison demands identical solution pH between the control tests. In analytical chemistry, one traditional way to do this is by buffering the solution. Buffers resist changes in pH upon addition of acidic or basic components.[64] While this is not a traditional method of synthesizing metal–organic frameworks, several advantages were apparent immediately. The pH can be chosen carefully to control the protonation state of the ligand. However, effective buffers require a fairly high concentration in solution. Any molecule that is a Brønsted acid or base is thus a Lewis base or acid, and any such molecule that can coordinate to metal ions would be expected to severely change the metal ion speciation in solution. This concern prompted the use of non-coordinating buffers.[65,66] It was not obvious a priori that the buffers could be included without again changing many solution variables at once; for instance, adding a buffer increases the ionic

strength of solution, which can affect speciation, dissociation constants and reactant solubility.[67–69] It was thus important to examine the effect of including a non-coordinating buffer on the crystallite morphology while acetate is present in solution. The buffered reaction was held to pH 7, while the pH of the non-buffered reaction drops slightly as the ligand is deprotonated. There is no discernable difference in the morphology observed with and without buffers (Fig. 2.6a-b), suggesting that these buffers may be used as pH control with negligible participation in relevant metal complexation, at least in this pH range. The crystallites synthesized in a buffered solution are slightly smaller, which suggests a slightly higher nucleation rate. This is likely because the pH remains higher on average for the buffered reaction, and thus the free ligand in solution is on average less protonated.

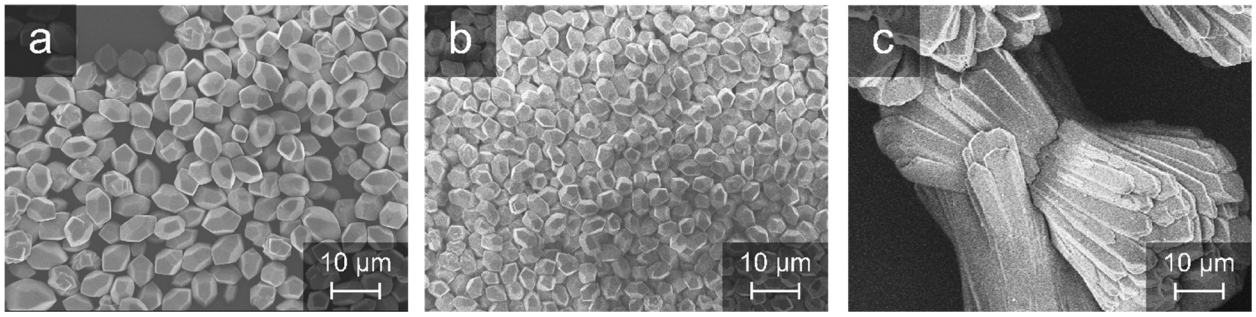

Figure 2.6. (a) Co_2(dobdc) synthesized with cobalt(II) acetate without buffer; (b) Co_2(dobdc) synthesized with cobalt(II) acetate buffered to pH 7; (c) Co_2(dobdc) synthesized with cobalt(II) tetrafluoroborate buffered to pH 7.

Using the buffer allows the addition or subtraction of complexing agents at the same pH. Continuing at neutral pH, the same reaction may be run with a weakly-coordinating anion, such as tetrafluoroborate. Without acetate present, the synthesis produces long, polycrystalline and polydisperse rods (Fig. 2.6c). Thus, the observed synthetic control requires the presence of acetate. Moreover, using non-coordinating buffer reveals the mechanism of control: because the reactions with and without acetate are buffered to the same pH, the mechanism of control must be coordinative and not a function of acetate acting as a base. The fact that the crystals are truncated along the *c*-axis suggests that competitive coordination must be happening in this direction of growth. Notably, using other anions of varying coordinative strength also leads to morphological control and changes the crystal facets (Figure 2.S4). Having a coordinative group on the anion that matches that of the linker is thus not necessary for homogeneous, controlled morphologies. The set of non-coordinating buffers may also be used to systematically vary the solution pH. The full range of the buffers (pH 3 – 11) is wider than is useful for this particular synthesis: because cobalt hydroxide readily forms at pH ~8,[70] I did not go above pH 7, while reactions buffered below the pK_a of the carboxylate functionalities do not proceed in appreciable amounts. A series of comparisons at pH 5, 6, and 7 for the buffered acetate reaction demonstrates that aspect ratio tends to increase with lower pH (Figure 2.7). A comparison of pH variation with non-coordinating anions substituted for acetate displays no change in crystal morphology (Figure 2.S5). Although lowering the pH affects the protonation state of both acetate and ligand in solution and appears to slow overall formation, the morphological changes here arise from increased protonation of acetate. As acetate is protonated, it is less able to compete with the ligand during growth, leading

to longer crystallites, but this lack of coordinating control also leads to greater morphological dispersity.

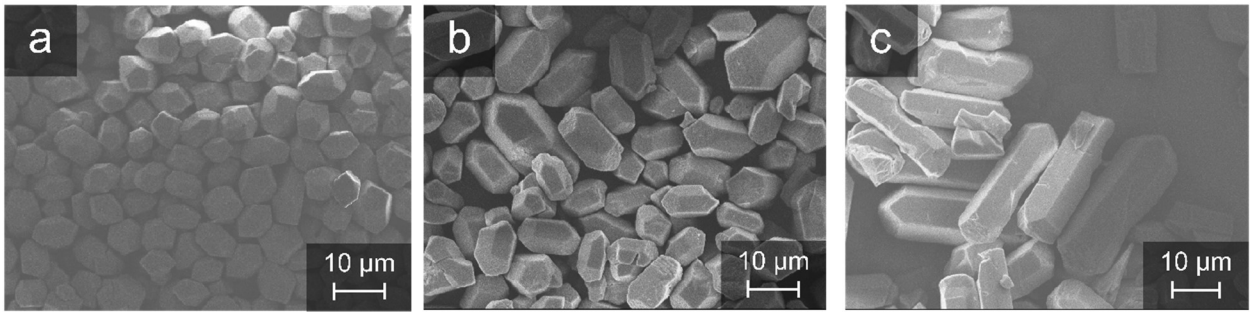

Figure 2.7. Co_2(dobdc) synthesized with cobalt(II) acetate buffered to (a) pH 6.5; (b) pH 6; (c) pH 5.5.

Density Functional Theory Calculations of Competitive Binding. Density functional calculations were then used to study the binding of both acetate and the ligand to cobalt-helices to test the hypothesis of competitive acetate binding with calculations. A cluster model of cobalt sites was based on the 106-atom cluster of the cobalt-helix in the MOF proposed and validated by the work of Verma et al. and others.[30] The cluster used here resembles the cluster of Verma et al. in that the helix contains five cobalt metals and seven ligand molecules where all ligand oxygen atoms bound to metals are deprotonated. There are, however, some differences between the two models. All of the ligands in the cluster used here are full salicylate anions, while in the Verma et al. cluster some of the ligands are missing phenol or carboxylate groups. Verma et al. omitted these groups because they did not participate in bonding with the five present cobalt atoms. Here, these functional groups are included in order to be able to quantitatively compare the replacement of ligand molecules at different positions in the helix as discussed in the subsequent paragraph. A requirement of this comparison is that the ligand molecules be identical. In addition, all open-metal cobalt sites in our cluster are occupied by water molecules to better reflect the solvated environment in which the metal helices are formed. The additional ligand and water molecules lead to a 125-atom cluster model, different views of which are shown in Figures 2.8a, 2.8c and 2.8e.

Starting from the aforementioned 125-atom cluster, ligand molecules were removed and replaced by both acetate and water molecules. Then, the competitive binding energy was calculated at the DFT level of theory (see the experimental section for more details). The clusters shown in Figure 2.8a-d show competitive bidentate and monodentate acetate binding at the terminal end of the metal helix, and the corresponding competitive binding energies are given in Table 2.1. In the case of monodentate acetate binding (Figure 2.8d), an additional water molecule is also added to fill an open coordination site on the exposed metal. Both bidentate- and monodentate-bound acetate groups can compete favorably with the ligand. The model of the monodentate-bound terminal acetate case is particularly useful because it facilitates a comparison on the basis of exact substituted molecules with the result given in Table 2.2 of bidentate acetate and water binding in the middle of a cobalt-helix, shown in Figures 2.8e-f. According to this comparison, acetate and water binding at the terminal helix end may be 25 kJ/mol more competitive than in the middle of the helix. A similar comparison can be made between the bidentate cases, leading us to conclude that bidentate acetate binding may be 13 kJ/mol more favorable at the terminal end than in the

middle of the helix. Comparing all three cases leads to the conclusion that, depending on how acetate binds, its competitive advantage over the ligand can nearly double (25 kJ/mol vs 13 kJ/mol). This finding could have interesting implications for the kinetics of cluster growth in solution. While monodentate acetate and water binding was found to be the most energetically competitive scenario, the single acetate–cobalt bond may be dislodged more often than the two bonds formed in the bidentate scenario. However, the findings also suggest that the monodentate scenario is stabilized by the co-adsorbing water, which could also play a role in determining the kinetics of replacement.

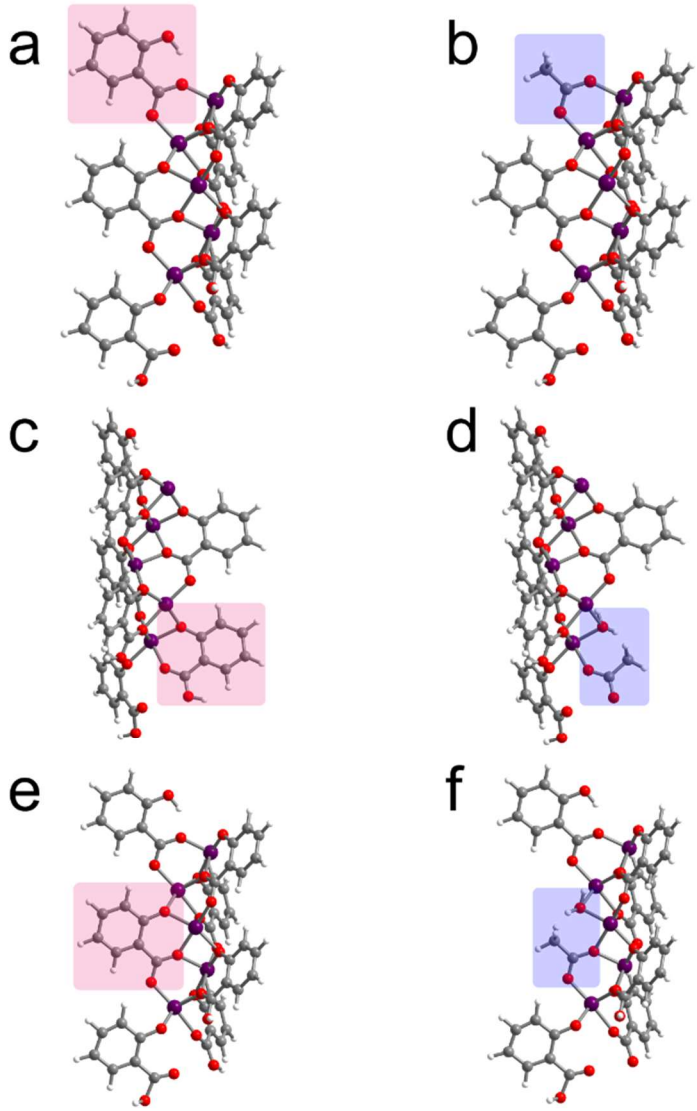

Figure 2.8. Helices used for DFT binding energy calculations. Cobalt, oxygen, carbon and hydrogen atoms are shown in purple, red, grey and white, respectively. Replaced bidentate terminal, monodentate terminal and middle-helix ligand molecules are highlighted in red in (a), (c) and (e) respectively, while target binding molecules are highlighted in blue in (b), (d) and (f). In (b), the ligand is replaced by acetate, while in (d) and (f) the ligand is replaced by a combination of acetate and water.

Table 2.1. Competitive Binding Energy at the Terminal End of a Co-Helix.

	E_b (kJ/mol)	$E_b - E_{b,\,ligand}$ (kJ/mol)
$[C_7O_3H_5]^-$	−85	---
$[CH_3COO]$- (bidentate)	–113	–28
$[CH_3COO]$- (monodentate) + H_2O	−125	−40

Table 2.2. Competitive Binding Energy at the Middle of a Co-Helix.

	E_b (kJ/mol)	$E_b - E_{b,\,ligand}$ (kJ/mol)
$[C_7O_3H_4]^{2-}$	−583	---
$[CH_3COO]$- (bidentate) + H_2O	–598	−15

Predicted Morphology with Counter Ions. Because experimental and theoretical results suggested that acetate molecules control morphology via coordination during crystallite growth, I believed it would be possible to change the resulting crystallite morphology by changing the binding strength of the acetate anion. Unlike the other anions found to control morphology, acetate lends itself readily to chemical modification by replacing the methyl group with more electron-donating or electron-withdrawing functionalities. I therefore synthesized a series of cobalt(II) salts with carboxylate-based anions of varying pK_a values[64] (Table 2.S1) using modified literature routes.[71,72] Here I use pK_a as a proxy for coordinating strength, as the acidity of the carboxylate is increased with the addition of electronegative substituents through inductive electron withdrawal.[73] The anions chosen as a series were acetate, formate, chloroacetate, and trichloroacetate. Due to their low pK_a, in each case the anions should effectively be fully deprotonated during syntheses buffered to pH 7. Some care needs to be taken in synthesizing and using trichloroacetate anions, as these can undergo hydrolysis via the haloform reaction at elevated temperature in water. However, on the time scale and temperature scale of the Co_2(dobdc) synthesis, this side reaction is negligible[74].

By substituting these metal salts into our buffered synthesis, we were able to synthesize monodisperse crystallites of varying aspect ratio. The crystallites all behave as single crystals under the optical microscope, indicating that the synthesis succeeds in maintaining single (Fig. 2.S6–2.S8). No evidence of buffer incorporation is seen via infrared spectroscopy (Fig. 2.S9–2.S10). Powder X-ray diffraction indicates that all crystallites are Co_2(dobdc) (Figure 2.9). As predicted, aspect ratio is inversely related to the anion pK_a. As the pK_a increases in the order of trichloroacetate < chloroacetate < formate < acetate, the corresponding crystallite aspect ratio decreases (Fig. 2.10). Notably, as these syntheses are buffered to the same pH, these effects may be ascribed directly to coordination during growth. Pulling electron density away from the carboxylate functional group decreases its ability to compete with ligand binding, reducing truncation in the c-direction and resulting in longer crystallites. Interestingly, the crystallite facets

are the same across the series of anions, indicating minimization of the surface energy of these facets (Fig. 2.S11).

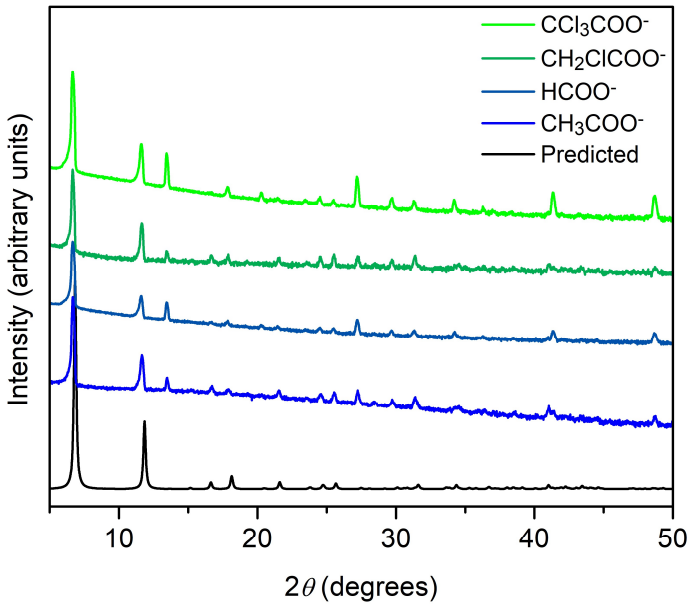

Figure 2.9. Powder X-ray diffraction patterns for Co_2(dobdc) synthesized using different carboxylate-containing anions.

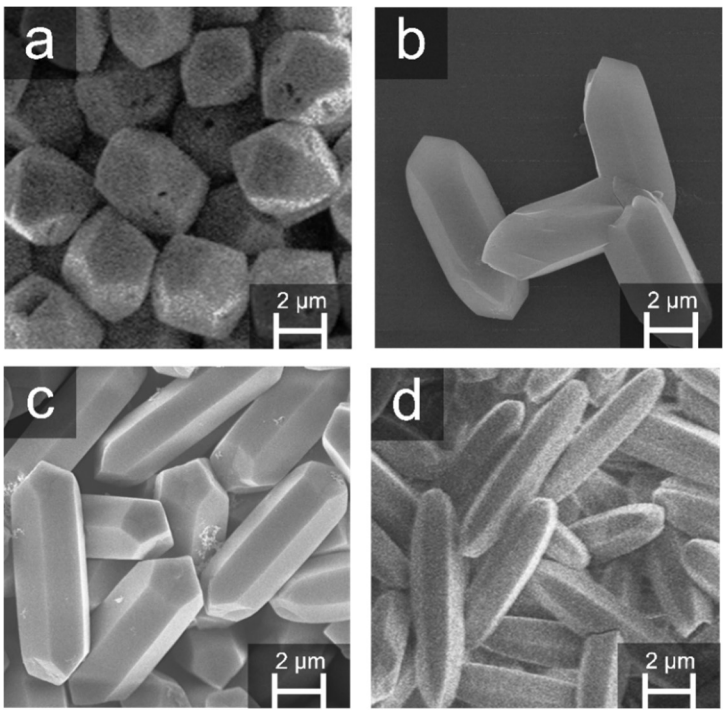

Figure 2.10. Co_2(dobdc) synthesized in water/ethanol buffered to pH 7 with different carboxylate metal salts: (a) cobalt(II) acetate (b) cobalt(II) formate (c) cobalt(II) chloroacetate (d) cobalt(II) trichloroacetate

For further analysis, a given crystallite can be modeled in Mathematica to calculate pore length distribution within the material. From a given set of Miller indices and unit cell dimensions, as well as particle length and width, it is possible to derive equations for a set of planes that define the crystallite shape as the space bordered by their intersections. Subtracting one set of three-fold symmetric faces from the other yields a three-dimensional representation of *c*-axis length of the crystallite. This object can be integrated to yield the distribution of path lengths in the crystallite. (Fig. 2.S12). The facets do begin to lose their sharpness at the least strongly coordinating anion, trichloroacetate, suggesting that weakly-coordinating anions may become negligible in coordination at low enough pKa values. With even more weakly-coordinating anions, as studied earlier, morphological monodispersity is lost. In general, crystallites tend to have similar volumes between syntheses and nearly identical, very high yields. The volume of the crystallites does increase slightly as the anionic pKa decreases in the reaction, which could imply a subtle lowering of the nucleation rate. While I succeeded in synthesizing cobalt(II) salts with increased electron density on the carboxylate, including cobalt(II) pivalate and cobalt(II) propionate, the metal salts were fairly insoluble in the solvent mixture, impeding the introduction of metal cations into solution.

Metal Analogue Comparison. All foregoing results were demonstrated for the cobalt analogue of the framework; however, the metal series that can form this structure type includes magnesium, manganese, iron, nickel, copper, zinc, and cadmium. One obvious question is how the metal identity affects the resulting morphology under similar conditions. To probe this, the same reaction was run with the metal(II) acetate of each known variant of M_2(dobdc) with the exception of cadmium[75]. Of these, the iron, nickel, and zinc frameworks also formed easily (Fig. 2.11). For the same reaction time, temperature, and molar equivalency, the reaction led to striking differences between the metal analogues. The solubility of all reactants is extremely similar between the different solutions and the pH is nearly identical, suggesting that the morphological differences observed may come from differences in coordination. However, it is difficult to ascribe definitive reasons to the variation in morphology. The observed single-crystalline domains tend to increase with metal lability,[76] in the order nickel < cobalt < zinc < iron.[77] For each single-crystalline domain, the *c*-axis growth appears to be truncated most for the least labile metals. The differences in morphology between the metals, then, is likely a complex counterbalancing of coordination equilibria, including the dynamics of exchange for the metal and ligand versus the dynamics of exchange for the metal and acetate. The manganese analogue required higher concentration to form but also required the synthesis to be stopped after no more than twenty minutes, at which point the reaction mixture would change color and a different crystalline phase formed. Similarly, the magnesium analogue would only form at significantly higher concentrations and only in unsilanized glassware. Further metal-based trends, discussion of surfaces and induction of nucleation will be discussed in Chapter 3. While the full suite of weakly-coordinating buffered tests was only run for Co_2(dobdc) formation, above, both the nickel and the zinc analogues were also synthesized using 2,6-Lutidine and the tetrafluoroborate salt in place of metal(II) acetate. In all three cases, the crystallite domain size increases in these non-coordinating syntheses relative to that of the aqueous ethanol synthesis by up to 10–100X (Fig. 2.12), suggesting that non-coordinating syntheses may be a generalizable route towards large crystals for diffusional or single crystal diffraction studies.

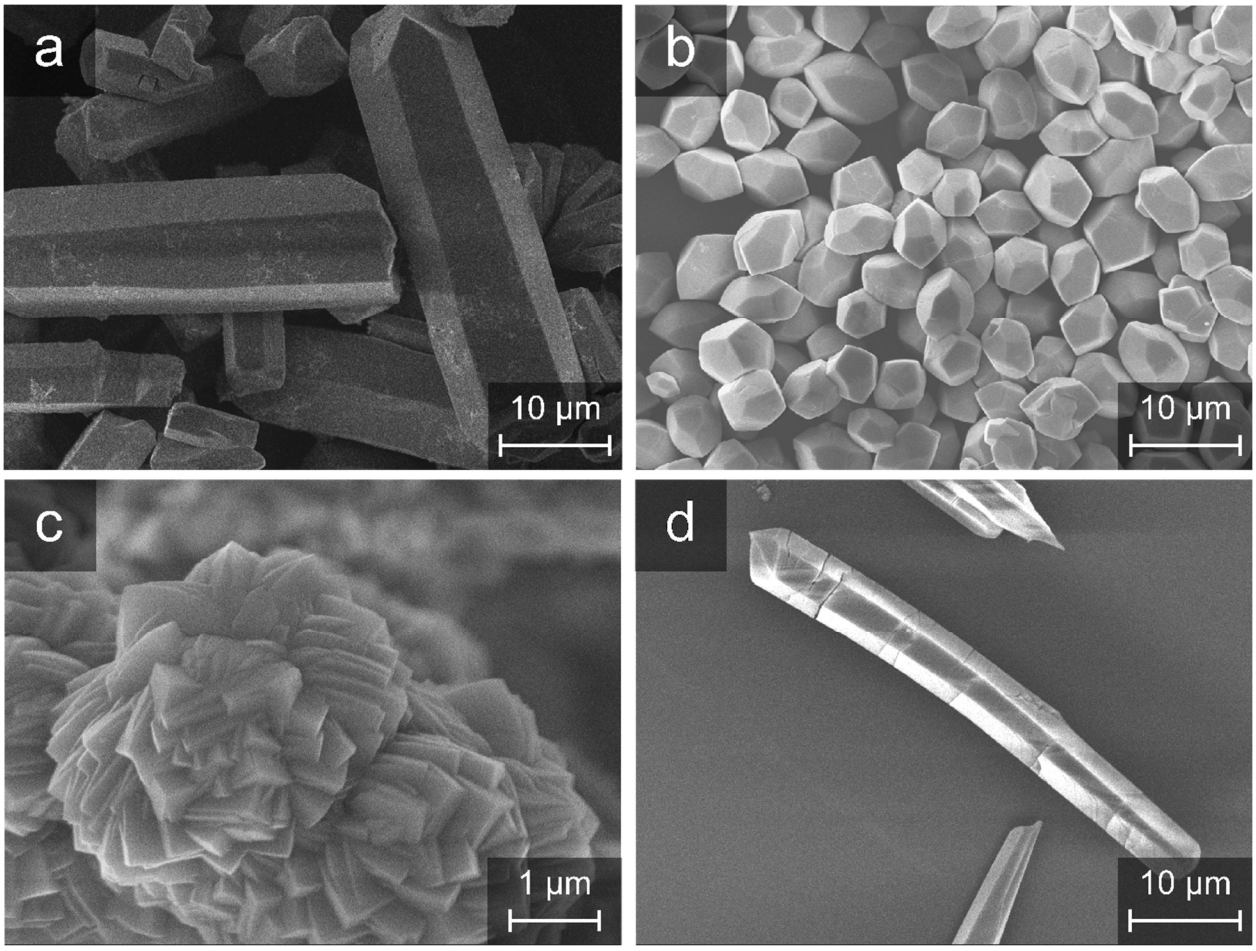

Figure 2.11. SEM micrographs of (a) Fe_2(dobdc) (b) Co_2(dobdc) (c) Ni_2(dobdc) and (d) Zn_2(dobdc) synthesized in aqueous ethanol using the corresponding metal(II) acetate precursor. Note the significantly smaller scale bar for Ni_2(dobdc) in (c): crystallite domain sizes are in the hundreds of nanometers.

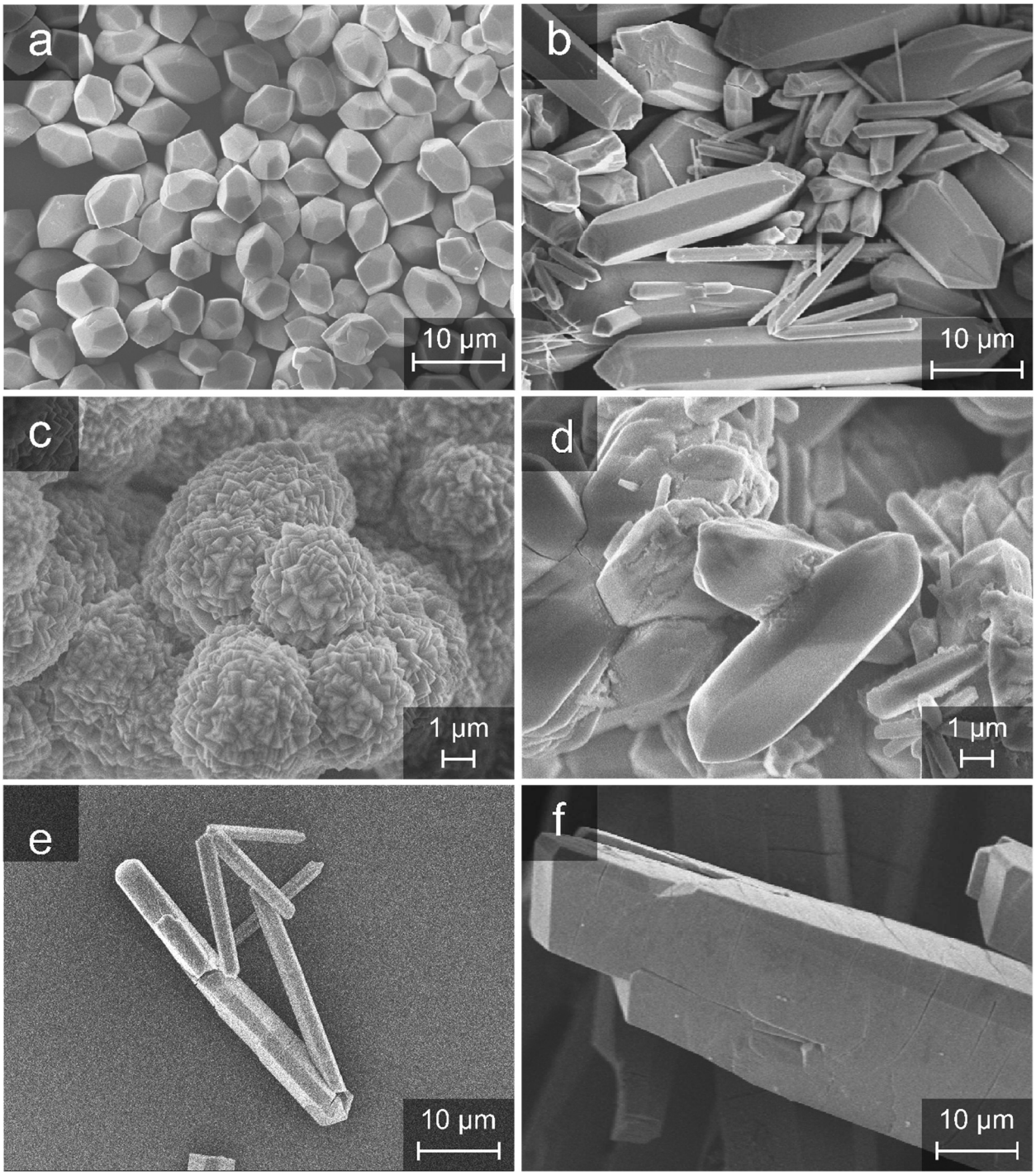

Figure 2.12. Left column (comprising (a), (c), (e) is M_2(dobdc) synthesized using the metal(II) acetate; right column (comprising (b), (d), (f) is M_2(dobdc) synthesized using the metal(II) tetrafluoroborate with 2,6-Lutidine added for pH control. (a) and (b) are Co_2(dobdc), (c) and (d) are Ni_2(dobdc), and (e) and (f) are Zn_2(dobdc). In all cases, the weakly-coordinating synthesis leads to significantly larger crystallite domains.

2.4 Outlook and Conclusions

These results demonstrate a new synthetic platform for metal–organic framework synthesis, in which non-coordinating pH control via weakly-coordinating bases or buffers allow a deliberate separation of protonation and coordination equilibria. This separation of equilibria is here used as both a tool of fundamental study and a way of accessing desired morphology in a predictive fashion. Targeting pH and metal complexation separately allows understanding of how solution variables interact as well as a new way to pinpoint which equilibrium is required for a desired reaction handle. In the specific case of Co2(dobdc), the resultant solution handle, which leads to unprecedented low aspect ratio single-crystalline particles, is the presence of acetate. In fact, the aqueous ethanol/acetate synthesis forms the lowest aspect ratio single-crystalline Co2(dobdc) reported. Density functional theory confirms that this morphological control stems from coordinating anions in solution, which engage in anisotropic competitive binding during crystallite growth. The degree of interaction may be tuned by varying the electron density on the interacting functional group, allowing access to monodisperse sets of crystallites with varying aspect ratio and thus desired crystalline path length. Using weakly-coordinating bases is a widely applicable strategy in which removing all non-solvent competitive coordination can allow for very large crystallites and here is demonstrated across multiple metal analogues of M_2(dobdc).

Although the specifics of the synthesis strategy must be altered between different metals and frameworks, the general strategy is in theory very widely applicable. As pH can be set and held, the desired solution pH will certainly vary between different frameworks. If the solution is buffered to a low enough pH such that all Brønsted acid functionalities are protonated for a given ligand, framework synthesis will proceed extremely slowly, if at all; on the other hand, at a high enough pH for all functionalities to be deprotonated on average, framework formation proceeds extremely quickly, resulting in nanoparticles. The pH range is also dictated by the choice of metal, as different metals have different proclivities to form hydroxides and oxides from water. Using non-coordinating buffers allows the prospect of matching the coordinating strength of the counterion to the lability of the metal. The syntheses described here are done in a water/alcohol solution, which precludes easily hydrolyzable frameworks, including many metal-oxo cluster-based MOFs. However, there is nothing inherent to this strategy that requires the use of water, merely the use of weakly- or non-coordinating control of hydrogen ion activity within the solvent medium. Thus, while water allows for a quantitative measure of pH, the method may be extended in theory to any solvent.

2.5 Acknowledgments

This work was supported by ExxonMobil Research and Engineering Company. I thank Rodi Torres-Gavosto, Miguel Gonzalez, and Rebecca Siegelman for experimental assistance, discussion, and ideas. All density functional theory calculations were done by Sudi Jawahery and Bess Vlaisavljevich. I thank Simon Weston and Joe Falkowski for helpful discussion, feedback and suggestions, including but not limited to the use of 2,6-Lutidine as a weakly-coordinating base. In addition, I would like to thank Professor Peidong Yang for the use of his scanning electron microscope.

2.6 References and Supplementary Figures and Tables

(1) Li, J.-R.; Kuppler, R. J.; Zhou, H.-C. *Chem. Soc. Rev.* **2009**, *38* (5), 1477.
(2) Li, J.-R.; Sculley, J.; Zhou, H.-C. *Chem. Rev.* **2012**, *112* (2), 869.
(3) Bloch, E. D.; Queen, W. L.; Krishna, R.; Zadrozny, J. M.; Brown, C. M.; Long, J. R. *Science* **2012**, *335* (6076), 1606.
(4) McDonald, T. M.; Mason, J. A.; Kong, X.; Bloch, E. D.; Gygi, D.; Dani, A.; Crocella, V.; Giordanino, F.; Odoh, S. O.; Drisdell, W.; Vlaisavljevich, B.; Dzubak, A. L.; Poloni, R.; Schnell, S. K.; Planas, N.; Lee, K.; Pascal, T.; Wan, L. F.; Prendergast, D.; Neaton, J. B.; Smit, B.; Kortright, J. B.; Gagliardi, L.; Bordiga, S.; Reimer, J. A.; Long, J. R. *Nature* **2015**, *519*, 303.
(5) Lee, J.; Farha, O. K.; Roberts, J.; Scheidt, K. A.; Nguyen, S. T.; Hupp, J. T. *Chem. Soc. Rev.* **2009**, *38* (5), 1450.
(6) Corma, A.; García, H.; Llabrés i Xamena, F. X. *Chem. Rev.* **2010**, *110* (8), 4606.
(7) Horcajada, P.; Serre, C.; Vallet-Regí, M.; Sebban, M.; Taulelle, F.; Férey, G. *Angew. Chemie Int. Ed.* **2006**, *45* (36), 5974.
(8) Horcajada, P.; Chalati, T.; Serre, C.; Gillet, B.; Sebrie, C.; Baati, T.; Eubank, J. F.; Heurtaux, D.; Clayette, P.; Kreuz, C.; Chang, J.S.; Hwang, Y.K.; Marsaud, V.; Bories, P.N.; Cynober, L.; Gil, S.; Férey, G.; Couvreur, P.; Gref, R. *Nat. Mater.* **2010**, *9* (2), 172.
(9) Rosi, N. L.; Eckert, J.; Eddaoudi, M.; Vodak, D. T.; Kim, J.; O'Keeffe, M.; Yaghi, O. M. *Science* **2003**, *300* (5622), 1127.
(10) Suh, M. P.; Park, H. J.; Prasad, T. K.; Lim, D.-W. *Chem. Rev.* **2012**, *112* (2), 782–835.
(11) Murray, L. J.; Dincă, M.; Long, J. R. *Chem. Soc. Rev.* **2009**, *38* (5), 1294.
(12) Mason, J. A.; Oktawiec, J.; Taylor, M. K.; Hudson, M. R.; Rodriguez, J.; Bachman, J. E.; Gonzalez, M. I.; Cervellino, A.; Guagliardi, A.; Brown, C. M.; Llewellyn, P. L.; Masciocchi, N.; Long, J. R. *Nature* **2015**, *527* (7578), 357.
(13) Wang, L.; Han, Y.; Feng, X.; Zhou, J.; Qi, P.; Wang, B. *Coord. Chem. Rev.* **2016**, *307*, 361.
(14) Zhou, H.-C.; Long, J. R.; Yaghi, O. M. *Chem. Rev.* **2012**, *112* (2), 673.
(15) Rezaei, F.; Webley, P. *Chem. Eng. Sci.* **2009**, *64* (24), 5182.
(16) Akhtar, F.; Andersson, L.; Ogunwumi, S.; Hedin, N.; Bergström, L. *J. Eur. Ceram. Soc.* **2014**, *34* (7), 1643.
(17) Chung, T.-S.; Jiang, L. Y.; Li, Y.; Kulprathipanja, S. *Prog. Polym. Sci.* **2007**, *32* (4), 483.
(18) Bachman, J. E.; Smith, Z. P.; Li, T.; Xu, T.; Long, J. R. *Nat. Mater.* **2016**, *15* (8), 845.
(19) Ruthven, D. M. *Principles of Adsorption and Adsorption Processes*; John Wiley and Sons, 1984.
(20) Rousseau, R. W. *Handbook of Separation Process Technology*; John Wiley and Sons, 1987.
(21) Umemura, A.; Diring, S.; Furukawa, S.; Uehara, H.; Tsuruoka, T.; Kitagawa, S. *J. Am. Chem. Soc.* **2011**, *133* (39), 15506.
(22) Hermes, S.; Witte, T.; Hikov, T.; Zacher, D.; Bahnmüller, S.; Langstein, G.; Huber, K.; Fischer, R. A. *J. Am. Chem. Soc.* **2007**, *129* (17), 5324.
(23) Diring, S.; Furukawa, S.; Takashima, Y.; Tsuruoka, T.; Kitagawa, S. *Chem. Mater.* **2010**, *22* (16), 4531.
(24) Cravillon, J.; Nayuk, R.; Springer, S.; Feldhoff, A.; Huber, K.; Wiebcke, M. *Chem. Mater.* **2011**, *23* (8), 2130.

(25) Schaate, A.; Roy, P.; Godt, A.; Lippke, J.; Waltz, F.; Wiebcke, M.; Behrens, P. *Chem. - A Eur. J.* **2011**, *17* (24), 6643.
(26) Stock, N.; Biswas, S. *Chem. Rev.* **2012**, *112* (2), 933.
(27) Rosi, N. L.; Kim, J.; Eddaoudi, M.; Chen, B.; Yaghi, O. M. *J. Am. Chem. Soc.* **2005**, *127*, 1504.
(28) Caskey, S. R.; Wong-Foy, A. G.; Matzger, A. J. *J. Am. Chem. Soc.* **2008**, *130* (33), 10870.
(29) Díaz-García, M.; Sánchez-Sánchez, M. *Microporous Mesoporous Mater.* **2014**, *190*, 248.
(30) Verma, P.; Xu, X.; Truhlar, D. G. *J. Phys. Chem. C* **2013**, *117* (24), 12648.
(31) Lee, K.; Howe, J. D.; Lin, L.-C.; Smit, B.; Neaton, J. B. *Chem. Mater.* **2015**, *27* (3), 668.
(32) Zhao, Y.; Truhlar, D. G. *J. Chem. Phys.* **2006**, *125* (19), 194101.
(33) Frisch, M. J.; Trucks, G. W.; Schlegel, H. B.; Scuseria, G. E.; Robb, M. A.; Cheeseman, J. R.; Scalmani, G.; Barone, V.; Mennucci, B.; Petersson, G. A.; Nakatsuji, H.; Li, X.; Caricato, M.; Marenich, A.; Bloino, J.; Janesko, B. G.; Gomperts, R.; Mennucci, B.; Hratchian, H. P.; Ortiz, J. V.; Izmaylov, A. F.; Sonnenberg, J. L.; Williams-Young, D.; Ding, F.; Lipparini, F.; Egidi, F.; Goings, J.; Peng, B.; Petrone, A.; Henderson, T.; Ranasinghe, D.; Zakrzewski, V. G.; Gao, J.; Rega, N.; Zheng, G.; Liang, W.; Hada, M.; Ehara, M.; Toyota, K.; Fukuda, R.; Hasegawa, J.; Ishida, M.; Nakajima, T.; Honda, Y.; Kitao, O.; Nakai, H.; Vreven, T.; Throssell, K.; Montgomery, Jr., J. A.; Peralta, J. E.; Ogliaro, F.; Bearpark, M.; Heyd, J. J.; Brothers, E.; Kudin, K. N.; Staroverov, V. N.; Keith, T.; Kobayashi, R.; Normand, J.; Raghavachari, K.; Rendell, A.; Burant, J. C.; Iyengar, S. S.; Tomasi, J.; Cossi, M.; Millam, J. M.; Klene, M.; Adamo, C.; Cammi, R.; Ochterski, J. W.; Martin, R. L.; Morokuma, K.; Farkas, O.; Foresman, J. B.; Fox, D. J. Gaussian 09, Revision C.01; Gaussian, Inc.: Wallingford, CT, 2010.
(34) Tang, J.; Yamauchi, Y. *Nat. Chem.* **2016**, *8* (7), 638.
(35) Gonzalez, M. I.; Mason, J. A.; Bloch, E. D.; Teat, S. J.; Gagnon, K. J.; Morrison, G. Y.; Queen, W. L.; Long, J. R. *Chem. Sci.* **2017**, *8*, 4387.
(36) Chmelik, C.; Mundstock, A.; Dietzel, P. D. C.; Caro, J. *Microporous Mesoporous Mater.* **2014**, *183*, 117.
(37) Haque, E.; Jhung, S. H. *Chem. Eng. J.* **2011**, *173* (3), 866.
(38) Yan, W.; Guo, Z.; Xu, H.; Lou, Y.; Chen, J.; Li, Q. *Mater. Chem. Front.* **2017**, *1* (7), 1324.
(39) Chen, J.; Mu, X.; Du, M.; Lou, Y. *Inorg. Chem. Commun.* **2017**, *84*, 241.
(40) Vornholt, S. M.; Henkelis, S. E.; Morris, R. E. *Dalt. Trans.* **2017**, *46*, 8298.
(41) Cattaneo, D.; Warrender, S. J.; Duncan, M. J.; Castledine, R.; Parkinson, N.; Haley, I.; Morris, R. E. *Dalt. Trans.* **2016**, *45* (2), 618.
(42) Bétard, A.; Zacher, D.; Fischer, R. A. *CrystEngComm* **2010**, *12* (11), 3768.
(43) Jiang, H.; Wang, Q.; Wang, H.; Chen, Y.; Zhang, M. *Catal. Commun.* **2016**, *80*, 24.
(44) Forse, A. C.; Gonzalez, M. I.; Siegelman, R. L.; Witherspoon, V. J.; Jawahery, S.; Mercado, R.; Milner, P. J.; Martell, J. D.; Smit, B.; Blümich, B.; Long, J. R.; Reimer, J. A. *J. Am. Chem. Soc.* **2018**, *140*, 1663.
(45) Wulff, G. *Zeitschrift für Kryst. und Mineral.* **1901**, *34*, 449.
(46) Hartman, P.; Perdok, W. G. *Acta Crystallogr.* **1955**, *8* (1), 49.
(47) Friedel, G. *Bull. Soc. Fr. Miner.* **1907**, *30*, 326.
(48) Donnay, J. D. H.; Harker, D. *Am. Miner.* **1937**, *22*, 446.
(49) Macrae, C. F.; Bruno, I. J.; Chisholm, J. A.; Edgington, P. R.; McCabe, P.; Pidcock, E.; Rodriguez-Monge, L.; Taylor, R.; van de Streek, J.; Wood, P. A. *J. Appl. Crystallogr.*

2008, *41* (2), 466.
(50) Friščić, T.; Reid, D. G.; Halasz, I.; Stein, R. S.; Dinnebier, R. E.; Duer, M. J. *Angew. Chemie Int. Ed.* **2010**, *49* (4), 712.
(51) Klimakow, M.; Klobes, P.; Thünemann, A. F.; Rademann, K.; Emmerling, F. *Chem. Mater.* **2010**, *22* (18), 5216.
(52) Tuffnell, J. M.; Ashling, C. W.; Hou, J.; Li, S.; Longley, L.; Ríos Gómez, M. L.; Bennett, T. D. *Chem. Commun.* **2019,** Advance Article.
(53) Buncel, E.; Symons, E. A. *J. Chem. Soc. D* **1970**, *0* (3), 164.
(54) Indeed, as N,N-dimethylformamide decomposition can occur via either thermolysis or hydrolysis, the resulting product is dimethylamine and either carbon monoxide or formate or a mixture thereof, which can change over time in the reaction.
(55) Pohanish, R. P. *Sittig's Handbook of Toxic and Hazardous Chemicals and Carcinogens.*; Elsevier Science, 2011.
(56) It can be helpful to have reactants dissolved for solution-phase studies, as crystals can begin heterogeneous nucleation from precipitated starting matter, for better or for worse: see Chapter 3 for a discussion of nucleation at interfaces.
(57) Mussini, P. R.; Mussini, T.; Rondinini, S. *Pure & Appl. Chem.* **1997**, *69*, 1007.
(58) Rondinini, S. *Anal. Bioanal. Chem.* **2002**, *374* (5), 813.
(59) Rueden, C. T.; Schindelin, J.; Hiner, M. C.; DeZonia, B. E.; Walter, A. E.; Arena, E. T.; Eliceiri, K. W. *BMC Bioinformatics* **2017**, *18* (1), 529.
(60) Murthy, C. R.; Gao, B.; Tao, A. R.; Arya, G. *Nanoscale* **2015**, *7*, 9793.
(61) Zucker, R. V.; Chatain, D.; Dahmen, U.; Hagege, S.; Carter, W. C. *J. Mater.. Sci.* **2012**, *47*, 8290.
(62) Nothing is truly non-coordinating; the consideration here is whether or not the non-coordinating addition appears to interfere with growth, and if the weakly-coordinating species can outcompete the solvent.
(63) Shimizu, S.; Watanabe, N.; Kataoka, T.; Shoji, T.; Abe, N.; Morishita, S.; Ichimura, H. Pyridine and Pyridine Derivatives. In *Ullmann's Encyclopedia of Industrial Chemistry*; Wiley-VCH Verlag GmbH & Co. KGaA: Weinheim, Germany, 2000.
(64) W.M, H. and D. . L. *CRC Handbook of Chemistry and Physics, 91st Edition*; 2010.
(65) Good, N. E.; Winget, G. D.; Winter, W.; Connolly, T. N.; Izawa, S.; Singh, R. M. M. *Biochemistry* **1966**, *5* (2), 467.
(66) Kandegedara, A.; Rorabacher, D. B. *Anal. Chem.* **1999**, *71* (15), 3140.
(67) Barthel, J. M. G.; Krienke, H.; Kunz, W. *Physical Chemistry of Electrolyte Solutions: Modern Aspects*; Steinkopff, Darmstadt, and Springer: New York, 1998.
(68) *Activity Coefficients in Electrolyte Solutions*, 2nd ed.; Pitzer, K. S., Ed.; CRC Press: Boca Raton, FL, 2018.
(69) Kielland, J. *J. Am. Chem. Soc.* **1937**, *59* (9), 1675.
(70) *Prudent Practices in the Laboratory*; National Academies Press: Washington, D.C., 1995.
(71) Lever, A. B. P.; Ogden, D. *J. Chem. Soc. A Inorganic, Phys. Theor.* **1967**, 2041.
(72) Marchetti, F.; Marchetti, F.; Melai, B.; Pampaloni, G.; Zacchini, S. *Inorg. Chem.* **2007**. *46*, 3378.
(73) Lewis, G. N. *Valence and the Structure of Atoms and Molecules*; The Chemical Catalog Company: New York, 1923.
(74) Verhoek, F. H. *J. Am. Chem. Soc.* **1934**, *56* (3), 571.
(75) While Cd_2(dobdc) is an interesting framework (and indeed the only reported second row

metal variant of M_2(dobdc), the toxicity of cadmium makes it a less useful model system.
(76) Irving, H.; Williams, R. J. P. *J. Chem. Soc.* **1953**, 3192.
(77) Attempts to form Cu_2(dobdc) from this solvent system all resulted in amorphous products or nothing at all.

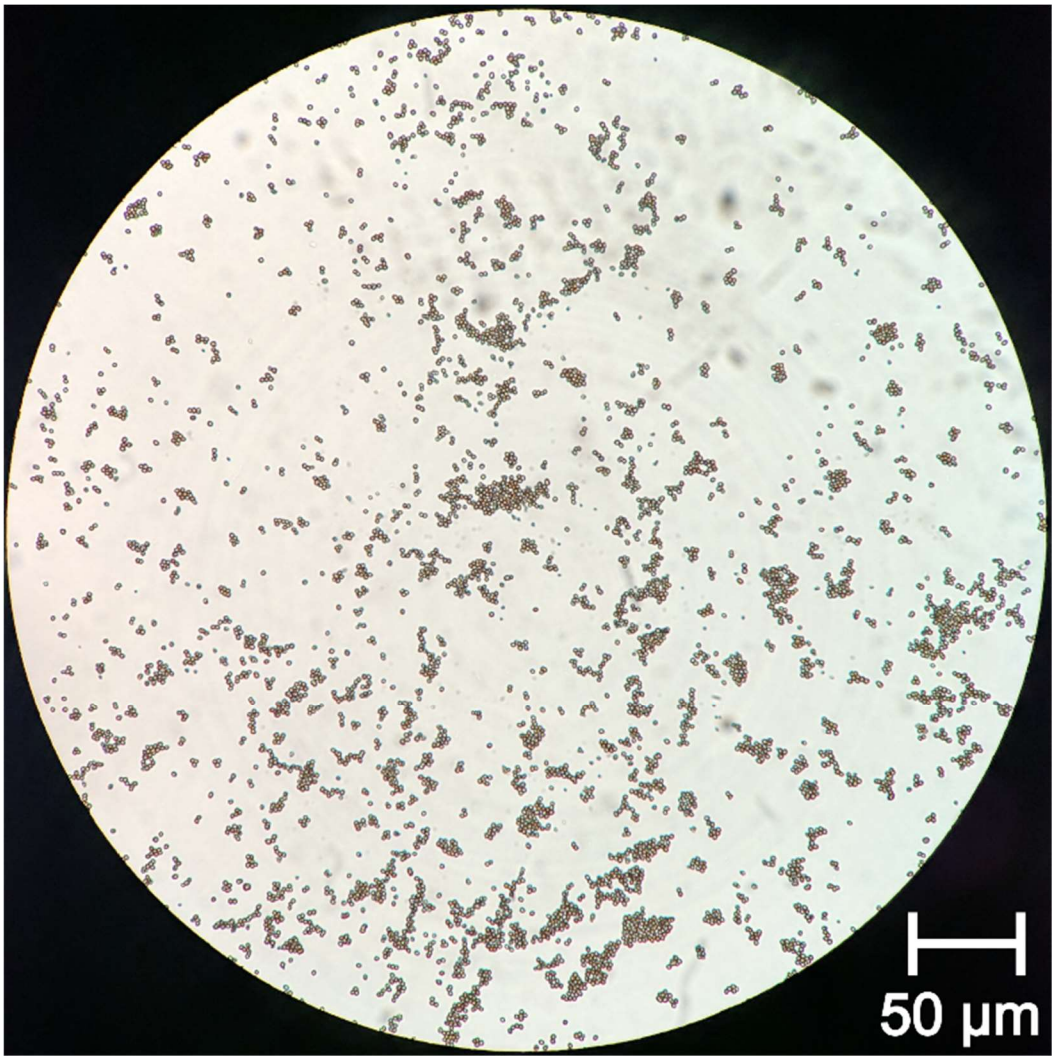

Figure 2.S1. Optical microscopy of monodisperse Co_2(dobdc) generated in aqueous ethanol using cobalt(II) acetate as a metal source.

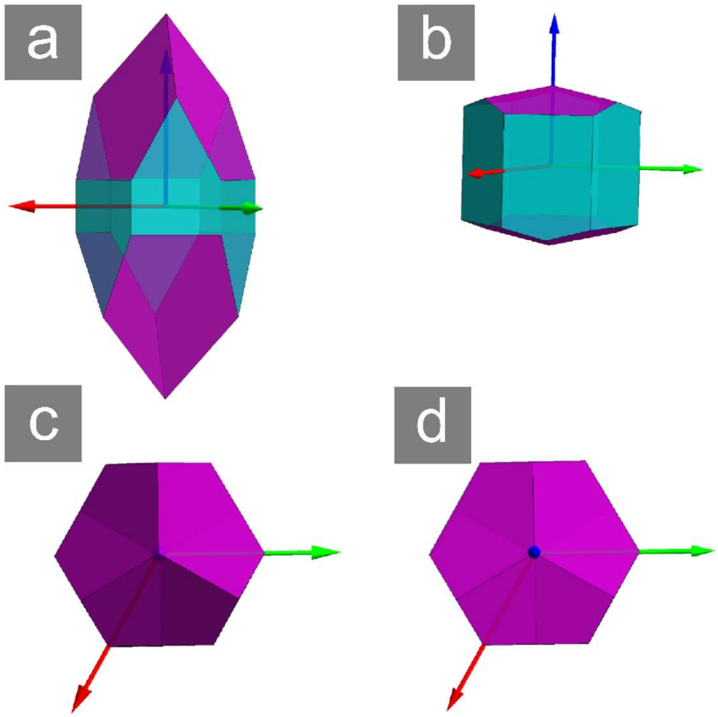

Figure 2.S2. (a) and (b) are two hypothetical morphologies which satisfy the space group symmetry requirements of Co_2(dobdc); (c) is the crystallite in (a) viewed directly down the *c*-axis, and (d) is the crystallite in (b) viewed directly down the *c*-axis.

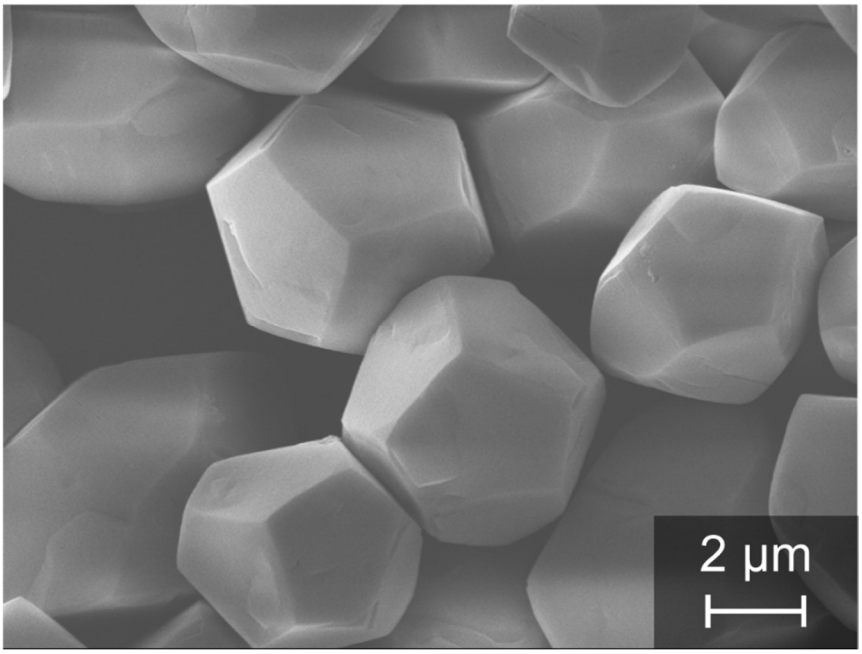

Figure 2.S3. Several examples of crystallites viewed down the *c*-axis (per Fig. 2.S2c-d) are featured in the center of this SEM micrograph.

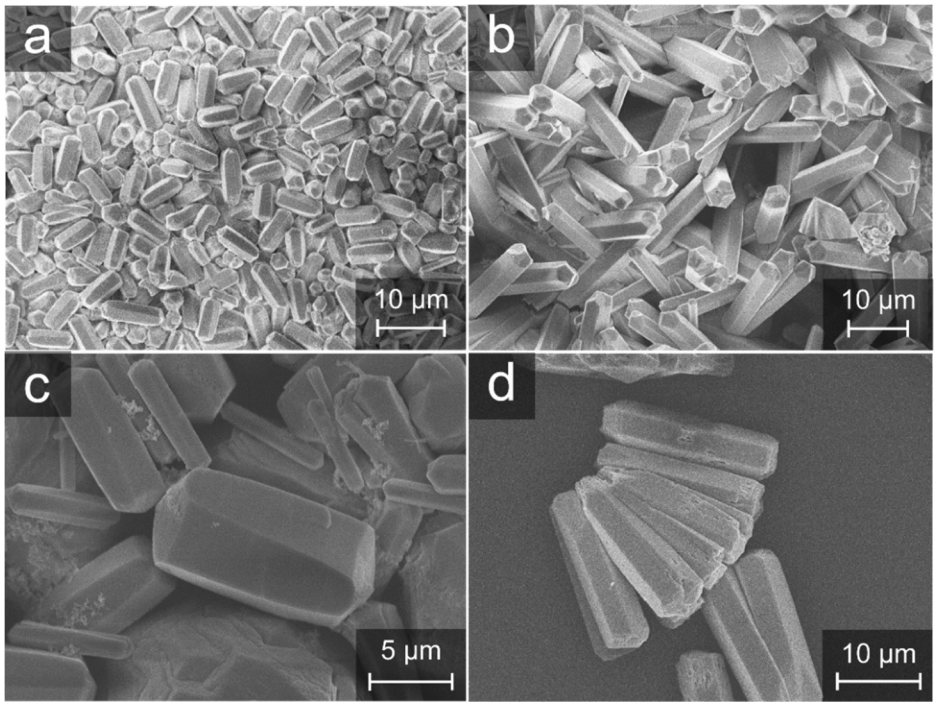

Figure 2.S4. Co_2(dobdc) crystallites synthesized at pH 7 using MOPS buffer and (a) cobalt(II) triflate, (b) cobalt(II) sulfate, (c) cobalt(II) bromide, and (d) cobalt(II) iodide.

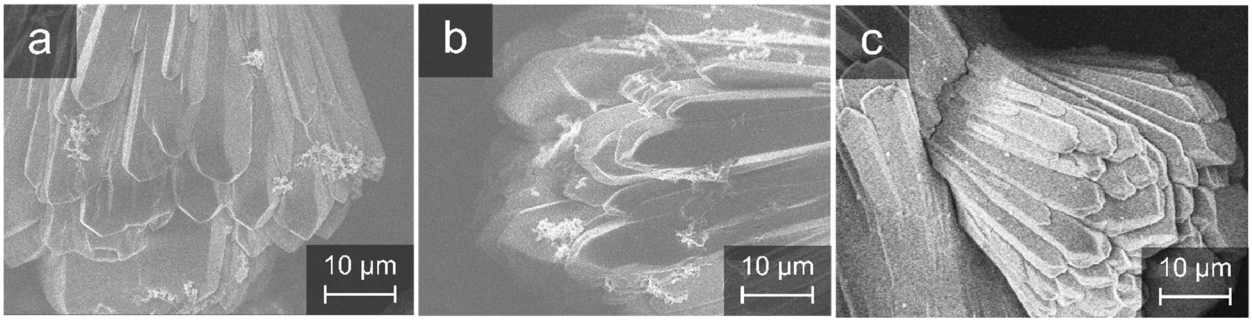

Figure 2.S5. Buffered synthesis of Co_2(dobdc) at different pH values using cobalt(II) tetrafluoroborate: (a) pH 5 (b) pH 6 (c) pH 7. Without acetate present, there is no noticeable variation in morphology across this pH range.

Table 2.S1. pK_a values of conjugate acids for anions used in buffered synthesis.

Acid	pK_a (25 °C, water)
Acetic	4.76
Formic	3.75
Chloroacetic	2.87
Trichloroacetic	0.66

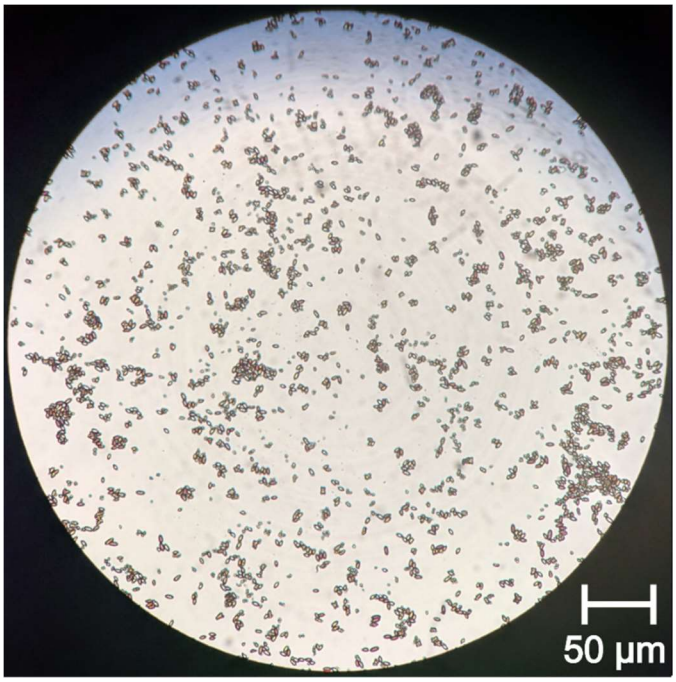

Figure 2.S6. Optical microscopy of Co_2(dobdc) crystallites synthesized at pH 7 using cobalt(II) formate.

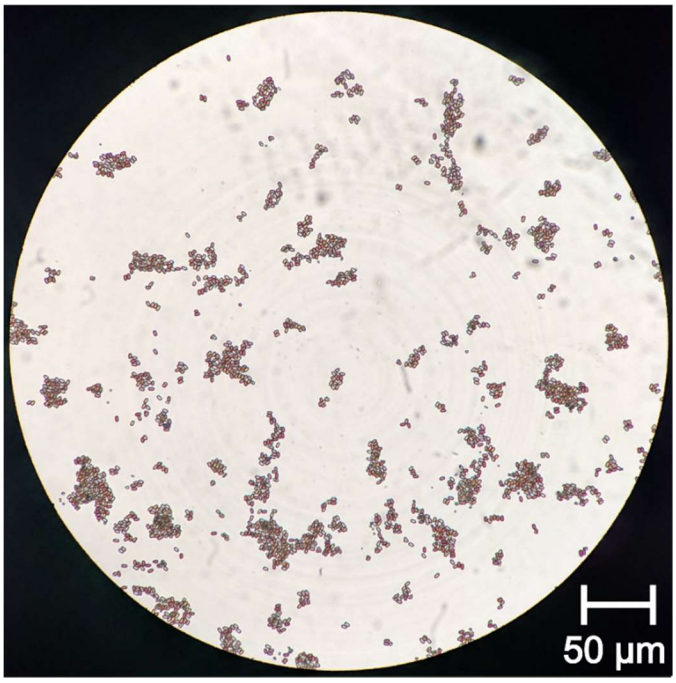

Figure 2.S7. Optical microscopy of Co2(dobdc) crystallites synthesized at pH 7 using cobalt(II) chloroacetate.

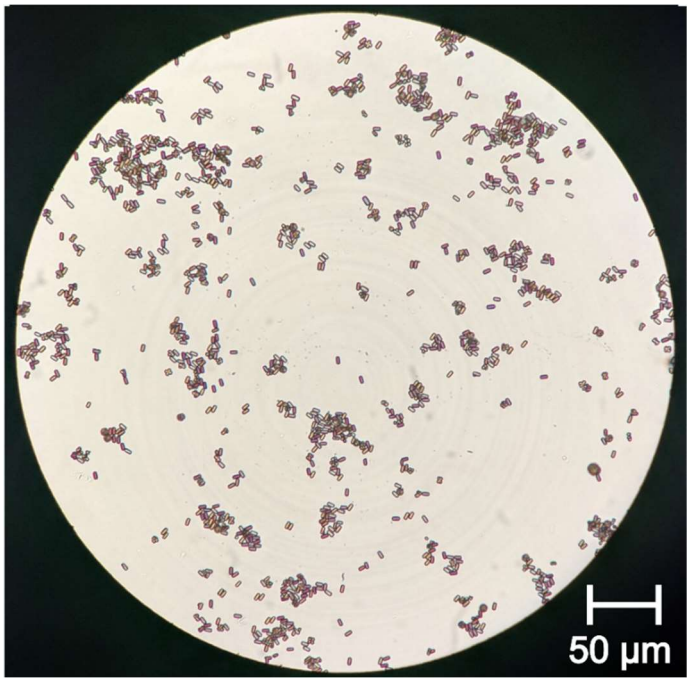

Figure 2.S8. Optical microscopy of Co2(dobdc) crystallites synthesized at pH 7 using cobalt(II) trichloroacetate.

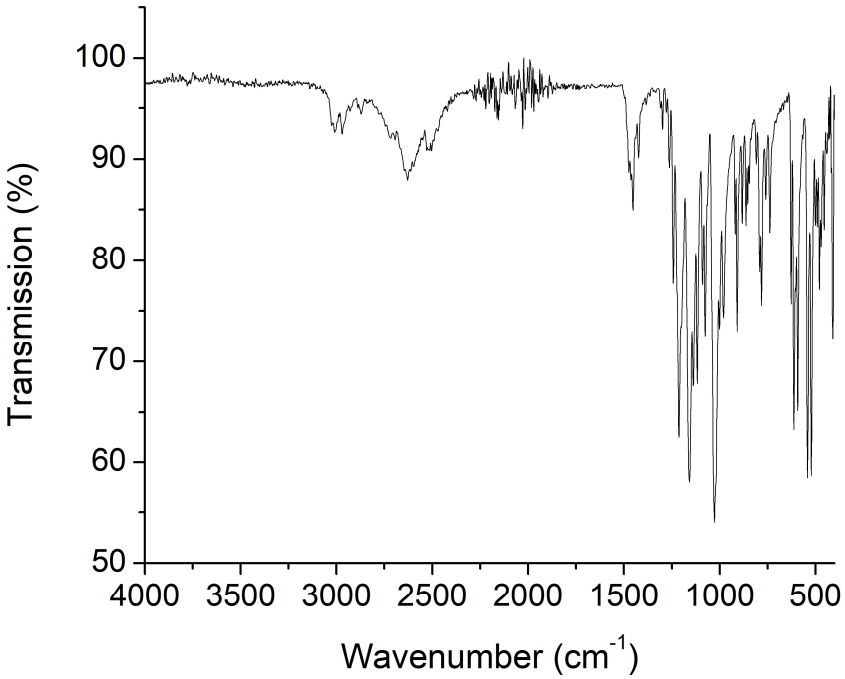

Figure 2.S9. The infrared spectroscopy pattern of the buffer, 3-(N-morpholino)propanesulfonic acid, has many identifying features. The sharpest of these is near 1026 cm^{-1} and is in a region where the framework Co_2(dobdc) has no stretching frequencies (Fig. 2.S10).

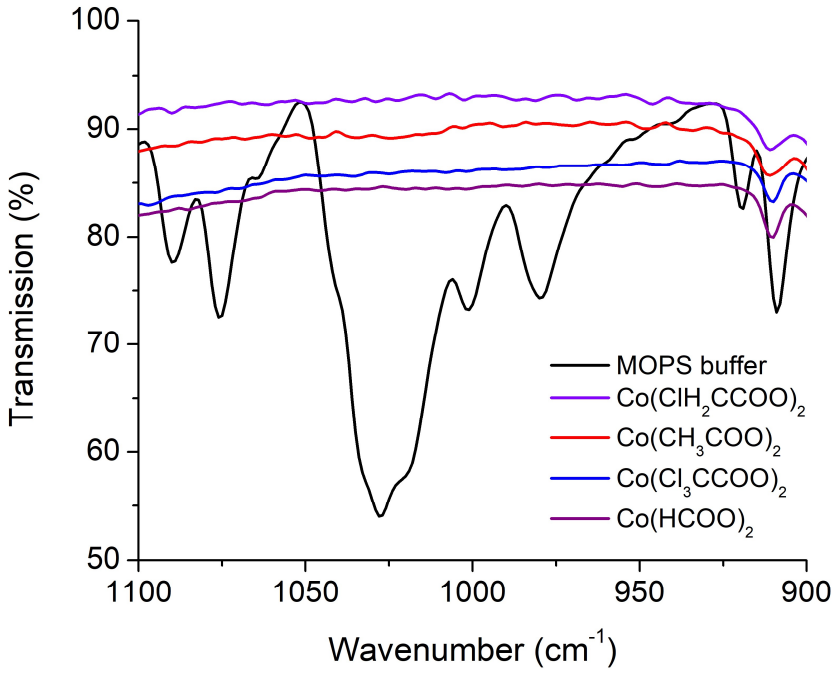

Figure 2.S10. Focusing on the region incorporating an identifying sulfonic acid stretch at 1026 cm^{-1} in the buffer, there is no evidence of buffer incorporation into any Co_2(dobdc) product formed in buffer, identified in the legend using the precursor metal salt.

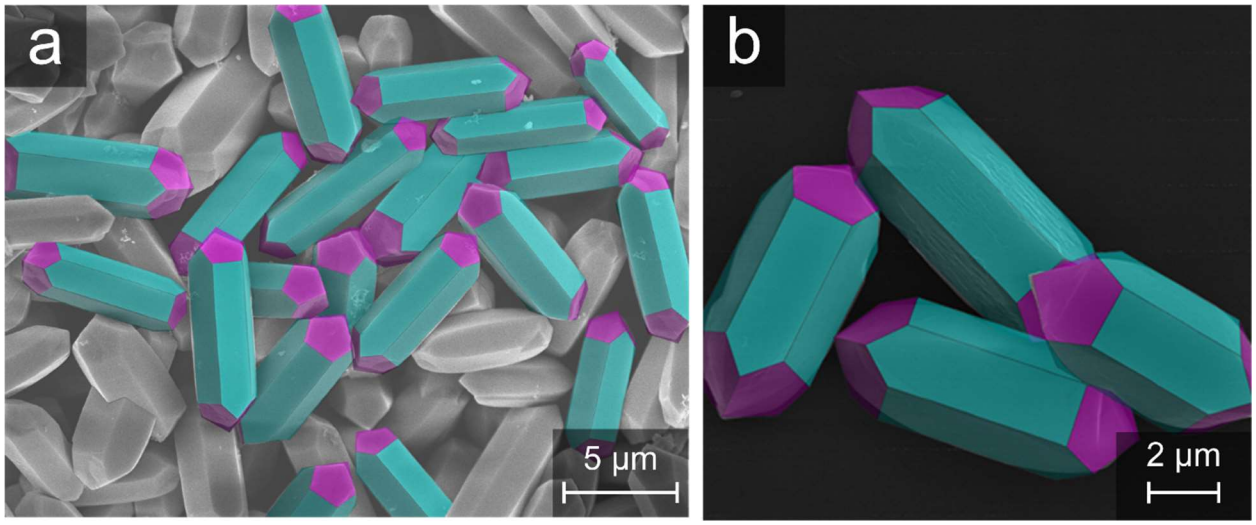

Figure 2.S11. Indexed particles synthesized at pH 7 using (a) cobalt(II) chloroacetate and (b) cobalt(II) formate. Notably, the facets may be self-consistently indexed to be the same as those resulting from the cobalt(II) acetate synthesis.

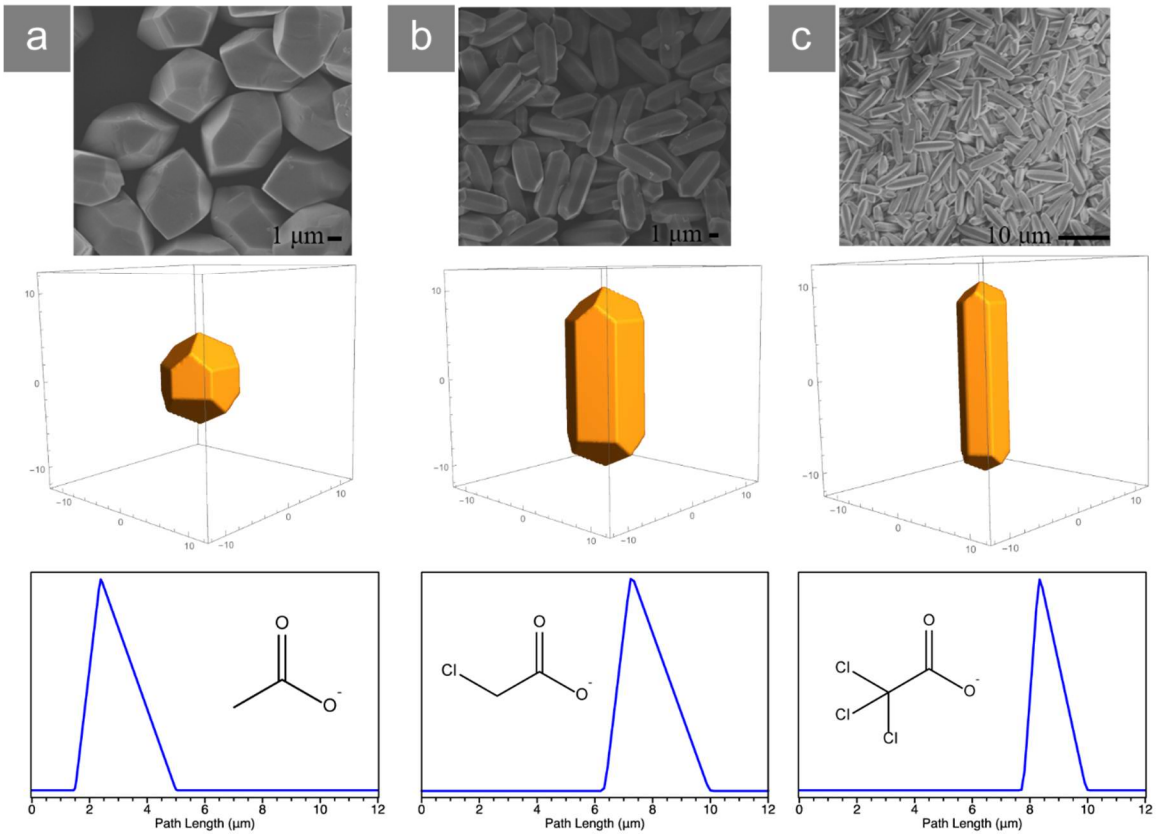

Figure 2.S12. Path length distributions for Co_2(dobdc) crystallites synthesized at pH 7 using (a) cobalt(II) acetate (b) cobalt(II) chloroacetate (c) cobalt(II) trichloroacetate. Distributions are generated using the morphologies reconstructed in Mathematica from SEM micrographs.

Chapter 3: Controlling Interfacial Effects During Crystallization

3.1 Introduction

Crystalline phase and distribution of crystallite shape and size are products of the crystallization conditions. It can be extraordinarily difficult to understand and predict the conditions needed for a given desired phase, size, or shape, as there are a vast number of different programmed (i.e., heating rate or method) and synthetic variables available. As discussed in Chapter 2, many of these variables are intertwined; changing a programmatic variable or adding some molecule to modify one variable can bring about wholly unexpected results. Most metal–organic framework studies on crystallization rely on changing one programmatic variable at a time, such as solvent or solvent combination,[1–5] metal source,[6–11] or temperature,[7,12–14] among others.[15] Notably, these are all handles assumed to affect solution variables. As the frameworks in hydrothermal or solvothermal synthesis are grown from solution, it generally assumed that these solution variables alone dictate product phase or crystallite size or shape.[15] However, nucleation generally occurs heterogeneously, or from surfaces, due to lower interfacial energy, which is not one of the typically-studied solution variables.[16,17] In fact, industrial crystallizers typically rely on seed crystallites or the addition of foreign particles to control heterogeneous nucleation and achieve desired product outcomes.[18] Although the surfaces and interfaces present during typical solvothermal or hydrothermal synthesis of metal–organic frameworks are generally disregarded, it is possible that metal–organic frameworks are nucleating through heterogeneous pathways.

A growing field in metal–organic framework syntheses involves intentionally growing materials on surfaces. This subgroup of materials is referred to as surface-mounted metal–organic frameworks, or SURMOFs.[19–25] These are materials intended to nucleate on and remain attached to a surface, whereas hydrothermal or solvothermal syntheses usually collect precipitated crystallites. Usually, the process of growing SURMOFs involves layer-by-layer techniques, where the solution is changed from one containing the metal ion, to one containing the ligand, and so on. While using a surface-growth technique has been done to achieve specific crystal facet orientations relative to the surface, it has not been employed for phase selection. The closest example of phase selection based on a surface functionality is Grzesiak and coworkers' work with MOF-2 and MOF-5 derivatives: in this case, by adding a polymer substrate, they were able to induce two new phases.[26] Although metal–organic framework materials can be grown on surfaces, it is by no means established that the surface-liquid interface is an important variable during hydrothermal or solvothermal synthesis. Herein, I demonstrate that surface functionalities present on the glassware are an important variable during metal–organic framework synthesis across different metal analogues and frameworks. Further, control of surface functionalities through passivation can be used to dictate crystalline phase produced, change resulting crystallite size across orders of magnitude, and reduce particle polydispersity.

3.2 Experimental

General Procedures, Materials, and Reagents. Laboratory powder X-ray diffraction patterns were collected using a Bruker AXS D8 Advance diffractometer with Cu Kα radiation (λ = 1.5418

Å). All synthetic manipulations were carried out under air, unless otherwise noted. All water used came from a milli-Q water purification system. All other reagents and solvents were obtained from commercial suppliers at reagent grade purity or higher and were used without further purification. The ligand H_4dobdc was purchased from Sigma-Aldrich. SEM images were taken using a JEOL JSM - 6340F SEM. All samples were prepared by drop-casting particles dispersed in methanol onto a silicon chip, then sputter coating a layer of gold approximately 3 nm thick to reduce sample charging. Crystals were imaged at 5 keV/12 μA.

Chlorotrimethylsilane Surface Passivation. Glassware was heated to 160 °C in an oven for several hours, along with a separate glass jar. With the glassware still hot, a solution of 1% chlorotrimethylsilane in toluene by volume was made in the glass jar and then added to the synthesis glassware. The reaction vessel containing the silane solution was then agitated using a Vortex-Genie 2 Lab Mixer for thirty seconds and allowed to sit for 12 hours. The vessel was then rinsed twice with acetone and heated in a 160 °C oven to remove trace acetone.

N,O-bis(trimethylsilyl)acetamide Surface Passivation. The glassware was heated to 160 °C in an oven for several hours. Two milliliters of neat N,O-bis(trimethylsilyl)acetamide per hundred milliliter of reaction vessel volume were added. The glassware was stoppered via rubber septum or suitable chemically resistant vial lid and the vessel was heated to 120 °C for two hours, at which point it was removed from heat and allowed to cool. The vessel was then rinsed twice with acetone and allowed to dry in an oven at 160 °C.

Reaction 3.1: Coordinating Synthesis of M_2(dobdc), M = Co, Zn. The ligand H_4dobdc (10.0 mg, 0.050 mmol) was dissolved in 5 mL ethanol using sonication and cobalt(II) acetate tetrahydrate (44.0 mg, 0.177 mmol) or zinc acetate dihydrate (39.0 mg, 0.177 mmol) was dissolved in 5 mL H_2O using sonication. The two solutions were combined into a 20 mL vial and agitated for a few seconds using a Vortex-Genie 2 Lab Mixer. The vial was then sealed and suspended into an oil bath already set to 75 °C unless otherwise noted. After at least two hours, the vial was removed from heat and allowed to cool, after which the supernatant solution was decanted. The crystals were soaked three times in 20 mL of water for six hours at 80 °C, followed by soaking three times in 20 mL of N,N-dimethylformamide (DMF) at 120 °C for six hours, followed by soaking three times in 20 mL of methanol at 60 °C for six hours. After each wash, the solution was decanted and replaced. Fully desolvated Co_2(dobdc) crystallites were obtained by heating at 180 °C under dynamic vacuum for 24 h.

Reaction 3.2: 2,6-Lutidine Synthesis of Zn_2(dobdc). The ligand H_4dobdc (10.0 mg, 0.050 mmol) was dissolved in 5 mL ethanol using sonication and zinc(II) nitrate hexahydrate (52.6 mg, 0.177 mmol) was dissolved in 5 mL H_2O using sonication. The two solutions were combined into a 20 mL vial and 2,6-Lutidine (40.9 μL, 0.353 mmol) was added to the solution mixture, which was then agitated for a few seconds using a Vortex-Genie 2 Lab Mixer. The vial was then sealed and suspended into an oil bath already set to 75 °C. After at least two hours, the vial was removed from heat and allowed to cool, after which the supernatant solution was decanted. The crystals were soaked three times in 20 mL of water for six hours at 80 °C, followed by soaking three times in 20 mL of N,N-dimethylformamide (DMF) at 120 °C for six hours, followed by soaking three times in 20 mL of methanol at 60 °C for six hours. After each wash, the solution is decanted and replaced. Fully desolvated Zn_2(dobdc) crystallites were obtained by heating at 180 °C under dynamic vacuum for 24 h.

Reaction 3.3: Synthesis of Zn_2(dobpdc). The ligand H_4dobpdc (14 mg, 0.050 mmol) was dissolved in 5 mL ethanol using sonication and zinc acetate dihydrate (39.0 mg, 0.177 mmol) was dissolved in 5 mL H_2O using sonication.. The two solutions were combined into a 20 mL vial and

agitated for a few seconds using a Vortex-Genie 2 Lab Mixer. The reaction solution was then sparged with nitrogen for twenty minutes. The vial was then sealed and suspended into an oil bath already set to 75 °C unless otherwise noted. After at least two hours, the vial was removed from heat and allowed to cool, after which the supernatant solution was decanted under inert atmosphere. The crystals were soaked three times in 20 mL of water for six hours at 80 °C, followed by soaking three times in 20 mL of N,N-dimethylformamide (DMF) at 120 °C for six hours, followed by soaking three times in 20 mL of methanol at 60 °C for six hours. After each wash, the solution was decanted and replaced. Fully desolvated Zn_2(dobpdc) crystallites were obtained by heating at 180 °C under dynamic vacuum for 24 h.

Intentional Surface Growth. For Co_2(dobdc), Ni_2(dobdc), and Zn_2(dobdc), growth solutions were prepared as described above in aqueous ethanol metal acetate synthesis. For the Mg_2(dobdc) synthesis solution, the ligand H_4dobdc (10.0 mg, 0.050 mmol) was dissolved in 5 mL ethanol using sonication and magnesium(II) acetate tetrahydrate (37.9 mg, 0.177 mmol) was dissolved in 5 mL H_2O using sonication, in analogy to Reaction 3.1. The two solutions were combined into a 20 mL vial and agitated for a few seconds using a Vortex-Genie 2 Lab Mixer. The desired surface for growth was then epoxied to the bottom of a 4 mL vial, which was suspended into the growth solution. At the desired stopping point, the surface was removed and placed into a solution of 1:1 water:ethanol.

Atomic Force Microscopy Measurements. Atomic Force Microscopy images were taken using an Asylum MFP-3D, always in tapping mode and in air, using a series of silicon nitride cantilevers. Samples were left to dry in air after quenching in water/ethanol.

3.3 Results and Discussion

As detailed in Chapter 2, the aqueous ethanol synthesis of Co_2(dobdc) leads to highly monodisperse crystallites of designable aspect ratio. However, the inspiration for the work in this chapter inspecting and controlling solid/liquid interfaces during synthesis arose from irreproducibilities observed while scaling up these syntheses for use in diffusional studies.

Variation in Co_2(dobdc) Synthesis. In attempting to test the properties of the small-aspect ratio Co_2(dobdc) crystallites reported in Chapter 2, the synthesis (Reaction 3.1) needed to be replicated and scaled up. Follow-up experiments with seemingly identical solutions did not yield identical batches of crystallites. Thus, there was an uncontrolled reaction handle causing variation in dispersity that was not arising merely from the solution itself. One plausible variable was that of the heating set-up and method. Early syntheses were run in a natural convection oven which had already been set to 75 °C. Both non-ideal location of a given vial within the oven and the total number of vials present in the oven at any one time contributed to increased particle dispersity, which suggest non-uniform heat transfer within the oven. Indeed, this is a known effect for zeolite synthesis, where temperature gradients contribute to particle dispersity.[27,28]

As nucleation and growth have activation barriers and are temperature-dependent,[29,30] thermal gradients during synthesis lead to spatially non-uniform crystallization conditions within the same reaction vessel. After testing a number of different heating media (oven, oil bath, metal bead bath) and different methods of introducing the samples to an increased temperature (ramping temperature slowly, ramping temperature quickly, and placing directly in a pre-heated medium), I found that a preheated oil bath generally led to the lowest morphological variation within a single sample and from sample to sample (Fig. 3.1). Similar conclusions have been found for zeolite

systems.[31] While heating method has been found to be important for metal–organic framework synthesis, it is normally discussed in the context of microwave heating.[32,33]

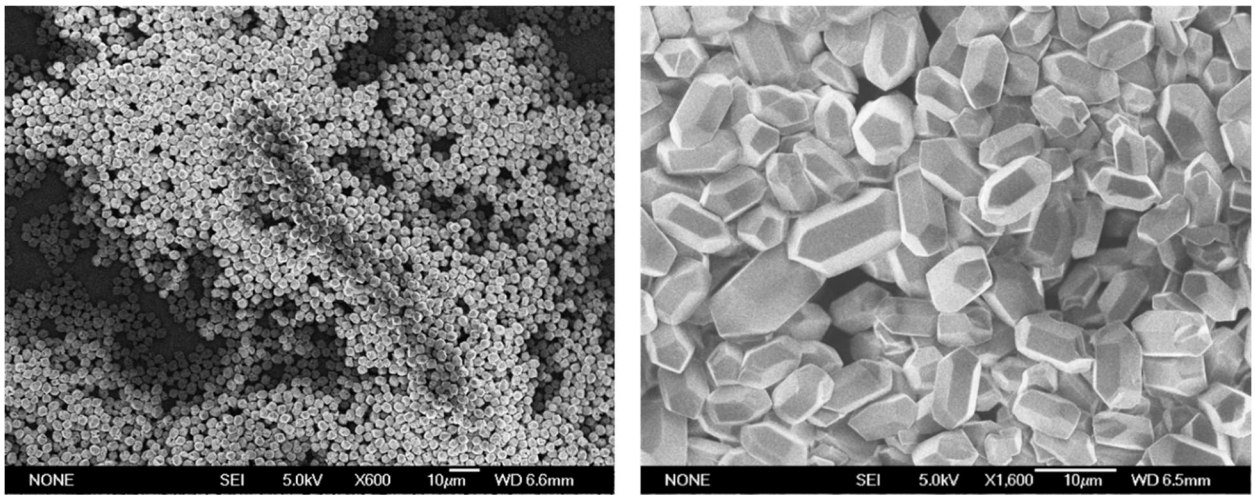

Figure 3.1. At left, Reaction 1-Co_2(dobdc) formed in an oil bath; at right, Reaction 1-Co_2(dobdc) synthesized in an oven. The sample synthesized in an oil bath has slightly smaller, highly uniform particles. The sample synthesized in an oven displays the same crystalline facets but has a moderate degree of polydispersity.

Under circumstances of particularly low temperature or directional heating, however, it appeared that some or all Co_2(dobdc) crystallites may be forming from the sides of the glassware. This was in some cases visually apparent, as a thin film would be present post-synthesis on some vials across any of the heating sources. The crystallites could also be coaxed into forming from the glassware by controlling the direction and duration of heating. Reaction 3.1 for the cobalt analogue was allowed to react at raised temperature for only a short amount of time (1 minute) by sitting on a hot plate set to 75 °C, where a thermal gradient was introduced by only heating one side of the glassware. The vials were then left to sit for two weeks at room temperature. The hypothesis was that this would have some nucleation during the short period of heating and allow growth at a reduced temperature, leading to particularly large crystallites. Instead, the synthesis formed several film sections of Co_2(dobdc), confirmed via powder X-ray diffraction (Fig. 3.S1), consisting of many small needle morphologies arranged in parallel with preferential orientation to form a rug-like sheet (Fig. 3.2). The sheets are free-standing.

Although individual domains are less than a micron in length, the sheets themselves are several hundred microns in width and length. Such macrostructures with preferential domain arrangement are rare; in fact, this hierarchical morphology is not only rare but unprecedented among reported MOF morphologies for one-dimensional frameworks. While thin films exist, they do not exhibit parallel preferred orientation.[34–36] No mechanistic studies were performed on the formation of this morphology, but the particular dimensionality of the morphology (a two-dimensional sheet consisting of small rods) resembles the dimensional constraint imposed during synthesis. In fact, using the two-dimensional interface between immiscible liquid layers is a common strategy to grow metal–organic framework thin films.[25,37,38] It seemed likely from these preliminary pieces of evidence that the surface-liquid interface was playing an important role during this synthesis.

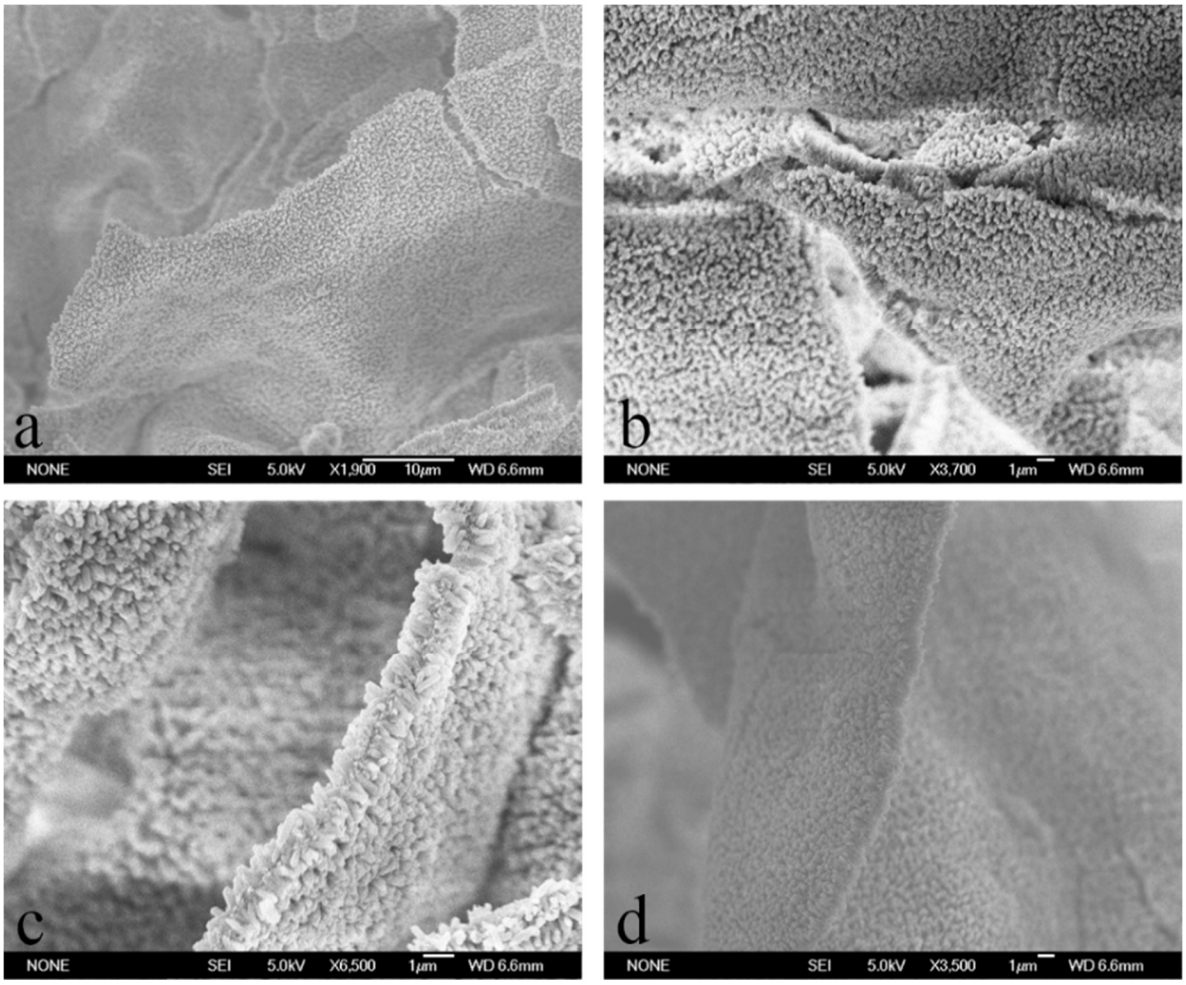

Figure 3.2. The sheet-grown Co_2(dobdc) structure demonstrated in (a)-(d) was found to be part of many different sheets, hundreds of square microns in size. The cross-sections shown in (c) and (d), about a micron in thickness, are representative of the entire sample.

In synthetic chemistry, it has been known for decades that surface silanol groups on glassware can interfere with desired chemical reactions.[39] Adsorption of metal ions on hydrated solid surfaces in general is frequently encountered in both natural aquatic environments and in industrial processes.[40–42] The native silanol groups present in amorphous silicon oxide can be highly adsorptive to metal cations, including the metals which can be incorporated into M_2(dobdc).[43] These silanol groups can behave as protic acids in contact with water and as Lewis bases towards incoming Lewis acids. Indeed, numerous studies have been conducted on the adsorption behavior of cobalt(II) at various oxide surfaces, including a suite on silica itself.[44–46] While a full discussion of the mechanism, structure, and complexes formed is beyond the scope of this chapter, there is a general literature consensus that the nature of the adsorption is ionic and that in all observed cases cobalt(II) ions maintain an octahedral coordination geometry.[46] It was plausible that cobalt(II) adsorption takes place at native silanol groups during hydrothermal synthesis. This leads to the possibility of heterogeneous nucleation at these cobalt-adsorbed sites, exacerbated by the fact that in any heating configuration discussed above, the thermal gradient is highest at the glassware

surface. That is, the surfaces heat up faster than the bulk solution, as they are in direct contact with the heat transfer medium.

One way of probing the proposed influence of the silanol groups on the reaction products is to passivate the surface. This process involves treating the glassware with a covalent coating method to chemically graft desired functionalities in the place of the original hydroxyl groups.[47] In this case, adding capping hydrocarbon groups (such as -Si(CH_3)$_3$) to the exposed silanol site should prevent cobalt(II) adsorption at these sites and related reaction interference. An easy test of the success of the method is visual inspection of the contact angle after adding water to the glassware. Covered in hydrophobic groups, the contact angle between the surface and the water changes from low angles, indicating surface wetting, to angles greater than 90°, indicating bad adhesion between the water and the surface. As a control test, I re-ran the aqueous ethanol Co_2(dobdc) synthesis with and without silanized glassware. Remarkably, the size and shape dispersity improved both within each sample and between samples using silanized glassware. In fact, heating method plays a significantly reduced role with passivated reaction vessel surfaces: after re-running the synthesis in an oil bath and in an oven, the difference between the oven and the oil samples vanished, and both samples are particularly monodisperse in size and morphology (Fig. 3.3). Removing the influence of surface silanol groups is thus an important variable in improving homogeneity and reproducibility of Co_2(dobdc) synthesis and could be crucial in the process of scaling up syntheses to industrial usage.

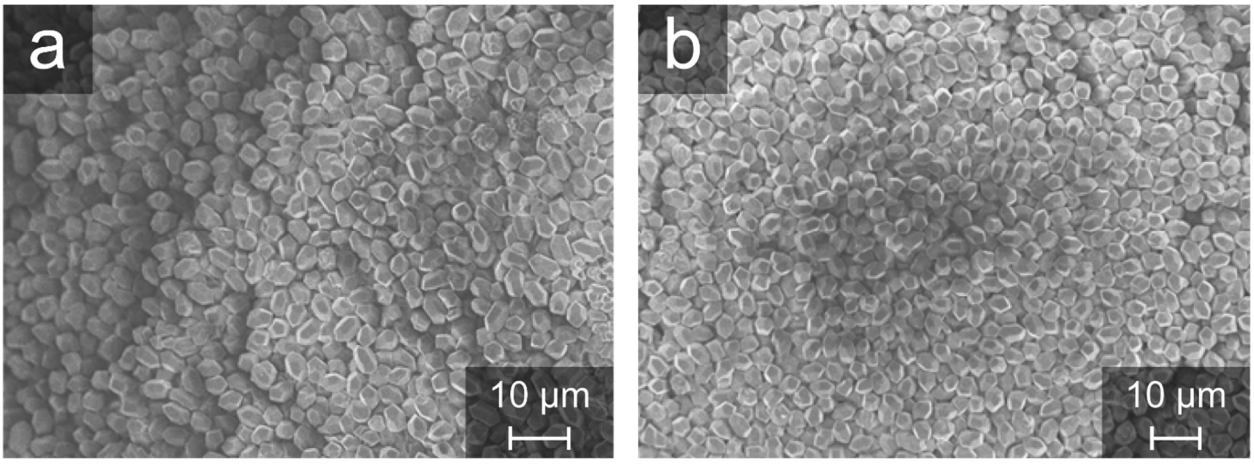

Figure 3.3. (a) Reaction 3.1 to produce Co_2(dobdc), synthesized in oil with silanized glassware versus (b) the same stock solution synthesized in silanized vials in an oven. Remarkably, the differences observed using heating method vanish after the glassware surfaces have been passivated.

Phase Selection in Zn_2(dobdc) Synthesis. The interference of surface sites during hydrothermal synthesis seemed plausible for the other metal analogues of M_2(dobdc), including the zinc analogue. In the process of synthesizing large quantities of large Zn_2(dobdc) for the studies in Chapter 5 via repetition of Reaction 3.2, I found that reproducing the synthesis did not always lead to the same results in size, shape, or even crystalline phase produced. While previous synthetic trials had produced long needles several hundred microns in length (Fig. 2.13), many replicated trials sometimes led to the expected very large crystallites of Zn_2(dobdc) and sometimes instead to a highly crystalline secondary phase reported in the literature[48] to be infinite one-dimensional

chains of tetrahedral zinc(II) bridged by the doubly-deprotonated ligand, $Zn(H_2dobdc)•2H_2O$. The morphology is also characteristically different between the two phases: $Zn_2(dobdc)$ forms long rods under these conditions, as mentioned in Chapter 2, and the second phase makes a block-like morphology. Notably, this inconsistency arose when using identical solution and programmatic variables, such as reactant and solvent source or heating method. Attempts to filter the solutions made no difference, down to 0.22 micron-sized PTFE filters. Different results were obtained on a vial-by-vial basis from stock solutions, which made it clear that the controlling handle must not be a solution variable at all, but rather variation in the borosilicate glassware vials.

Using Reaction 3.2 without silanized glassware, stock solutions led to the $Zn_2(dobdc)$ structure for 24 out of 50 trials. After passivating vials using trimethylchlorosilane (see Section 3.2), all vials formed majority $Zn_2(dobdc)$ type material via powder X-ray diffraction and optical microscopy, and 38/40 vials formed only $Zn_2(dobdc)$ (Fig. 3.4). The other two vials also formed some $Zn(H_2dobdc)•2H_2O$. This is a significant improvement over the prior outcome, where approximately half of the vials failed to form the desired phase. Generally, phase selection is explained by rationalizing the differences between the materials formed in terms of solution variables and final phase stability.[49–57] For example, higher temperatures can lead to thermodynamic instead of kinetic products.[58] In general, variation in the solution pH can lead to products with Brønsted acidic or basic functionalities at a corresponding protonation state and corresponding conformations.[59,60]

At first, when presented with the question of phase selection between $Zn_2(dobdc)$ and $Zn(H_2dobdc)•2H_2O$, it is similarly tempting to try to rationalize when one should appear versus the other. Notably, in the metal–organic framework, the ligand is fully deprotonated $[dobdc]^{4-}$, while in the one-dimensional chain, the ligand is only doubly deprotonated $[H_2dobdc]^{2-}$: the phenolic groups are protonated while the carboxylate groups are not. It could be reasonably expected that the solution pH could play an important role here, where under more acidic conditions, the 1-D phase could be favored relative to $Zn_2(dobdc)$. However, varying the amount of 2,6-Lutidine between 2–7 equivalents added per ligand made no difference in the phase selection when the reaction was run in unsilanized vials. Duplicating this in silanized vials, however, the phase selection is indeed pH-dependent in the manner rationalized above. Vials run with 2–4 equivalents of base per ligand made large crystals of the 1-D chain, confirmed via single crystal X-ray diffraction (Fig. 3.5), while vials run with higher equivalencies and thus higher pH formed majority $Zn_2(dobdc)$. In fact, the crystals formed of the 1-D phase are the first single crystals of the material that allowed for the structure to be solved via single crystal X-ray diffraction.

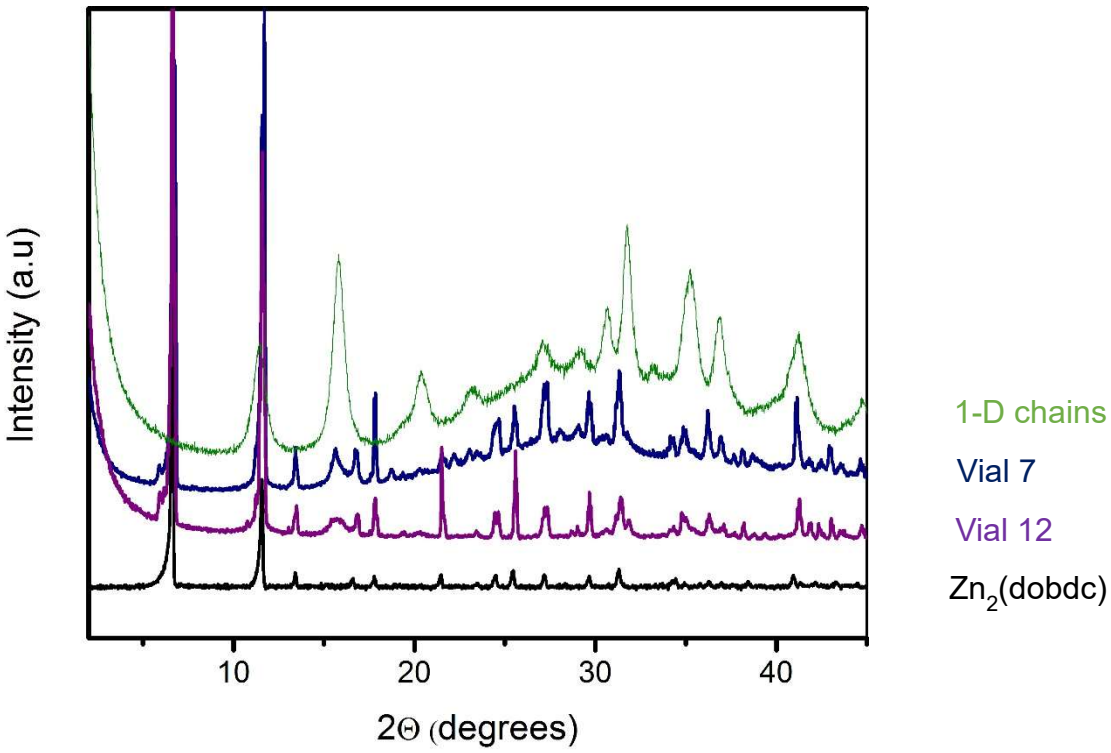

Figure 3.4. Powder X-ray diffraction reveals that all trials of Reaction 3.2 synthesized in silanized vials evidenced significant Zn_2(dobdc) formation; the two vials (out of forty) which also contained some 1-D phase are also displayed here.

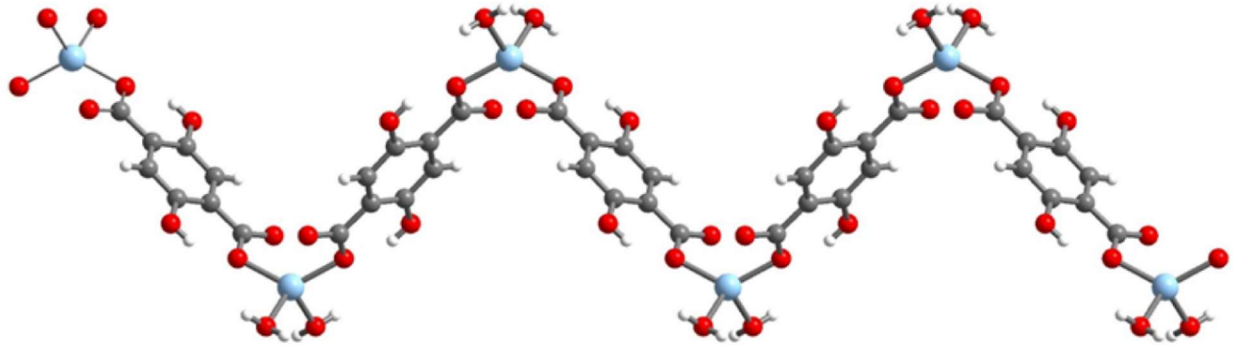

Figure 3.5. The single crystal structure of the one-dimensional phase formed with 3 eq. 2,6-lutidine substituted into Reaction 3.2.

One other difference between the phases is the coordination geometry of the zinc cations. In the 1-D infinite chains, zinc(II) adopts a tetrahedral geometry, with two sites occupied by water and the others coordinated to the ligand through the deprotonated carboxylate group; in the solvated framework, the zinc(II) cations are instead in an octahedral environment, with one site occupied by water. As a cation dissolved in water, zinc(II) exists exclusively as the octahedral hexaaquo species.[61] However, its behavior at surfaces is more complicated. As Roberts et al. discuss in their study of zinc complexation at metal oxide surfaces, the coordination at the surface site for amorphous silica can vary between octahedral and tetrahedral geometry: at low

concentrations and pH, surface zinc species are octahedral, but as pH and surface concentration increases, the geometry changes to tetrahedral coordination.[62] Thus, in unsilanized glassware, having a higher pH could actually lead to surface-bound zinc species having tetrahedral geometry and thus nucleating the 1-D chain at these zinc-adsorbed sites.

Once the silanol groups are passivated, the solution variables control nucleation and growth, and the solution pH-behavior matches the protonation state of the materials formed. Of note, even at 7 equivalents of 2,6-Lutidine per ligand, two of the vials still formed some 1-D chain in the silanized vials, as displayed in Figure 3.4. This could be the true statistical distribution of the products that should be formed from this reaction, but the fact that the material is isolated to specific vials suggests that some 1-D material was formed because of defects in the silanization of the glassware, where remaining silanol groups existed to nucleate the 1-D phase. Using a silanizing reagent such as trimethylchlorosilane can leave point defects, because it is unable to polymerize across the glass surface, each reactant only possessing only one reactive functional group.

Surface-Controlled Crystallite Size in Zn_2(dobpdc) Synthesis. The larger-pore framework M_2(dobpdc) (M = Mg, Mn, Fe, Co, Ni, Zn; dobpdc^{4-} = 4,4'-dioxidobiphenyl-3,3'-dicarboxylate) is of significant interest for carbon capture applications.[63–65] The material is isoreticular to M_2(dobdc), consisting of hexagonal, one-dimensional channels lined with coordinatively-unsaturated metal sites (Fig. 3.6). The pore diameter of M_2(dobpdc) is significantly larger relative to M_2(dobdc), 1.8 nanometers vs. 1.2 nanometers, as a result of the additional phenyl ring on the ligand. It therefore makes a useful extension of the developed syntheses for both practical and fundamental reasons.

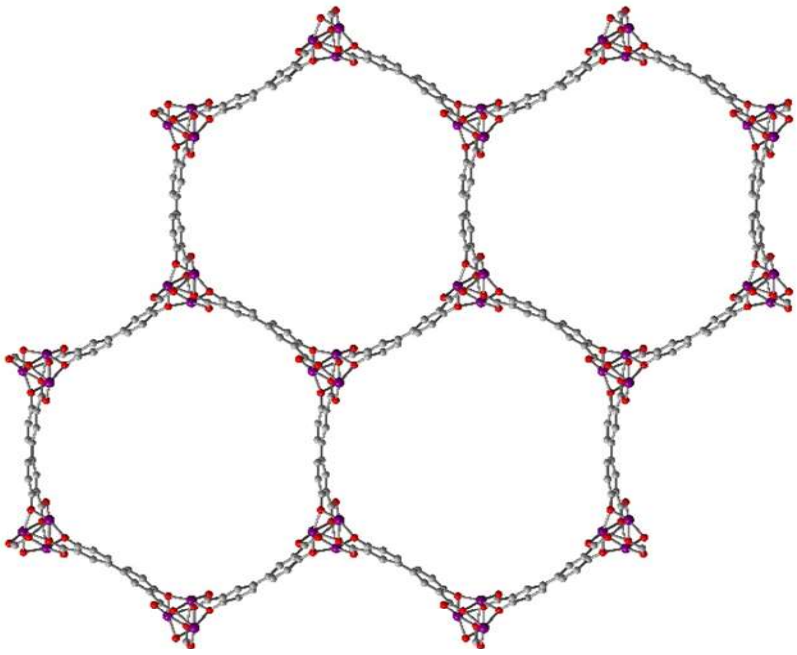

Figure 3.6. The expanded framework M_2(dobpdc) also features helical chains of metal atoms and one-dimensional hexagonal pores but has a pore diameter of approximately 1.8 nanometers. Grey atoms are carbon, red atoms oxygen, and purple atoms are the metal.

I began with the zinc analogue of the framework in preparation for running studies described in Chapter 5, leading to the development of Reaction 3.3. One challenge in extending these syntheses to the larger-pore frameworks is that the organic molecule is now significantly more hydrophobic as a result of the second phenyl ring added. Its solubility in the aqueous-ethanol solution is correspondingly much lower, and dissolution requires more effort. Here, reactant dissolution is a concern because the apparent prevalence of heterogeneous nucleation in the M_2(dobdc) series, displayed in the preceding sections, suggests that it may play a role for the larger-pore frameworks. Heterogeneous nucleation can begin at or near undissolved reactants, where the strongest concentration gradient of the reactant may be found.[9,66] This can be a complicating factor in understanding the crystallization process.

It is also worth noting that the synthesis should be run air-free, or at minimum with solutions sparged of oxygen by bubbling nitrogen through the reaction mixture prior to heating; although the oxidation state of the zinc cations will not change during the synthesis process, the ligand itself can be oxidized when it is deprotonated, either free in solution[67,68] or as part of the framework M_2(dobpdc)[69,70]. Some care should be taken when sparging the solutions; as ethanol is more volatile than water, sparging solutions with reactants present can lead to increased concentration more so for the ligand solution than the metal salt solution. Proper Schlenk technique requires that the solvent be de-oxygenated first and then cannula-transferred to a container with the reactant present.

Extending Reaction 3.1, developed for Zn_2(dobdc), to the synthesis of the larger-pore analogue was accomplished by replacing the ligand H_4dobdc for H_4dobpdc at the same number of equivalents. The product was confirmed to be Zn_2(dobpdc) via powder X-ray diffraction (Fig. 3.S2). In unsilanized vials, the reaction produces long rod morphologies approximately 50–100 microns in length. However, the same reaction run in silanized 20 mL vials yielded crystallites about a millimeter in length (Fig. 3.7.

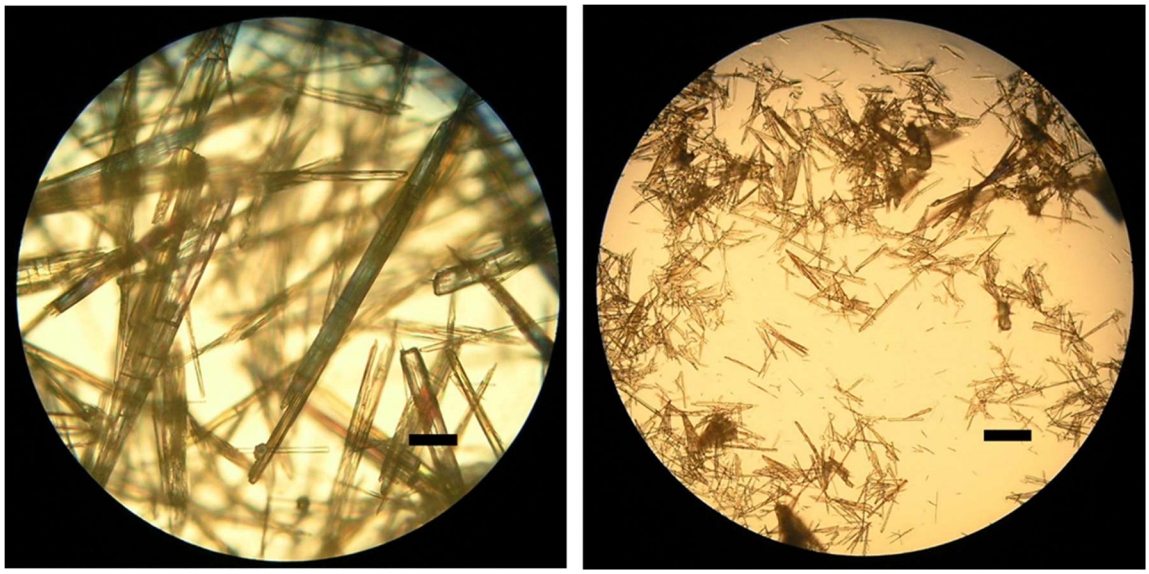

Figure 3.7. At left, Zn_2(dobpdc) synthesized in chlorotrimethylsilane-passivated vial; at right, an identical stock solution grown in unsilanized vials. Scale bar for each is 100 microns.

Here, the surface functionalities present in the native glassware control the resulting crystallite volume by several orders of magnitude. This is strongly suggestive of changes in the nucleation rate. Fast nucleation will lead to many crystallites, depleting the reactant medium and preventing growth to large size; slow nucleation generally leads to a wide population of sizes as nucleation continues alongside growth because of slow depletion of reactants in solution. If the number of nucleation sites are restricted and nucleation elsewhere is hindered, crystals will only begin to form at these sites, leading to very large crystallites.[71] The imperfect results of the Zn_2(dobdc) phase selection suggested that there may be point defects present after silanization. This is consistent with the observed increase in size for Zn_2(dobpdc) in silanized glassware. Notably, this reaction is significantly faster than the current state-of-the-art single crystal synthesis (12 hours rather than several days), leading to its adoption for single crystal studies within our lab. The material may also be formed using the non-coordinating base 2,6-Lutidine, in an extension of Reaction 3.2. Using this synthesis with tetrahydrofuran in the place of ethanol led to the largest crystallite size of any of the M_2(dobpdc) or M_2(dobdc) analogues reported, and, indeed, one of the largest reported of any metal–organic framework (Fig. 3.8).

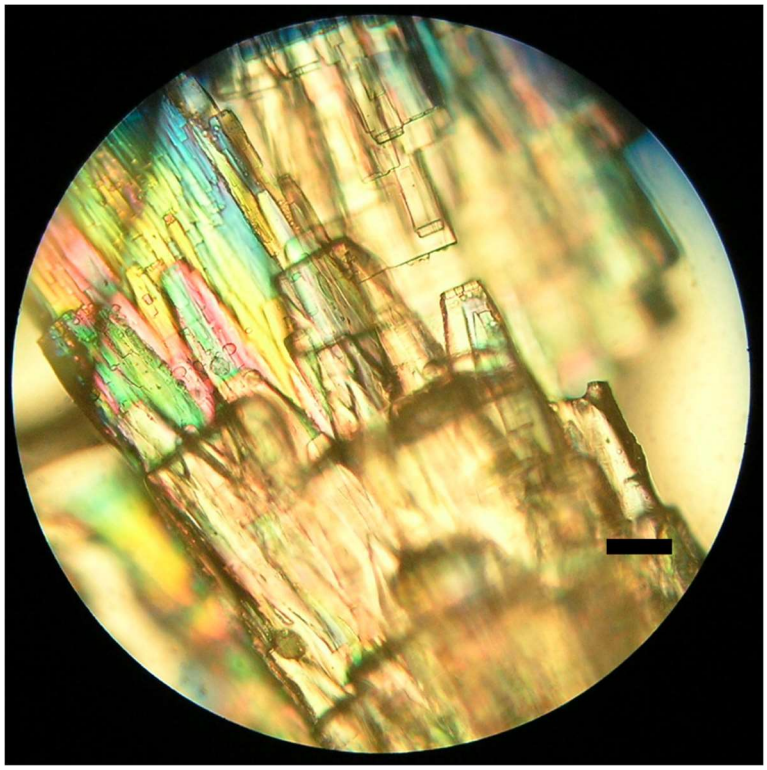

Figure 3.8. Zn_2(dobpdc) grown in silanized vials using 2,6-Lutidine as a base and tetrahydrofuran as a co-solvent. The scale bar is 100 microns. The full length of a crystallite was nearly 10 millimeters.

Surface Effects in Zn_2(dobpdc) Scale-Up. The above surface control was accomplished with the same silanizing agent, chlorotrimethylsilane, which replaces surface silanol groups with capping -$Si(CH_3)_3$ groups. The stoichiometric reaction produces an equivalent of HCl, which can promote the reverse reaction. A different silanization method using N,O-bis(trimethylsilyl)acetamide to induce the same hydrophobic functionality was also used. This

reaction is run at reflux and produces acetamide. N,O-bis(trimethylsilyl)acetamide is more reactive with silica surfaces than chlorotrimethylsilane, leading to more sites covered at equilibrium.[72]

While this second route of silanization produced equally excellent results for the Co_2(dobdc) synthesis using Reaction 3.1, the use of N,O-bis(trimethylsilyl)acetamide-silanized vials led to unexpected results for the synthesis of Zn_2(dobpdc) using Reaction 3.3: very large Zn_2(dobpdc) crystallites did form, but a secondary phase also formed that we believe is likely to be the as of yet unreported phase Zn(H_2dobpdc)•$2H_2O$, an extended analogue to the known phase Zn(H_2dobdc)•$2H_2O$, (Fig. 3.S3). While single crystals large enough to be solved via single crystal X-ray diffraction have not yet been synthesized, the material may be formed under identical conditions to those which form Zn(H_2dobdc)•$2H_2O$, at conditions too acidic for the phenolic groups to be deprotonated.[73] Further, the material hypothesized to be Zn(H_2dobpdc)•$2H_2O$ can also be used in analogous fashion to the smaller-ligand analogue as a starting material for a mixed-metal framework ZnM(dobpdc). In any case, the material is a secondary phase that was not present using the chlorotrimethylsilane-prepared vials. Currently, it appears that using different silanization techniques does allow control over the level of point defects in the protective silane layer, but it is possible from this result that aiming for the highest possible level of surface passivation may be detrimental to production of the desired framework. Going from unsilanized glassware to chlorotrimethylsilane-passivated surfaces appears to merely cut down on the number of nucleation sites, whereas further passivation of silanol groups may actually cut the rate down to such an extent that other pathways may become favorable, some of which result in the new phase. While this is a promising avenue for future research, it represents future work that is outside the scope of this thesis.

One control test of this idea was to silanize two 500 mL round-bottom flasks, one with each silanizing agent, and attempt to use Reaction 3.3 to synthesize Zn_2(dobpdc) in each. Visual inspection shows fewer, more isolated points from which material has grown with the N,O-bis(trimethylsilyl)acetamide-passivation, as compared to the chlorotrimethylsilane-passivation (Fig. 3.S4). Indeed, as expected, the average crystal size is larger for the better passivation process (Fig. 3.9). Simultaneously, more of the second phase also grows for this better passivation process (Fig. 3.9, Fig. 3.S5).

Another interesting observation gleaned from watching the round bottom flasks during crystallization was that the earliest visible material precipitation occurred at a different interface than had been considered yet: the vapor/solution interface. Collection of this material yielded largely block-like morphologies and not the long rods expected of Zn_2(dobpdc). Thus, it is possible that this second phase grows from the solution/vapor interface, which has some limited literature precedence for metal–organic frameworks.[74,75] Cutting down on the area of this surface by filling up the round bottom flask more accomplished the goal of diminishing the amount of second phase formed, although some was still formed and needed to be removed for the purpose of collecting large phase pure Zn_2(dobpdc) crystallites. Fortuitously, the second phase is substantially denser than the desired framework. These phases can be readily separated by first soaking the solid mixture in methanol (yielding the methanol solvated framework) and then dispersing in chloroform; the second phase sinks while the less dense porous framework floats.

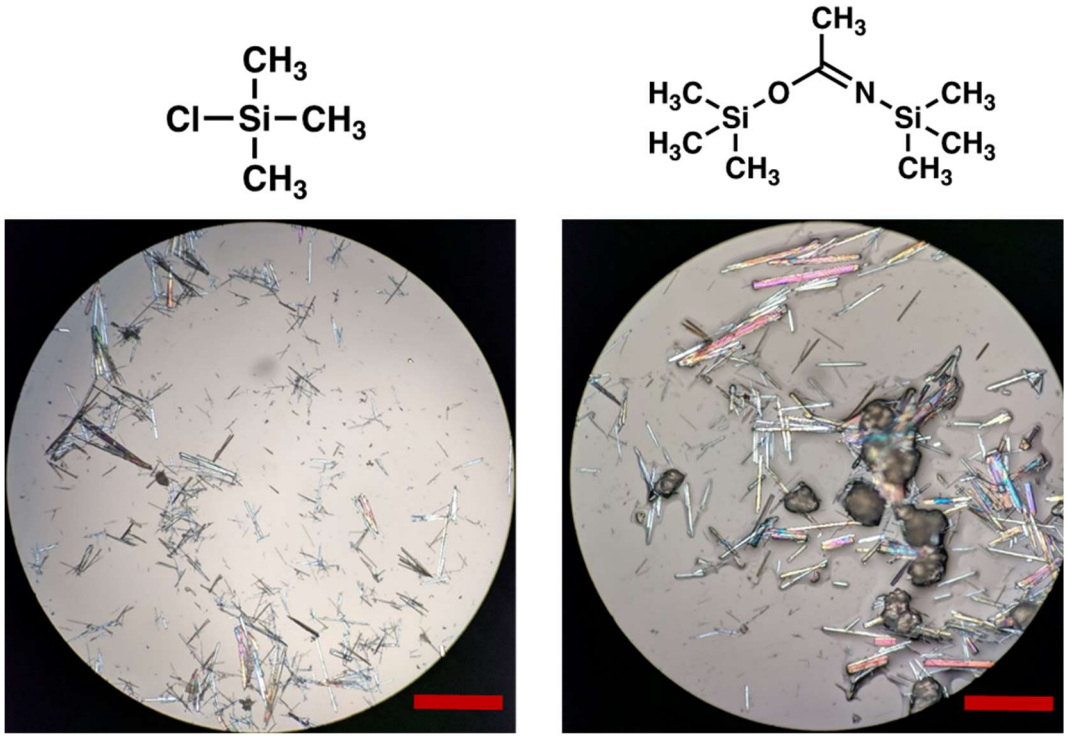

Figure 3.9. The results from attempted Zn_2(dobpdc) synthesis includes two phases using either silanizing method, above, when the reaction is scaled up. Scale bars 400 microns. Average crystallite size is much larger using N,O-bis(trimethylsilyl)acetamide, but more of the second phase is also observed.

Intentional Growth from Surfaces for M_2(dobdc) and Initial Atomic Force Microscopy Studies. From the previous case studies, the exposed functionalities of the glass surfaces must play an outsize role in the nucleation of M_2(dobdc) and M_2(dobpdc). Imparting hydrophobicity to the exposed polar functionalities can affect particle size, shape, dispersity, and crystalline phase. Seeking to follow up on this, I began running experiments to effect nucleation directly from surfaces by suspending a surface from which the framework may grow into a growth solution medium. Two different surfaces were examined: amorphous silica glass and mica, the latter of which is a group of sheet silicates with nearly perfect basal plane cleavage[76] popular with microscopists for its atomically flat surface (Fig. 3.S6). Initial studies began with the Zn_2(dobdc) synthesis, because of its demonstrated phase- and size-selectivity based on surface site availability.

I conducted a series of stopped-time observations of Zn_2(dobdc) growth on mica surfaces, wherein freshly cleaved mica was suspended into a growth solution (Fig. 3.S7). The first tests were conducted at 70 °C, chosen to avoid appreciable evaporation of the growth solution, as the vials with substrate suspended could not be fully closed (normal synthetic conditions are 75 °C). Tests were run with surfaces suspended into both silanized and unsilanized vials, as nucleation on the glassware should affect the overall mass balance for the synthesis as thus nucleation and growth at the suspended mica surface. The mica surfaces were removed after some set amount of time and placed in our powder X-ray diffractometer. At about 4 minutes of growth at 70 °C, the highest-angle peak corresponding to Zn_2(dobdc) appears, indicating that Zn_2(dobdc) will indeed grow from mica surfaces (Fig. 3.10).

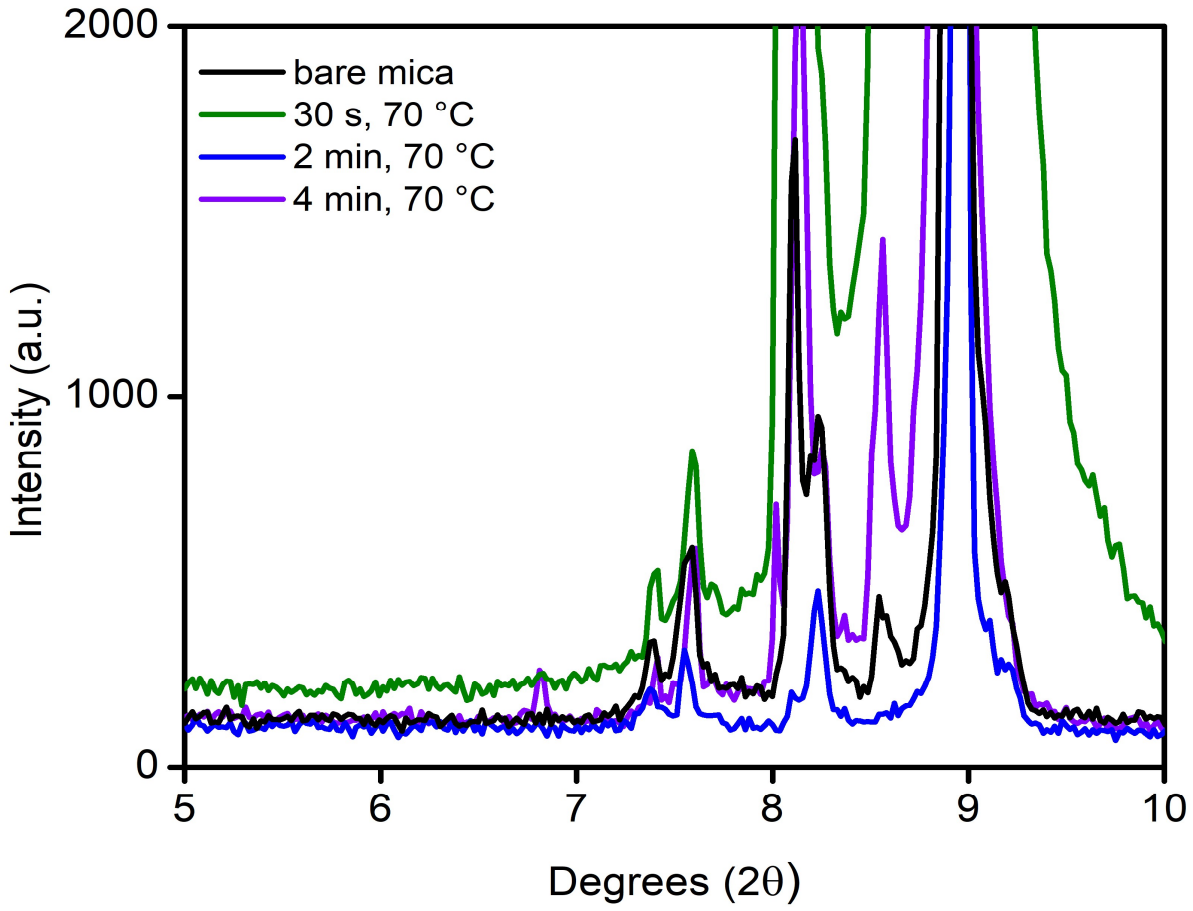

Figure 3.10. At four minutes, the highest angle peak corresponding to Zn_2(dobdc), near 6.8 degrees, begins to appear. All other peaks belong to mica. Because the mica is a large single crystal, differing orientations of the crystal relative to the X-ray beam causes differences in intensity between these reflections.

There were several reasons to attempt lower-temperature studies, primarily that any proposed AFM or other in situ studies would most easily be done at room temperature. Any in situ cell containing resistive heating elements will lead to material formation directly at the heating element itself, which may or may not be within the viewing range for the instrument. A comparison of syntheses with Reaction 3.1 to form Zn_2(dobdc) across different temperatures revealed that even decreasing the reaction temperature from 75 °C to 40 °C greatly exacerbated the material tendency to form on the walls of the glassware (Fig. 3.10). Here, at lower temperatures, Zn_2(dobdc) forms at very isolated spots as very large columns growing from the same point. In general, the barrier to nucleation is lower for heterogeneous pathways than homogeneous pathways, enough so that several argue in the literature that nearly all nucleation which occurs is heterogeneous.[71,77,78] Lowering the temperature thus gives the additional benefit of helping to diminish though not necessarily eliminate potential solution-based nucleation.

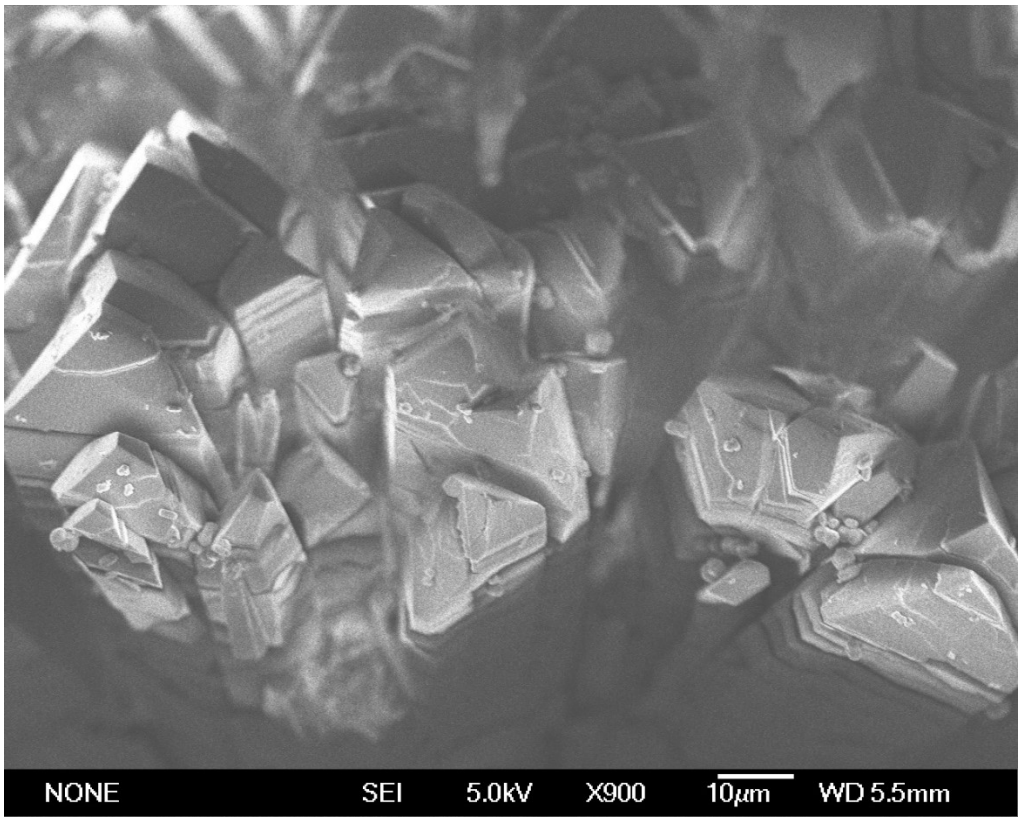

Figure 3.11. Zn_2(dobdc) grown from unsilanized vials at 40 °C has much larger crystallites which grow from seemingly discrete spots on the glassware.

Initial trials at room temperature were left for twelve hours with mica suspended into the growth solution sitting at 25 °C. Under these conditions, Zn_2(dobdc) forms at the surface as confirmed by powder X-ray diffraction (Fig. 3.11). The shoulder on the first peak is characteristic of single crystals with preferred orientation on the pXRD stage.[77] The same experiment was run with a microscope slide (amorphous silica) suspended into the same growth solution, and large crystallites of Zn_2(dobdc) similarly formed at the surface. Further stopped-time experiments were conducted on glass surfaces with reaction time intervals ranging from 5 minutes to 3 hours. Even after only 5 minutes at room temperature, crystals are evident in optical micrographs (Fig. 3.S8). After 45 minutes of growth at room temperature, several crystallites as large as 80 microns in length are apparent (Fig. 3.S9). Notably, the crystallites are isolated across the surface of the glass slide, not homogeneously distributed. This is likely related to inhomogeneities of surface functionalities (the glass slides were not silanized).

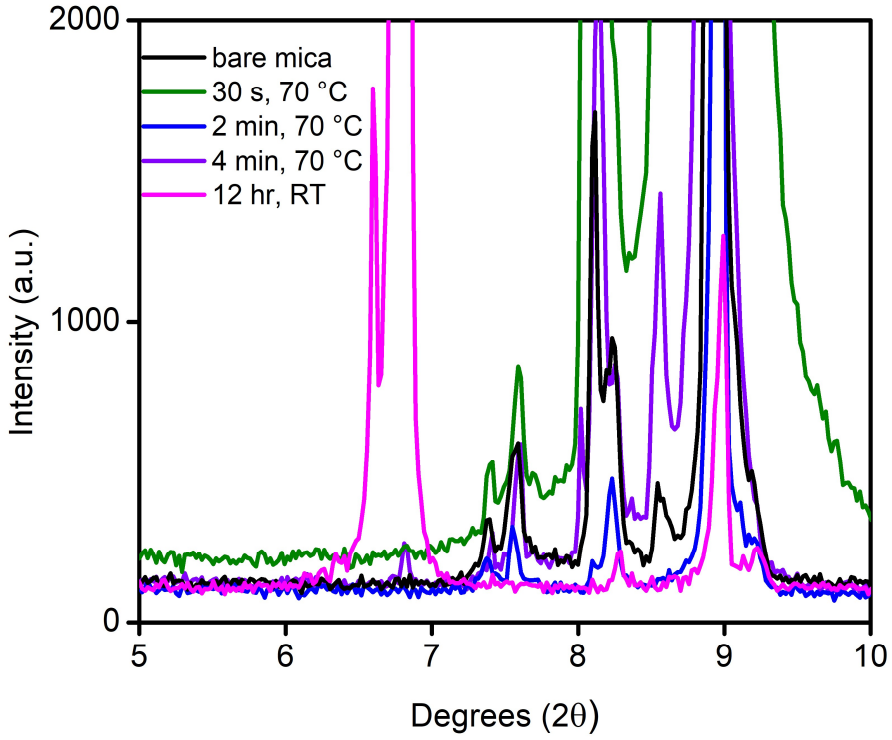

Figure 3.12. Very large single crystals of Zn_2(dobdc) grew on mica at room temperature overnight, here overlaid with early time points at higher temperature. The shoulder on the first peak is characteristic of single crystals with preferred orientation on the pXRD stage.

A tapping-mode atomic force microscopy image of a section of the glass surface at only 5 minutes of room temperature growth revealed small peaks protruding vertically from the surface approximately 5–10 nanometers in height, as well as a film that was approximately 1 nanometer in height. Similar trials were run for other metal analogues Mg_2(dobdc), Co_2(dobdc), and Ni_2(dobdc). Within five minutes, on either glass or mica substrates, structures form on the surface for each reaction mixture. Although the glass surfaces had significant charging, which impeded tapping-mode atomic force microscopy analysis, the mica surfaces were examined across this metal series (Fig. 3.S10–3.S16). While for amorphous silica, the presence of silanol groups is a reasonable hypothesis for nucleation sites, similar sites do not exist on the mica surface. Instead, the surface imparts a partial negative charge, which can adsorb metal cations. Clearly, significant reactivity is happening at the surface for all metal analogues.

In all cases, thin peaks appear to grow nearly perpendicularly from the surface. The largest structures by far are those of the Zn_2(dobdc) synthesis (Fig. 3.S10), consistent with the prior observations of significant surface control. The least amount of surface-grown material, similarly, is Co_2(dobdc), which is also the synthesis that is least affected by silanization, which adds consistency but does not impart huge changes to particle size or shape for the high-temperature synthesis of Reaction 3.1. For the nickel synthesis (Fig. 3.S11–3.S12), the cobalt synthesis (Fig. 3.S13–3.S14), and the magnesium synthesis (Fig 3.S15–3.S16), thin film formation is also observed. Control tests were run with only one reactant (either the ligand or the metal salt) and several solvent combinations (water, ethanol, or water/ethanol). Both the metal salt and the ligand

needed to be present for precipitate to be observed, implying that the structures formed are likely coordination solids, although the phase could not be identified using powder X-ray diffraction. This thin film is likely either amorphous or too small in quantity for the diffractometer used, particularly in contrast to the large signal from the single-crystalline mica substrate.

3.4 Outlook and Conclusions

The phase, size, morphology, and particle distribution of M_2(dobdc) and M_2(dobpdc) frameworks are sensitive not only to the expected solution variables but also to the functionalities present in the reaction vessel itself. While this interface is used intentionally in the literature to grow metal–organic frameworks that are designed to stay attached to the surface, it is entirely ignored as a normal variable in hydrothermal and solvothermal metal–organic framework syntheses. Despite this, I have found it to be a singularly important variable across nearly the entire series of M_2(dobdc) and M_2(dobpdc) frameworks. The failure to address and control reaction vessel surface functionalities leads to irreproducible syntheses, an important and persistent problem in the field of metal–organic frameworks. Since demonstrating that the surfaces may be used to control the resulting synthetic products for M_2(dobdc) and M_2(dobpdc), the strategy of surface passivation to control nucleation sites has led to size control effects for very different materials, including imidazolate frameworks, and more metals than are discussed in this chapter, including vanadium-based frameworks.

Further, the degree of control observed is consistent with the literature on metal adsorption at surfaces. Metal cations tend to adsorb as a function of their charge density, as would be expected for largely ionic interactions at the surface. In accordance, the higher the charge density, the more important this effect: the zinc frameworks are particularly susceptible, as are the magnesium analogues, where a silanized surface means that the framework will not form at all. The cobalt analogue, on the other hand, becomes more homogeneous in particle distribution as a function of silanization, as the effect of metal adsorption at the surface is lessened relative to the zinc frameworks. While this chapter only covers case studies, the processes of metal adsorption at surfaces and interfacial nucleation are likely playing undetected, often important roles for a vast number of frameworks. As the materials proceed towards industrialization and synthesis scales up volume and surfaces unequally, these variables will only become more important. For future crystallization studies, scaling up syntheses, and aiming for specific crystallite phase and size, it will be important to examine and control the interface functionalities available to the synthesizing system.

3.5 Acknowledgments

This work was supported by ExxonMobil Research and Engineering Company. The use of atomic force microscopy instruments is gratefully acknowledged to the Molecular Foundry at Lawrence Berkeley National Laboratory. I thank Paul Ashby for discussion, guidance, and help with atomic force microscopy experiments. I thank Simon Weston and Joe Falkowski for helpful discussion and suggestions. In addition, I would like to acknowledge Peidong Yang for the use of his scanning electron microscope.

3.6 References and Supplementary Figures

(1) Stavitski, E.; Goesten, M.; Juan-Alcañiz, J.; Martinez-Joaristi, A.; Serra-Crespo, P.; Petukhov, A. V.; Gascon, J.; Kapteijn, F. *Angew. Chemie - Int. Ed.* **2011**, *50* (41), 9624.
(2) Sanil, E. S.; Cho, K.-H.; Lee, S.-K.; Lee, U.-H.; Ryu, S. G.; Lee, H. W.; Chang, J.-S.; Hwang, Y. K. *J. Porous Mater.* **2015**, *22* (1), 171.
(3) Adarsh, N. N.; Kumar, D. K.; Dastidar, P. *CrystEngComm* **2008**, *10* (11), 1565.
(4) Fan, J.; Shu, M.-H.; Okamura, T.; Li, Y.-Z.; Sun, W.-Y.; Tang, W.-X.; Ueyama, N. *New J. Chem.* **2003**, *27* (9), 1307.
(5) Israr, F.; Chun, D.; Kim, Y.; Kim, D. K. *Ultrason. Sonochem.* **2016**, *31*, 93.
(6) Sonnauer, A.; Hoffmann, F.; Fröba, M.; Kienle, L.; Duppel, V.; Thommes, M.; Serre, C.; Férey, G.; Stock, N. *Angew. Chemie Int. Ed.* **2009**, *48* (21), 3791.
(7) Biemmi, E.; Christian, S.; Stock, N.; Bein, T. *Microporous Mesoporous Mater.* **2009**, *117* (1–2), 111.
(8) Li, Y.-S.; Bux, H.; Feldhoff, A.; Li, G.-L.; Yang, W.-S.; Caro, J. *Adv. Mater.* **2010**, *22* (30), 3322.
(9) Maserati, L.; Meckler, S. M.; Li, C.; Helms, B. A. *Chem. Mater.* **2016**, *28* (5), 1581.
(10) Qin, R.; Zeng, H. C. *ACS Sustain. Chem. Eng.* **2018**, *6* (11), 14979.
(11) Gu, J.; Wen, M.; Liang, X.; Shi, Z.; Kirillova, M.; Kirillov, A. *Crystals* **2018**, *8* (2), 83.
(12) Forster, P. M.; Stock, N.; Cheetham, A. K. *Angew. Chemie Int. Ed.* **2005**, *44* (46), 7608.
(13) Bauer, S.; Stock, N. *Angew. Chemie Int. Ed.* **2007**, *46* (36), 6857.
(14) Millange, F.; El Osta, R.; Medina, M. E.; Walton, R. I. *CrystEngComm* **2011**, *13* (1), 103.
(15) Stock, N.; Biswas, S. *Chem. Rev.* **2012**, *112* (2), 933.
(16) Chernov, A. A. *Modern Crystallography III*; Springer Berlin Heidelberg, 1984; Vol. 36.
(17) Garside, J. Nucleation. In *Biological Mineralization and Demineralization*; Springer Berlin Heidelberg: Berlin, Heidelberg, 1982; pp 23–35.
(18) *Industrial Crystallization*; Mullin, J. W., Ed.; Springer US: Boston, MA, 1976.
(19) Shekhah, O.; Wang, H.; Kowarik, S.; Schreiber, F.; Paulus, M.; Tolan, M.; Sternemann, C.; Evers, F.; Zacher, D.; Fischer, R. A. *J. Am. Chem. Soc.* **2007**, *129* (49), 15118.
(20) Scherb, C.; Schödel, A.; Bein, T. *Angew. Chemie - Int. Ed.* **2008**, *47* (31), 5777.
(21) Robinson, A. L.; Stavila, V.; Zeitler, T. R.; White, M. I.; Thornberg, S. M.; Greathouse, J. A.; Allendorf, M. D. *Anal. Chem.* **2012**, *84* (16), 7043.
(22) Biemmi, E.; Scherb, C.; Bein, T. *J. Am. Chem. Soc.* **2007**, *129* (26), 8054.
(23) Heinke, L.; Gliemann, H.; Tremouilhac, P.; Wöll, C. SURMOFs: Liquid-Phase Epitaxy of Metal-Organic Frameworks on Surfaces. In *The Chemistry of Metal-Organic Frameworks: Synthesis, Characterization, and Applications*; Wiley-VCH Verlag GmbH & Co. KGaA: Weinheim, Germany, 2016; pp 523–550.
(24) Heinke, L.; Wöll, C. *Adv. Mater.* **2019**, *31*, 1806324.
(25) Ameloot, R.; Vermoortele, F.; Vanhove, W.; Roeffaers, M. B. J.; Sels, B. F.; De Vos, D. E. *Nat. Chem.* **2011**, *3* (5), 382.
(26) Grzesiak, A. L.; Uribe, F. J.; Ockwig, N. W.; Yaghi, O. M.; Matzger, A. J. *Angew. Chemie Int. Ed.* **2006**, *45* (16), 2553.
(27) Jawor, A.; Jeong, B.-H.; Hoek, E. M. V. *J. Nanoparticle Res.* **2009**, *11* (7), 1795.

(28) Brar, T; France, P; Smirniotis, P. G. *Ind. Eng. Chem. Res.* **2001**, *40*, 1133.
(29) Gibbs, J. *Trans Connect Acad Sci* **1876**, *3*, 108.
(30) Gibbs, J. *Trans Connect Acad Sci* **1878**, *16*, 343.
(31) Bai, L.; Chang, N.; Li, M.; Wang, Y.; Nan, G.; Zhang, Y.; Hu, D.; Zeng, G.; Wei, W. *Microporous Mesoporous Mater.* **2017**, *241*, 392.
(32) Ni, Z.; Masel, R. I. *J. Am. Chem. Soc.* **2006**, *128* (38), 12394.
(33) Klinowski, J.; Almeida Paz, F. A.; Silva, P.; Rocha, J. *Dalton Trans*. **2011**, 321.
(34) Bétard, A.; Zacher, D.; Fischer, R. A. *CrystEngComm* **2010**, *12* (11), 3768.
(35) Rezaei, F.; Lawson, S.; Hosseini, H.; Thakkar, H.; Hajari, A.; Monjezi, S.; Rownaghi, A. A. *Chem. Eng. J.* **2017**, *313*, 1346.
(36) Campbell, J.; Tokay, B. *Microporous Mesoporous Mater.* **2017**, *251*, 190.
(37) Bradshaw, D.; Garai, A.; Huo, J. *Chem. Soc. Rev.* **2012**, *41* (6), 2344.
(38) Zhao, M.; Lu, Q.; Ma, Q.; Zhang, H. *Small Methods* **2017**, *1* (1–2), 1600030.
(39) Iler, R. K. *The Chemistry of Silica : Solubility, Polymerization, Colloid and Surface Properties, and Biochemistry*; Wiley, 1979.
(40) Papirer, E. *Adsorption on Silica Surfaces*; Marcek Dekker, 2000.
(41) Rimola, A.; Costa, D.; Sodupe, M.; Lambert, J.-F.; Ugliengo, P. *Chem. Rev.* **2013**, *113* (6), 4216.
(42) Dalstein, L.; Potapova, E.; Tyrode, E. *Phys. Chem. Chem. Phys* **2017**, *19*, 10343.
(43) Dugger, D. L.; Stanton, J. H.; Irby, B. N.; McConnell, B. L.; Cummings, W. W.; Maatman, R. W. *J. Phys. Chem.* **1964**, *68* (4), 757.
(44) Persson, P.; Parks, G. A.; Brown, G. E. *Langmuir* **1995**, *11* (10), 3782.
(45) James, R. O.; Healy, T. W. *J. Colloid Interface Sci.* **1972**, *40* (1), 42.
(46) Bourikas, K.; Kordulis, C.; Vakros, J.; Lycourghiotis, A. *Adv. Colloid Interface Sci.* **2004**, *110* (3), 97.
(47) Seed, B. Silanizing Glassware. In *Current Protocols in Immunology*; John Wiley & Sons, Inc.: Hoboken, NJ, USA, 2001; Vol. 21, p A.3K.1-A.3K.2.
(48) Ghermani, N. E.; Morgant, G.; d'Angelo, J.; Desmaële, D.; Fraisse, B.; Bonhomme, F.; Dichi, E.; Sgahier, M. *Polyhedron* **2007**, *26* (12), 2880.
(49) Forster, P. M.; Burbank, A. R.; Livage, C.; Férey, G.; Cheetham, A. K. *Chem. Commun.* **2004**, *4* (4), 368.
(50) Forster, P. M.; Stock, N.; Cheetham, A. K. *Angew. Chemie - Int. Ed.* **2005**, *44* (46), 7608.
(51) Kam, K. C.; Young, K. L. M.; Cheetham, A. K. *Cryst. Growth Des.* **2007**, *7* (8), 1522.
(52) Appelhans, L. N.; Kosa, M.; Radha, A. V.; Simoncic, P.; Navrotsky, A.; Parrinello, M.; Cheetham, A. K. *J. Am. Chem. Soc.* **2009**, *131* (42), 15375.
(53) Yeung, H. H. M.; Cheetham, A. K. *Dalt. Trans.* **2014**, *43* (1), 95.
(54) Kieslich, G.; Kumagai, S.; Butler, K. T.; Okamura, T.; Hendon, C. H.; Sun, S.; Yamashita, M.; Walsh, A.; Cheetham, A. K. *Chem. Commun.* **2015**, *51* (85), 15538.
(55) Yeung, H. H.-M.; Wu, Y.; Henke, S.; Cheetham, A. K.; O'Hare, D.; Walton, R. I. *Angew. Chemie - Int. Ed.* **2016**, *55* (6), 2012.
(56) Li, Q. Q.; Kang, Y. F.; Ren, C. Y.; Yang, G. P.; Liu, Q.; Liu, P.; Wang, Y. Y. *CrystEngComm* **2015**, *17* (4), 775.
(57) Rosa, I. M. L.; Costa, M. C. S.; Vitto, B. S.; Amorim, L.; Correa, C. C.; Pinheiro, C. B.;

Doriguetto, A. C. *Cryst. Growth Des.* **2016**, *16* (3), 1606.
(58) Cheetham, A. K.; Kieslich, G.; Yeung, H. H.-M. *Acc. Chem. Res.* **2018**, *51* (3), 659.
(59) Caira, M. R. Crystalline Polymorphism of Organic Compounds; Springer, Berlin, Heidelberg, 2007; pp 163–208.
(60) McPherson, A.; Gavira, J. A. *Acta Cryst.* **2014**, *F70*, 2.
(61) Marcus, Y. *Chem. Rev.* **1988**, *88*, 1475.
(62) Roberts, D. R.; Ford, R. G.; Sparks, D. L. *J. Colloid Interface Sci.* **2003**, *263*, 364.
(63) McDonald, T. M.; Lee, W. R.; Mason, J. A.; Wiers, B. M.; Hong, C. S.; Long, J. R. *J. Am. Chem. Soc.* **2012**, *134* (16), 7056.
(64) McDonald, T. M.; Mason, J. A.; Kong, X.; Bloch, E. D.; Gygi, D.; Dani, A.; Crocella, V.; Giordanino, F.; Odoh, S. O.;Drisdell, W.; Vlaisavljevich, B.; Dzubak, A. L.; Poloni, R.; Schnell, S. K.; Planas, N.; Lee, K.; Pascal, T.; Wan, L. F.; Prendergast, D.; Neaton, J. B.; Smit, B.; Kortright, J. B.; Gagliardi, L.; Bordiga, S.; Reimer, J. A.; Long, J. R. *Nature* **2015**, *519* (7543), 303.
(65) Siegelman, R. L.; McDonald, T. M.; Gonzalez, M. I.; Martell, J. D.; Milner, P. J.; Mason, J. A.; Berger, A. H.; Bhown, A. S.; Long, J. R. *J. Am. Chem. Soc.* **2017**, *139* (30), 10526.
(66) Walton, A. G. Nucleation of Crystals from Solution. *Science* **1965**, *148* (3670), 601.
(67) Hankache, J.; Wenger, O. S. *Chem. Rev.* **2011**, *111* (8), 5138.
(68) Nelsen, S. F.; Weaver, M. N.; Telo, J. P. *J. Phys. Chem. A* **2007**, *111* (43), 10993.
(69) Aubrey, M. L.; Ameloot, R.; Wiers, B. M.; Long, J. R. *Energy Environ. Sci.* **2014**, *7* (2), 667.
(70) Aubrey, M. L.; Long, J. R. *J. Am. Chem. Soc.* **2015**, *137* (42), 13594.
(71) Vekilov, P. G. *Cryst. Growth Des.* **2010**, *10* (12), 5007.
(72) Klebe, J. F.; Finkbeiner, H.; White, D. M. *J. Am. Chem. Soc.* **1966**, *88* (14), 3390.
(73) Kim, D.; Coskun, A. *Angew. Chemie Int. Ed.* **2017**, *56* (18), 5071.
(74) Makiura, R.; Konovalov, O. *Sci. Rep.* **2013**, *3* (1), 2506.
(75) Tuccitto, N.; Amato, T.; Gangemi, C. M. A.; Trusso Sfrazzetto, G.; Puglisi, R.; Pappalardo, A.; Ballistreri, F. P.; Messina, G. M. L.; Li-Destri, G.; Marletta, G. *Langmuir* **2018**, *34* (39), 11706.
(76) Bragg, W. L. *Atomic Structure of Minerals*; Cornell University Press, 1937.
(77) Liu, X. Y. *J. Chem. Phys.* **2000**, *112* (22), 9949.
(78) Sear, R. P. *CrystEngComm* **2014**, *16* (29), 6506.
(79) Pecharsky, V. K.; Zavalij, P. Y. *Fundamentals of Powder Diffraction and Structural Characterization of Materials*; Springer US: Boston, MA, 2005.

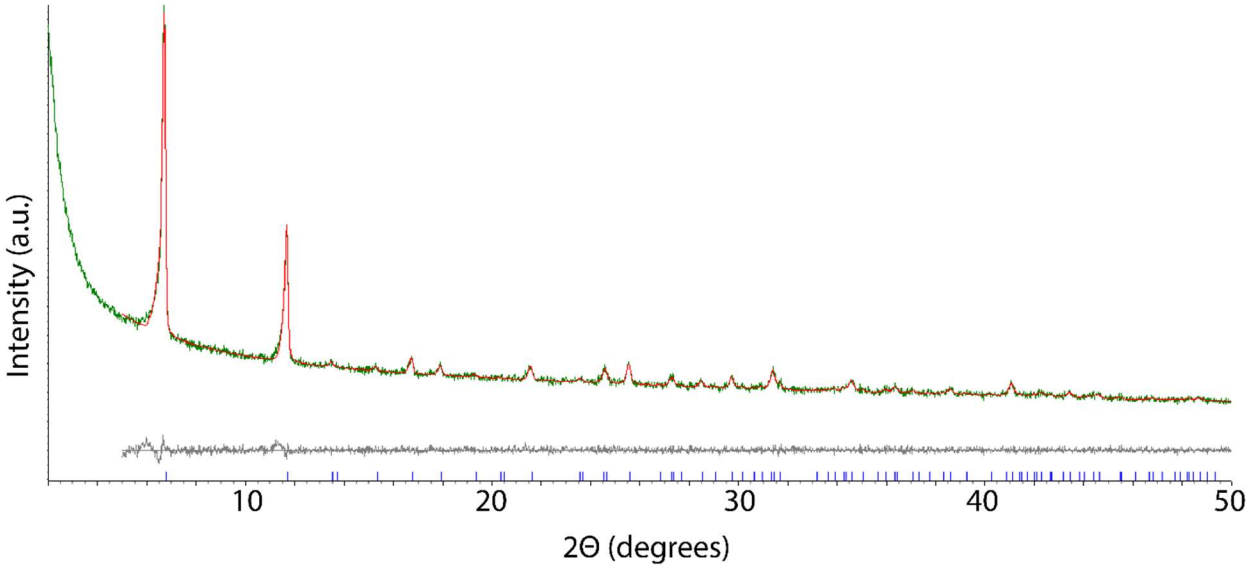

Figure 3.S1. The powder X-ray diffraction pattern for the sheet morphology of Co_2(dobdc) matches the bulk structure fitted with a simulated pattern, indicating that the material is highly crystalline and no other crystalline phases are present.

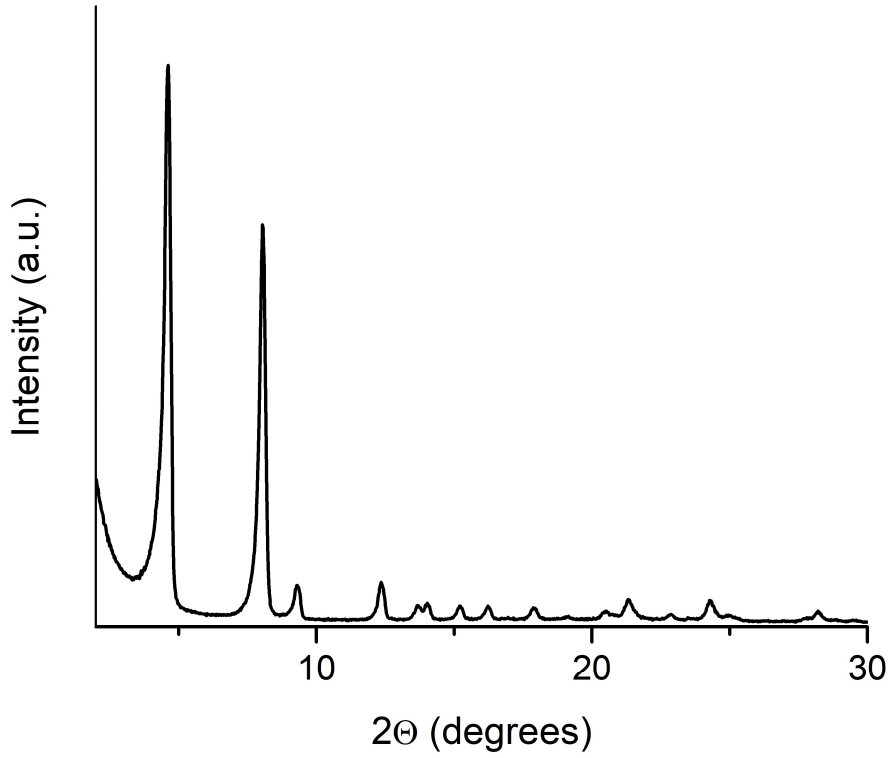

Figure 3.S2. The powder X-ray diffraction pattern of Zn_2(dobpdc) formed via Reaction 3.3, which matches the reported pattern for the material.

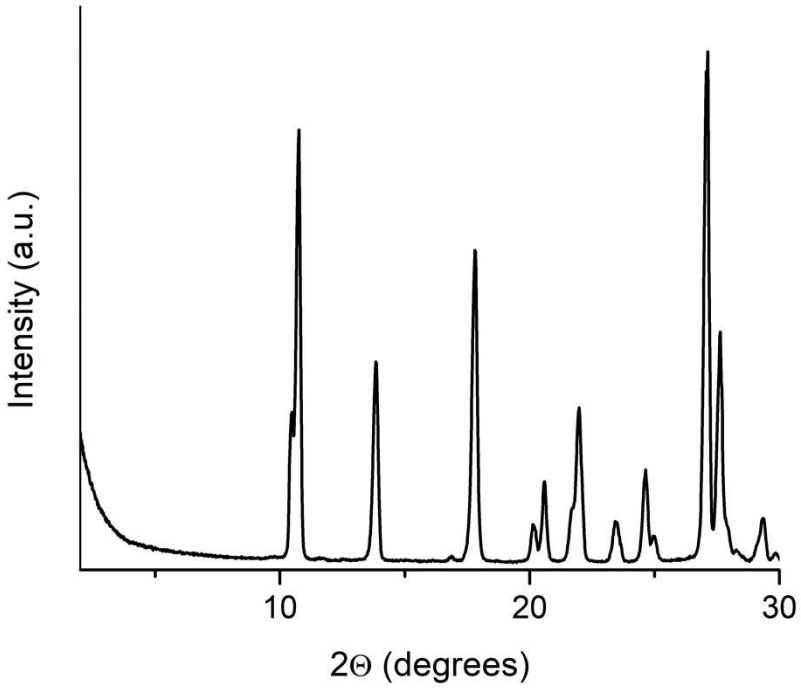

Figure 3.S3. The powder X-ray diffraction pattern of the secondary phase formed at scaled up conditions for Zn_2(dobpdc) using Reaction 3.3.

Figure 3.S4. Although it is difficult to visually show, the silanization process using chlorotrimethylsilane (at left) has more points of nucleation than the silanized vials using N,O-bis(trimethylsilyl)acetamide (results at right).

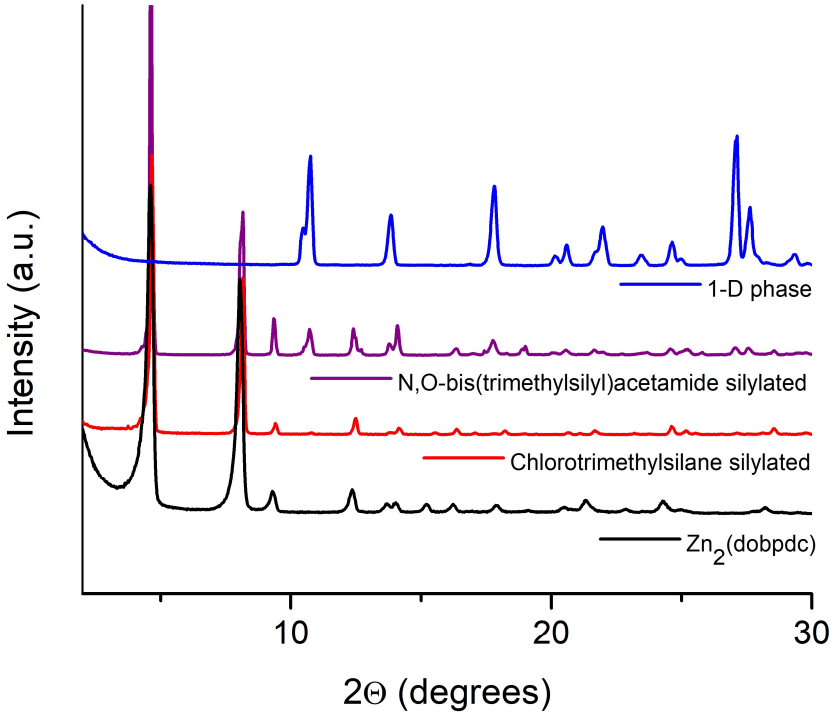

Figure 3.S5. Both silanization methods make some amount of MOF and 1-D chain using Reaction 3, but the use of N,O-bis(trimethylsilyl)acetamide as a silylating agent leads to more 1-D chain than using chlorotrimethylsilane.

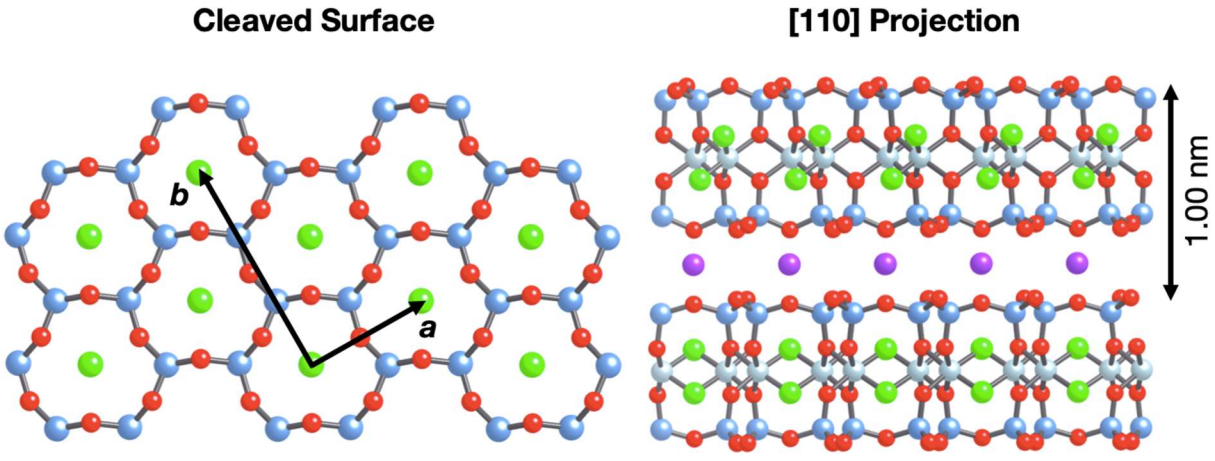

Figure 3.S6. Projections of the surface of muscovite mica indicate terminal oxygens along the basal plane. The excellent basal cleavage stems from the two-dimensional hexagonal structure. Color coded: K (purple), Si (light blue), Al (grey), disordered OH (green), all other O (red).

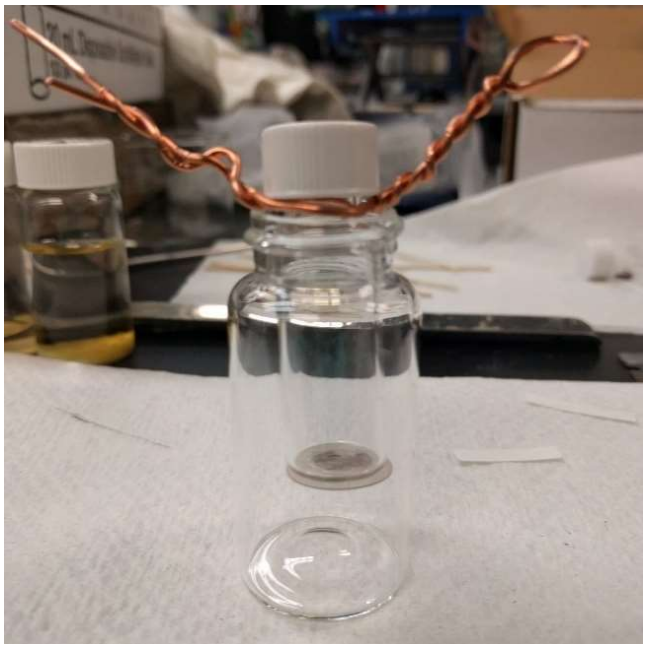

Figure 3.S7. Although there is no growth solution in this image, this is a configurational example of the ex situ trials used to determine minimum time lengths of surface-growth on mica. The crystals grew downwards from the mica, which had been epoxied onto the bottom of a 4 mL glass vial. Solutions were unstirred; if the experiments required heat, the 20 mL vial was placed into an oil bath.

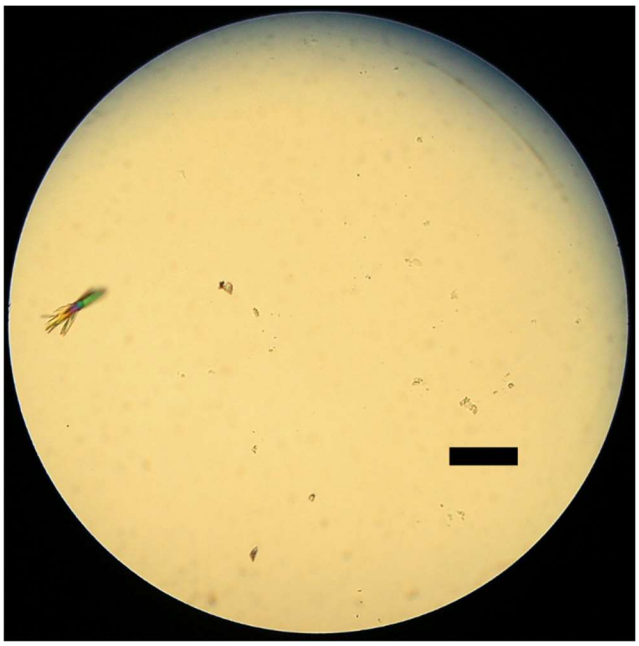

Figure 3.S8. Glass slide left in growth solution for 5 minutes. Some 50 micron-sized crystals already evident, with some smaller particles. Scale bar 50 microns.

Zn_2(dobdc) on mica

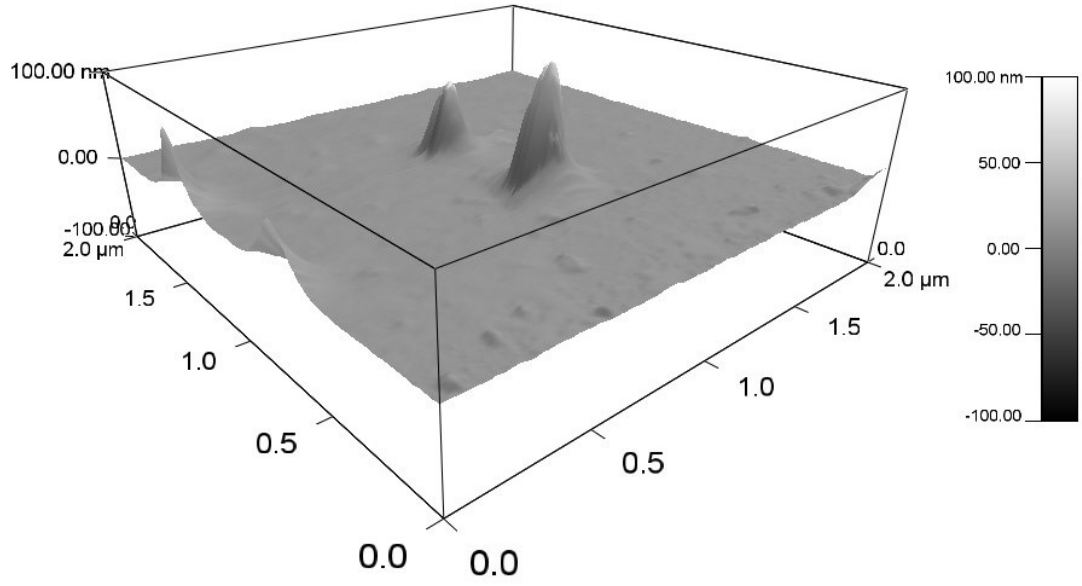

Figure 3.S10. On mica, most features grown from the Reaction 3.1-Zn_2(dobdc) were tall (fifty to one hundred nanometer) peaks.

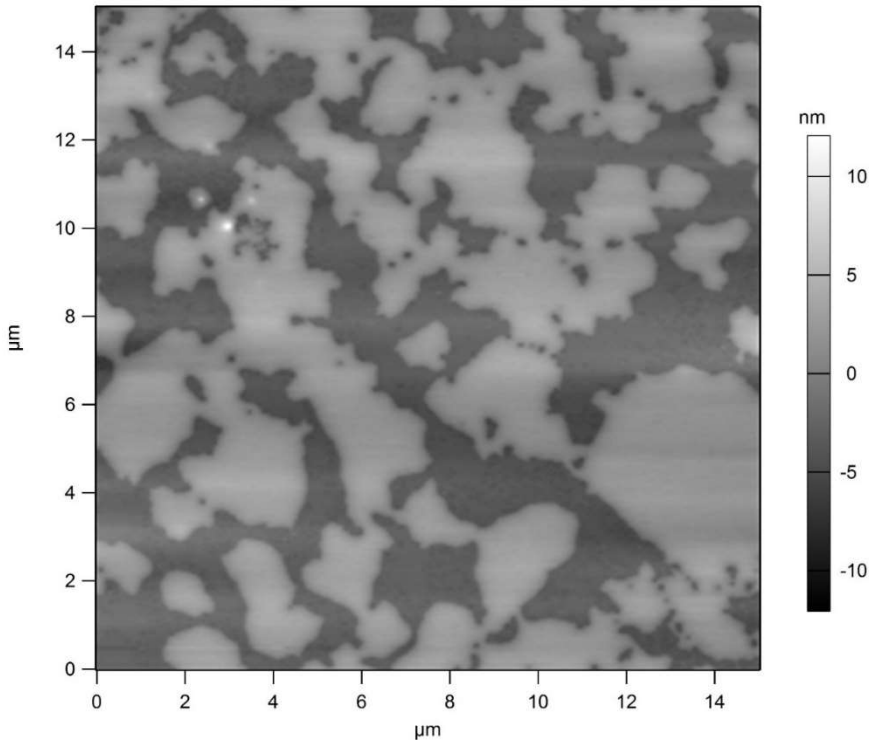

Figure 3.S11. After five minutes with Reaction 3.1-Ni_2(dobdc) growth solution, the mica surface was covered by a consistent six nanometer film. Phase contrast imaging confirms the film has different mechanical properties than mica.

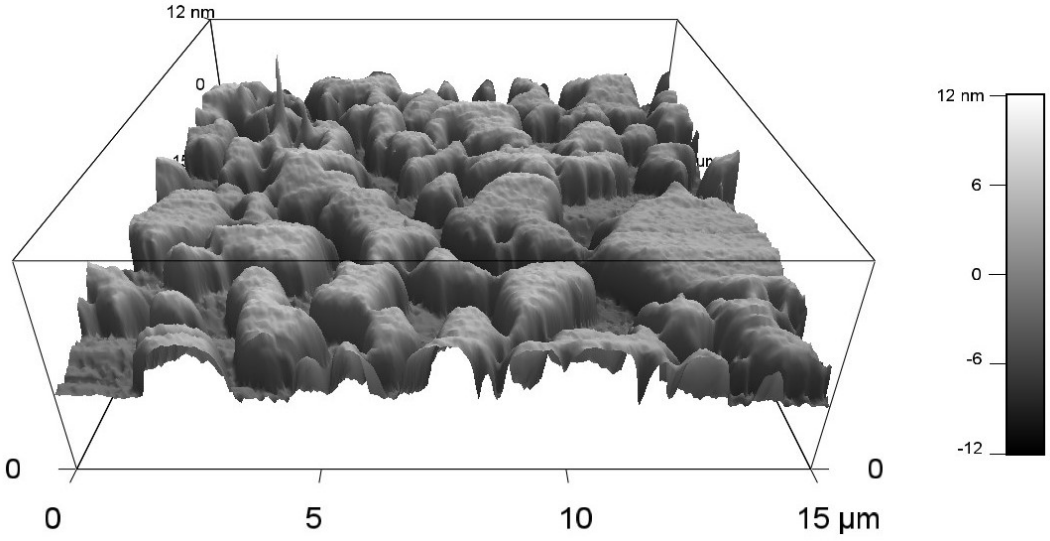

Figure 3.S12. Height-mapping of Figure 3.S11 displays the presence of some thin peaks growing straight up from the film, leading to the interesting hypothesis that the Ni_2(dobdc) phase may grow off a second thin film that appears at glassware surfaces.

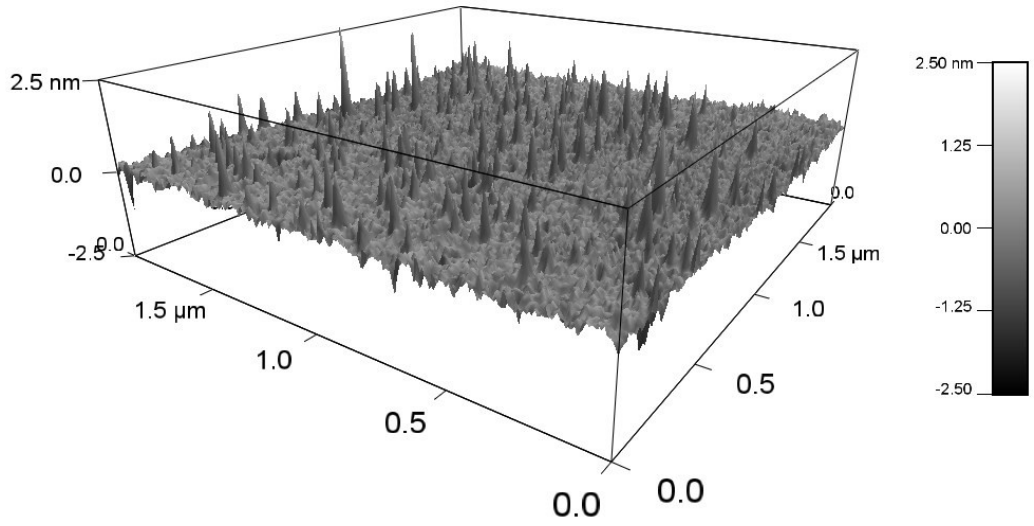

Figure 3.S13. Reaction 3.1-Co_2(dobdc) led to mostly very small, thin peaks, with significantly less material present on the surface by volume; this is consistent with the belief that lower cobalt surface adsorption (due to its lower charge density relative to zinc, magnesium, or nickel) leads to less surface growth.

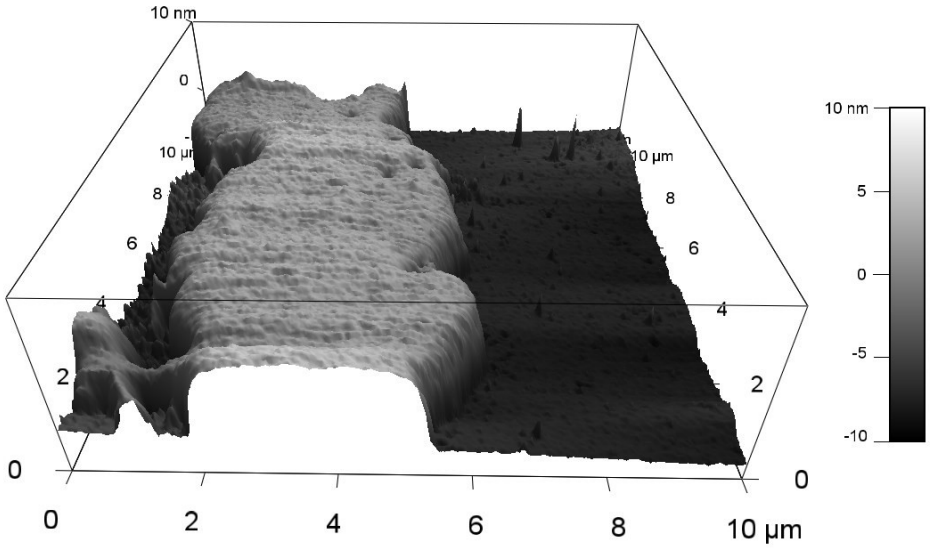

Figure 3.S14. Of note, the samples with Co_2(dobdc) on mica also displayed some limited evidence of six nanometer thickness films, like those displayed with nickel sample in Figure 3.S11.

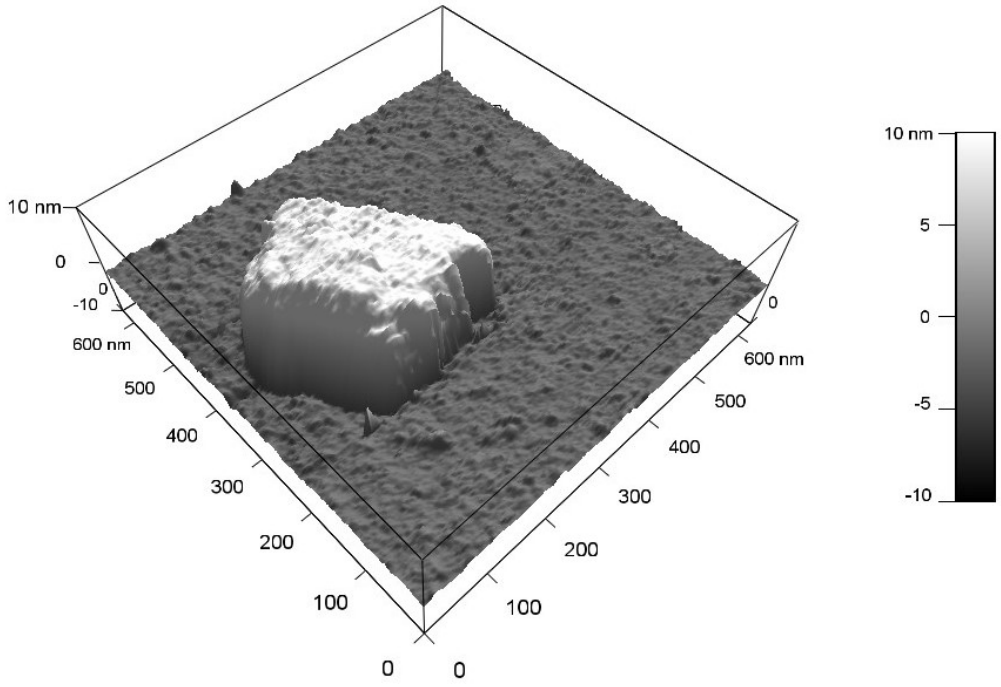

Figure 3.S15. The reaction mixture for Mg_2(dobdc) on mica after five minutes of growth displays some evidence of film formation nine nanometers in height. This concentration never appears to form any framework from solution.

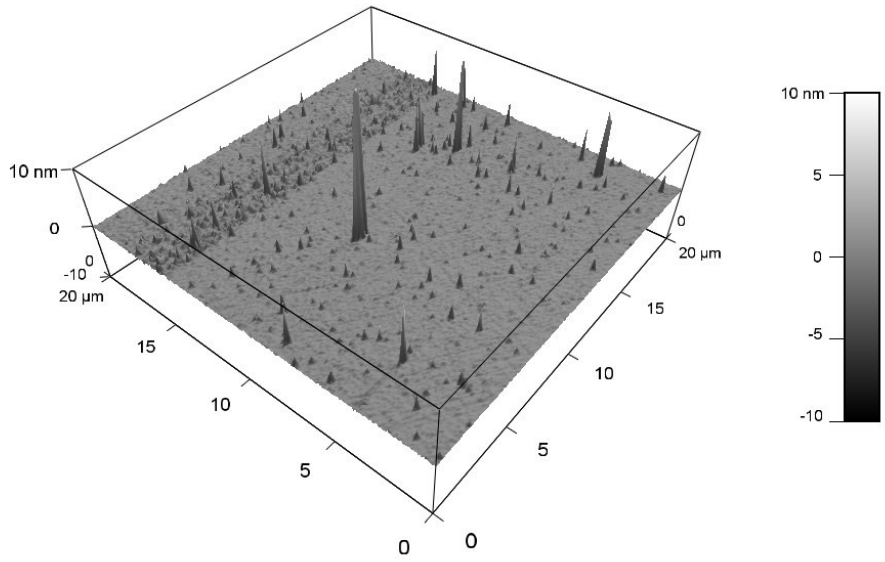

Figure 3.S16. Mg_2(dobdc) also displayed many (relatively small) peaks growing directly up from the surface, far more so than cobalt or zinc.

Chapter 4: Development and Application of a Zero-Length Chromatography System for Transport Diffusion Measurements

4.1 Introduction

The sorption kinetics and mass transport behavior of porous materials can be as important to their industrial application as their adsorption behavior at equilibrium.[1] The material structure and crystallite morphology and size distribution dictate the path length or set of path lengths that molecules must traverse within the adsorbent. In some cases, differing diffusivities of adsorbates or reactants can be used to play a strong role in selectivity.[2] However, this kinetic selectivity levies high transport resistances, which can cause processes to become impractically slow. The ideal material behavior optimizes both flux through the material and selectivity in separation or catalysis. However, as described in Chapter 1, the flux through a material or inherent adsorbate diffusion within an adsorbent is not necessarily identical to the measured apparent sorption kinetics. The measured process kinetics can be a function of several heat and mass transfer gradients.[3] Differentiating between them requires precise experiments which may test or eliminate these gradients separately. Only under these circumstances can one be confident that the quantity being measured is in fact an inherent (or effective) intracrystalline diffusivity.

One such discriminating technique to measure transport diffusion is zero-length column chromatography.[4] By using very small amounts of adsorbent in high-flow measurements, thermal gradients are negligible. Then, by changing the purge flow rate and gas type, the controlling resistance can be identified and quantified. While this is a simple experimental set-up in theory, effective instrument design must include careful handling of precise flow rate, valving effects that are negligible or do not interfere with desorption curves, and careful avoidance of the introduction of water for highly hydrophilic materials.

In Chapters 2 and 3, I have described methods of controlling the size and shape of M_2(dobdc) and M_2(dobpdc) in some cases across several orders of magnitude. This size control is in fact path length control within the crystallites. In this chapter, I detail work building, debugging, and using a novel zero-length column instrument designed and built within this lab for the purposes of diffusional measurements. Two case studies are presented: diffusion of CO_2 within Zn_2(dobdc) synthesized as described in Chapter 3 and diffusion of *m*-xylene within Co_2(dobdc) of differing aspect ratios, synthesized as described in Chapter 2. Both examples are designed to test transport properties of adsorbates involved in highly energy-intensive industrial separations within these size-controlled crystallites.[5]

4.2 Experimental Methods

General Procedures, Materials, and Reagents. All syntheses of M_2(dobdc) and M_2(dobpdc) are described in Chapters 2 and 3 of this work or below and referenced individually. Acetone, methanol, and hydrochloric acid were purchased commercially and used without further purification.

Solvothermal Synthesis of Co_2(dobdc). Single crystals of Co_2(dobdc) were synthesized using a slight modification to a previously published procedure.[6] A solution of H_4dobdc (74.3 mg, 0.375

mmol) in 2.5 mL of THF was added to a solution of $Co(CH_3COO)_2 \cdot 4H_2O$ (93.4 mg, 0.375 mmol) in 2.5 mL of deionized water in a PTFE-lined Parr-reactor. The reactor was placed in an oven that was preheated to 110 °C and kept at this temperature for 5 days to give pink needle-shaped single crystals. The crystals were soaked three times in 20 mL of DMF for 24 h at 120 °C, followed by soaking three times in 20 mL of methanol at 60 °C. Fully desolvated Co_2(dobdc) single crystals were obtained by heating at 180 °C under dynamic vacuum for 24 h.

Thermogravimetric Analysis Kinetics. Thermogravimetric Analysis (TGA) with CO2 uptake was done using a Q5000 Thermogravimetric Analyzer and TGA measurements involving propane were taken using a Discovery Series 5500 Thermogravimetric Analyzer from TA Instruments. For CO2 sorption kinetics on the bare framework, between 0.5 and 8 mg of sample were dropcast from methanol onto an aluminum TGA pan. For propane sorption kinetics on the bare framework, samples of Co_2(dobdc) were activated from methanol on a Schlenk line overnight and then left open to air for several hours. Leaving the samples open to air allowed for a consistent amount of MOF to be measured out onto each TGA pan, as each sample was found to have adsorbed the same amount of water. 5.00 mg of sample was placed on a TGA pan; when activated this procedure gave 3.40 ± 0.10mg of activated material. In order to minimize error associated with sample distribution each sample was evenly dispersed on the pan with three drops of methanol. Samples were activated on the TGA under a flow of nitrogen at 180 °C for two hours. After this initial activation, propane cycles were performed on each sample by first cooling to the target temperature (typically 40 °C), equilibrating for 5 minutes and then introducing a 2% stream of propane (balance nitrogen). After propane adsorption each sample was heated back to 180 °C under a flow of nitrogen for at least 30 minutes (the previous baseline from the initial activation was often achieved after 10 minutes). Purge gas flow rate was 20 mL/min.

Zero-Length Column Experiments. All samples are loaded in air into a custom-assembled ZLC cell (see Fig. 4.5) and activated in situ under flowing He for at least twelve hours. Samples as loaded are either methanol- or water-solvated. Insufficiently-activated metal–organic framework samples behave as if they have lower capacity (Section 4.10). Ultrahigh purity (99.999%) He and Ar were used as instrument purge gases for sample activation and desorption. High purity (99.99%) H_2 is used as a fuel source for the flame ionization detector (FID) and goes through a hydrocarbon removal column prior to reaching the detector. The adsorbates *m*-xylene and *p*-xylene were purchased from commercial sources, dried over 3 Å molecular sieves, and then stored over 3 Å molecular sieves in an N_2-filled glovebox. CO_2 equilibration used two different gas cylinders: 1.5% CO_2/98.5% N_2 and 4% CO_2/96% N_2, both commercially bought from Praxair. All gas cylinders (He, Ar, CO_2 mixture) go through a Restek Triple Gas Filter to remove trace oxygen, moisture, and hydrocarbons.

4.3 Results and Discussion

In Chapters 2 and 3 of this work, methods for controlling the size, shape, and dispersity of M_2(dobdc) and M_2(dobpdc) materials are described. Intuitively, this control should lead to measurable differences in intracrystalline diffusion, because size and shape control of these highly anisotropic materials correlates with control over path length. While the diffusivity itself for identical material composition should not change, the time constant of diffusion is related to the square of the path length. Elongating a one-dimensional structure in the pore direction results in longer pores, and thus longer path lengths. Control of the path length within porous materials can directly control the sorption kinetics: that is, the time scale associated with adsorption and/or

desorption within materials. However, examining the kinetics of a macroscopic sorption experiment is only under certain circumstances a probe of intracrystalline diffusion.

Thermogravimetric Analysis Sorption Kinetics. One initial set of tests demonstrating this convolution of mass transfer resistances was done using thermogravimetric analysis (TGA) as a technique to probe the kinetics of adsorption within Co_2(dobdc). These experiments did not work to uncover intracrystalline diffusion, but they are a useful case study in the concepts discussed and the motivation to build an instrument capable of discriminating between different mass transfer processes. The Co_2(dobdc) crystallites were synthesized using Reaction 2.3 to achieve multiple crystallite lengths (Fig. 4.1).

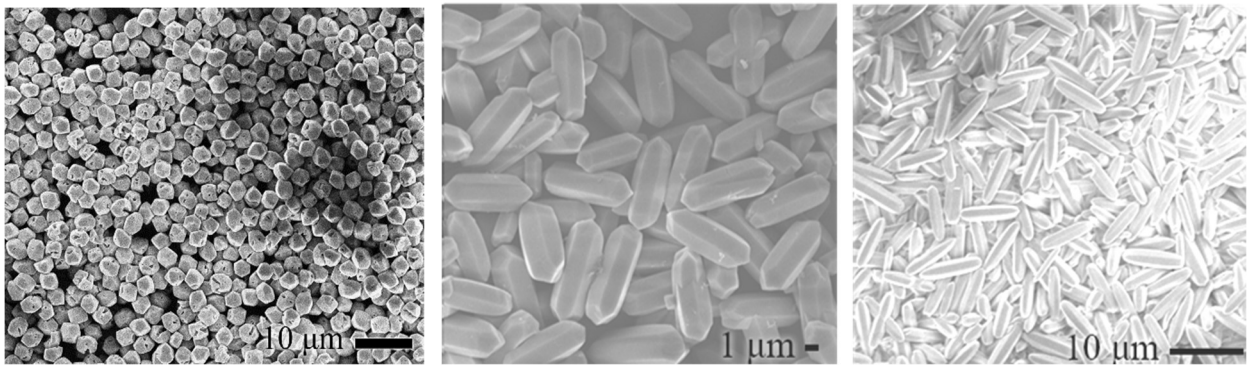

Figure 4.1. From left to right, Co_2(dobdc) crystallites synthesized from the $Co(CH_3COO)_2$, $Co(ClH_2CCOO)_2$, and $Co(Cl_3CCOO)_2$ precursors using Reaction 2.3 to create three sets of crystallites of varying path length.

Initial experiments probed the kinetics of CO_2 uptake by activation at introducing pure CO_2 at a given temperature and watching mass change; as CO_2 adsorbs, the mass of the sample will increase. In Figure 4.2, the kinetics of adsorption for the shortest path length sample is compared to that of the longest path length sample. Time zero is the time at which the gas stream was switched to CO_2 (see Section 4.2). To create this graph, the weight was normalized by the baseline activated weight. Additional weight, ascribed to CO_2, was then normalized to the amount of weight corresponding to one CO_2 molecule per open-metal site, called "Occupancy." No meaningful trend emerged: the aspect ratio in this case, for the temperatures probed, does not play a quantifiable role in sorption uptake. This can be due to several causes. First, CO_2 is a relatively small molecule and the pores of Co_2(dobdc) are around 1.2 nanometers in diameter. For fast-diffusing molecules, very large crystallites are required to be able to measure diffusion. It is likely that path length control across several microns does not control the overall kinetics for CO_2 uptake. Instead, much larger crystallites (at least tens to hundreds of microns) appear to be needed to measure diffusion. This work will be presented in the first ZLC case study for the zinc analogue.

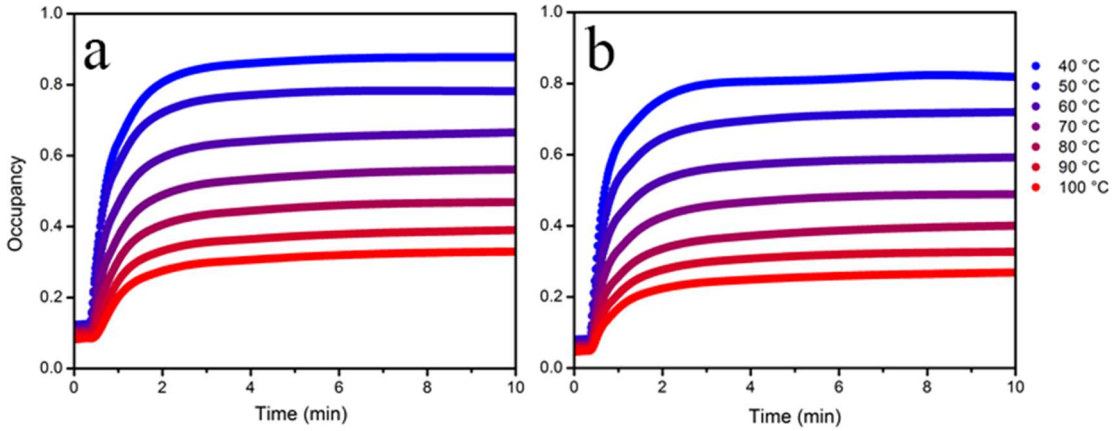

Figure 4.2. The kinetics of CO_2 adsorption for a. small aspect ratio crystallites and b. large aspect ratio crystallites.

The sample mass was found to be important in dictating the kinetic profile of CO_2 uptake: the same material at different masses could show different kinetic curves. This can be a sign of interparticle mass transfer resistance.[7] The lack of correlation displayed in Figure 4.2 between kinetics and intracrystalline path length typically means that some slower resistance controls the process. The overall kinetics are dictated by the overall mass transfer coefficient, which is the sum of the local resistances, such as intracrystalline diffusion, intercrystalline diffusion, or film resistance. Unless the intracrystalline diffusion is significantly slower than the other processes, the overall mass transfer resistance is a poor proxy.

From these experiments, it may be concluded that the intracrystalline diffusion is not slow enough to dictate the overall kinetics. For process design, this is an advantage. For the purpose of studying diffusion, however, this combination of technique/sorbent/sorbate is insufficient. One way to address this is to consider a slower-diffusing molecule. CO_2 has a fairly small kinetic diameter (330 pm), which is inversely related to gas-phase diffusion rate.[8,9] The same trend can hold within microporous materials.[10,11] Further experiments were run on a second TGA instrument with propane as a guest molecule (kinetic diameter 430 pm).

For the propane experiments, the same set of Co_2(dobdc) crystallites were used (Fig. 4.1). Sample masses were weighed out carefully using the microbalance of the TGA itself (See Section 4.2). The time derivative of propane uptake at 40 °C was compared across this series of crystallites. For these crystallites, at the same mass, the sorption kinetics curves overlay perfectly (Fig. 4.3). The only reproducible difference in kinetics arises when one of these samples is compared to a significantly larger crystallite (Fig. 4.4). Here a difference in kinetics arises on the tail end of uptake, attributable to adsorbate-adsorbate interactions as the pore fills. This slower uptake corresponds to an 8% lower total uptake during the half hour experiment, indicating that diffusivity may be measurable for crystallites approximately an order of magnitude larger in size.

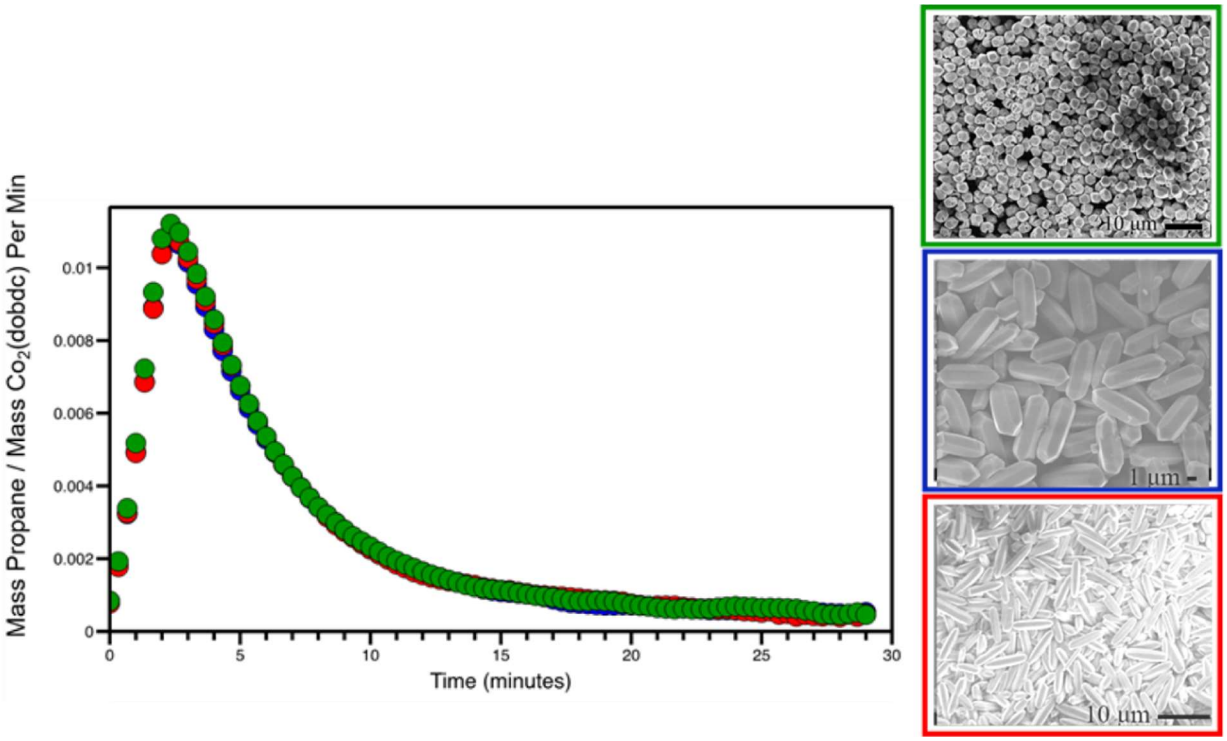

Figure 4.3. The propane uptake kinetics across a series of monodisperse Co_2(dobdc) crystallites yields essentially no difference in uptake kinetics, suggesting that intracrystalline diffusion is not the controlling mass transfer resistance under these conditions.

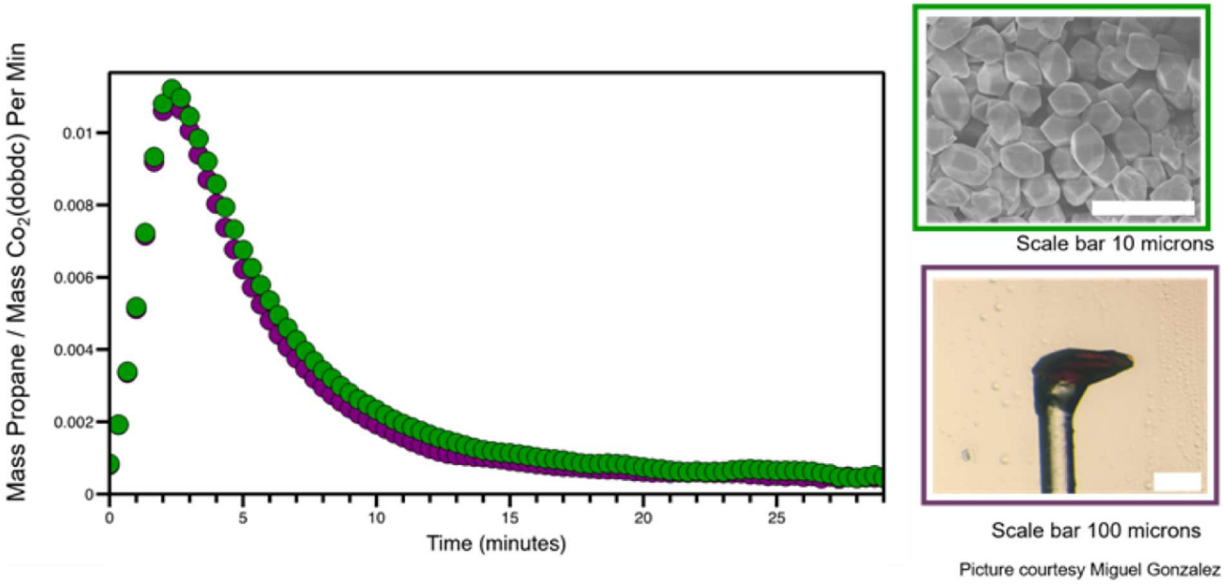

Figure 4.4. The hundred-micron sized Co_2(dobdc), synthesized solvothermally and displayed in purple, displayed the only reproducible kinetic limitation via this technique versus small Co_2(dobdc) crystallites, in green.

One additional note about using this technique to study porous materials, particularly those with open-metal sites, is that it is possible even for instruments that should be air-tight to have some water leakage. The Discovery 5500 TGA displayed some signs of water leakage during experiments. Water will displace many adsorbates of interest at open-metal sites.[6,12] Control tests temperature cycling under nitrogen displayed mass uptake too large to be accounted for by nitrogen uptake at 40 °C (Fig. 4.S1). Comparison with non-hydrophilic materials rules out system error. All experiments should have careful monitoring of possible inadvertent water exposure for these materials.

These experiments together suggest, first, that an even larger (and slower-diffusing) adsorbate is required to probe the differences in path length between the monodisperse samples of Co_2(dobdc). Second, studies of the diffusion of CO_2 within these frameworks should require crystallites of at least hundred-micron size path length, such as the Zn_2(dobdc) and Zn_2(dobpdc) samples synthesized in Chapter 3. Third, variables such as purge gas flow rate and sample mass could strongly affect the apparent kinetics. Even for the case of the large-crystal Co_2(dobdc), it is impossible to claim that the apparent kinetics are controlled in large part by the intracrystalline mass transfer. To be able to measure transport diffusivities, it is imperative to differentiate between different mechanisms of control in microporous materials. This led me to the conclusion that I needed to build a set-up capable of running measurements using a technique such as zero-length column chromatography (ZLC).

Adapting a Gas Chromatography Instrument for ZLC Measurements. Although the reader is directed to Chapter 1 for a full accounting of mass transfer resistances and the technique of zero-length column chromatography, a short review is provided here. The technique relies upon the use of step-changes in adsorbate pressure to very small amounts of adsorbent (<1 mg to ~ 15 mg). The minimization of adsorbent quantity, combined with high gas flow rates, maintains isothermal conditions within the cell, allowing for the elimination of heat effects. The step changes consist of a switching valve between a stream that contains adsorbate molecules and a purge stream. This is followed by a set of tests which can differentiate between different mass transfer resistances, including changes in flow rate, in purge gas, and in crystallite size. While the lab did not possess an instrument dedicated to these measurements, I saw that the operation of a gas chromatograph could be repurposed to act in a similar manner. The design, successes and challenges of this strategy, denoted as ZLC-Gen. 1, follow.

Included among the advantages of using this strategy of converting a gas chromatograph instrument is that it is a non-destructive use of pre-existing equipment that many labs already possess. Dedicated instruments for ZLC measurements, on the other hand, are rare. Using these tools may make the technique more accessible to the wider porous materials community. Typical gas chromatographs operate by injecting a sample to be analyzed into an inert gas stream, also known as the carrier gas.[13] Typical carrier gases are helium or nitrogen. The stream then traverses columns packed with material that can interact with various compounds within the sample differently, causing them to have different traversal times. These samples (after components have been separated) are then fed to a detector. Two typical detectors are thermal conductivity detectors (TCD) and flame ionization detectors (FID). The TCD senses changes in the thermal conductivity of the stream and compares it to a reference stream. The FID, on the other hand, is based off the generation and detection of ions during combustion of organic compounds. In general, FIDs have higher precision and lower detection limits but can only detect combustible materials. While the TCD has lower precision, it is a universal detector. The gas chromatograph adapted here has both in series.

The gas chromatography instrument has an inlet feed of helium and a sample loop, the latter of which I manipulated to monitor the desorption behavior of two industrially important molecules, CO_2 and *p*-xylene. While ZLC instruments typically use mass flow controllers to control the flow rate of the stream, the gas chromatograph instead relies upon a measured pressure set-point. A restricting column was added as a capillary flow-restrictor to the helium line to maintain appropriate flow rates. To measure initial CO_2 kinetics, a T-junction was added to the sample loop attaching a CO_2 cylinder. The basic operation is thus switching between the sample loop, which has a mixture of He/CO_2, and the pure He stream. During equilibration, the sample saturates with CO_2 molecules. During desorption, the stream switches to pure He, and the resultant stream concentration of CO_2 is observed. The cell itself contains 0.3 mg to 5 mg of MOF sandwiched between two stainless steel frits within a 1/16" Swagelok fitting (Fig. 4.5). The outlet of this cell leads directly to the TCD inlet, which is connected to the FID inlet.

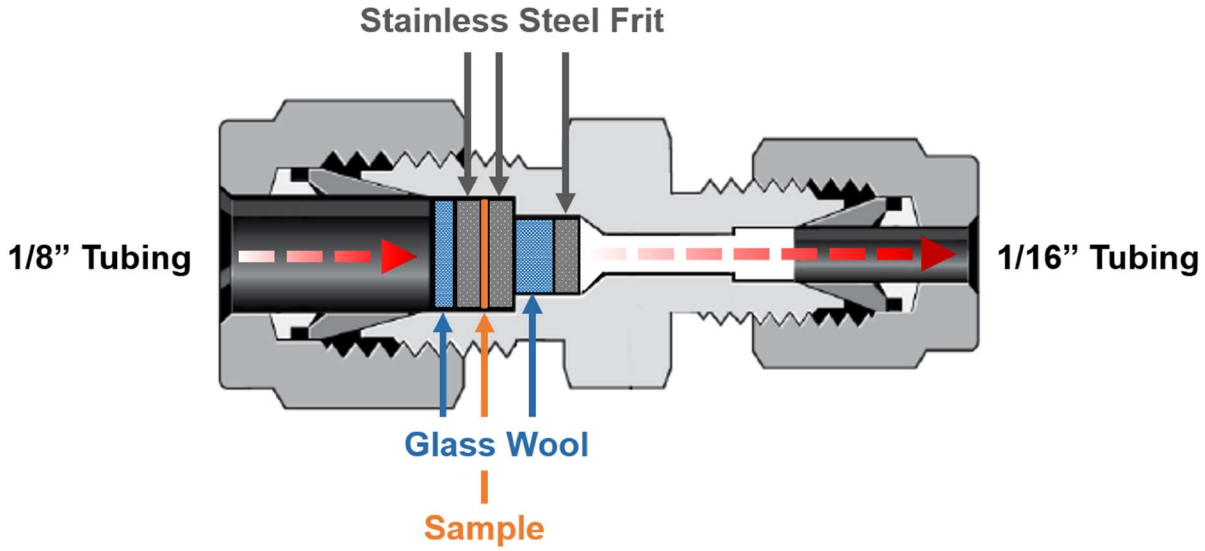

Figure 4.5. The ZLC cell contains a small amount of sample in between porous sinter disks. Glass wool holds the disks and sample in place and prevents sample from leaving the cell.

CO_2 Desorption Using ZLC-Gen. 1. Initial tests were run with CO_2 as an adsorbate on large Co_2(dobdc) crystallites (150 microns in length), synthesized solvothermally. As CO_2 is not combustible, the TCD must be used on this instrument. An example of a blank cell response is displayed in Fig. 4.S2. The baseline concentration of CO_2 is noisy. Nonetheless, the baseline signal while CO_2 is flowing through the cell may be averaged for our c_0 value. With a linear response factor for the detector and a given adsorbate, the voltage given by the detector is linearly related to the concentration in the stream, and the plot may then be converted to one of stream concentration c normalized to initial concentration c_0. The blank cell drops in signal faster, as to be expected, since it does not have the capacitance of the MOF (Fig. 4.6).

The first test is to vary the flow rate at the same temperature for the same sample. This leads to different values of the controlling nondimensional parameter, also known as the washout parameter, L, which is a ratio of sorption equilibrium factors to sorption kinetic factors. See Chapter 1 for more details.

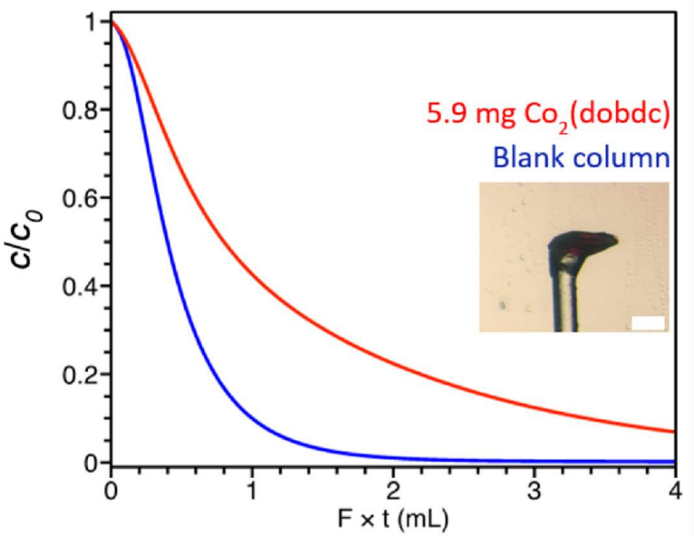

Figure 4.6. The desorption curves plotted as c/c_0 versus total flow in mL shows signal delay for the MOF. Scale bar on inset SEM micrograph is 100 microns.

The desorption kinetics for CO_2 with the Co_2(dobdc) sample were captured at a flow rate of 10 mL/min and 20 mL/min. The data were collected three times per desorption run, and these three runs were averaged together. For an equilibrium-controlled process, the curves should overlay when plotted as a function of F, flow rate, times t, time. Instead, Fig. 4.S3 displays kinetic control. The curve for the faster flow rate drops more steeply at the beginning but then levels to a more shallow slope, consistent with a kinetically-controlled mass balance.

However, the use of a T-junction to bleed in CO_2 led to some control problems in amount of CO_2. One fundamental difficulty with converting a gas chromatograph instrument is that it only has one gas inlet. For gaseous adsorbates, the experiment requires switching between two gas streams. As referenced in Chapter 1, it is easiest to run ZLC experiments within the linear section of the isotherm, where amount adsorbed at equilibrium is linearly proportional to the partial pressure of the gas.

With the equipment available, I was only able to decrease the concentration of CO_2 to be about 30% of the stream when joined at the sample loop to the helium stream, because the CO_2 pressure needed to be high enough to prevent back-diffusion of helium to the CO_2 cylinder. An alternate solution would be to use a cylinder with a lower partial pressure of CO_2, as done in subsequent sections. However, the sample junction is isolated when helium is not passing through it, leading to sample loop pressurization. The second-generation instrument has separate mass flow controllers for the adsorbate stream, avoiding this problem.

Adapting for Vapor-Phase Adsorbates. Initial experiments with the kinetics of xylene sorption on Co_2(dobdc) were also conducted using this instrument. As xylenes are liquid at room temperature, the introduction of xylenes to the sample is accomplished using a bubbler. The purge gas stream flows through and equilibrates with the liquid xylenes, generating a saturated stream. During desorption, the stream instead bypasses the bubbler. A general schematic of this operation is displayed in Figure 4.8. This is thus a second mode of operation, where the only gas cylinder used is the purge gas. I chose to study xylenes for several reasons: first, that the separation itself is of significant interest to the separations community, as the global energy cost of separating the isomers is high; second, that the material Co_2(dobdc) has been suggested for the separation of *p*-

xylene, *m*-xylene, *o*-xylene, and ethylbenzene; and third, that the molecules are relatively bulky, which should result in slower intracrystalline diffusivity. More information on this will be given in the second case study presented in this chapter.

For these experiments, the T-junction was removed from the sample loop and a bubbler containing the xylene adsorbate of interest (see Section 4.2) was introduced. The line is purged prior to attachment, so that the adsorbate liquid is kept air- and water-free. The sample loop is also kept under static pressure during desorption, but there is little noticeable change in pressure at the beginning of the equilibration section.

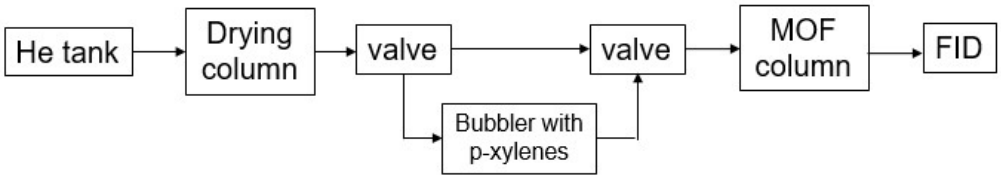

Figure 4.7. A schematic of vapor-phase sorption kinetics experiments, with *p*-xylene as an example adsorbate.

Detector Saturation. Regardless of the specific detector chosen, each method detects compounds based on a chemical or physical property of the sample. The response is an amplified electrical signal, which is then digitized and stored. Each detector has some normal range of setpoint variables and physical characteristics within which operation is normal. When some parameters fall outside of the typical usage, the detector can become saturated. In this case, the increase in signal as a function of increasing amount of analyte is less than expected. For an FID, detector saturation generally arises from incomplete combustion: the flame is no longer able to burn the large amount of analyte which passes through it.[13] The detectors generally sample at a fixed rate (in this case, 5 Hz). Higher flow rates have larger amounts of analyte passing through per amount of time and in some cases can lead to detector saturation. Figure 4.8 has a cartoon example of this case. Since all flow rates are sampled at the same frequency, the faster flow rates have higher signal. In the case of detector saturation, this can lead to false kinetic curves, beginning from a lower value with later onset of desorption.

Care must be taken to look for signs of this instrument limit: at the beginning of saturation, the voltage is no longer proportional to the flow rate. Further, at very high flow rates, the instrument background noise can change and appear to be non-physically low. That is, the level of background noise during equilibration will appear to approach zero.

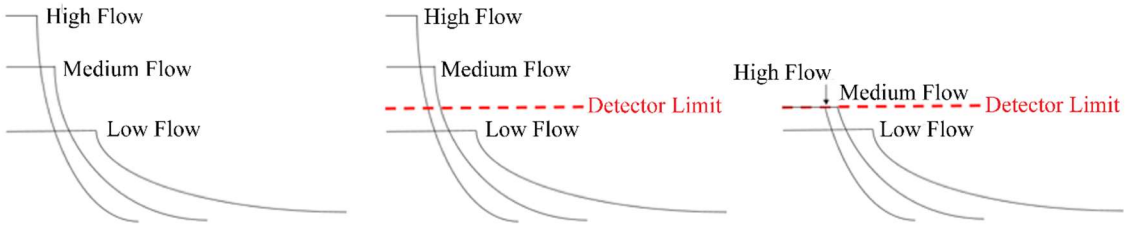

Figure 4.8. At left, illustrative cartoon desorption curves (faster flow rate has faster overall desorption). The middle diagram shows an overlaid detection limit. At far right, this detection limit has truncated the curves corresponding to fast and medium flow rates, changing their apparent kinetics.

Water-Scavenging and Material Compatibility. The initial bubbler design included Viton® o-rings, which are not compatible with xylenes. The o-rings gradually failed and introduced water and air, the former of which will compete with the desired adsorbate at the open-metal sites. The use of Kalrez® o-rings is required for experiments with xylenes. In general, material compatibility requirements must be met, including the valving and tubing. The ZLC-Gen 1 contains stainless steel and bronze components. Prior to usage, chemical compatibility should be checked for any desired sample.

Normal gas chromatography instruments have columns designed to separate components of the effluent stream such that they can be detected separately. From deliberate design, the only column present is that of the zero-length MOF column. If a stream has two components, such as water and *p*-xylene, a universal detector such as a TCD will read the fraction-averaged thermal conductivity of the stream. The FID, being unable to combust water, will only detect the xylene. The presence of water is not obvious in such a configuration.

Water leakage was detected by running multiple adsorption-desorption cycles on the same material without activation: at one temperature, switching between helium + xylene to pure helium. For a plot of concentration versus time, the area under the curve may be integrated to yield total concentration on the material, which corresponds to material capacity.[14] Over time, for no material change, the curves should overlay exactly. Instead, in this configuration, the curves were shifting down, indicating similar kinetics but a loss in capacity (Fig. 4.9). This is how the water-leakage through the o-ring was detected. Two solutions were developed: first, to replace the failing o-rings; second, to add in 4 Å molecular sieves into the bubbler. These are materials with pores large enough to allow water uptake but small enough that xylene molecules will not be able to penetrate. All bubbler configurations now adopt both these settings.

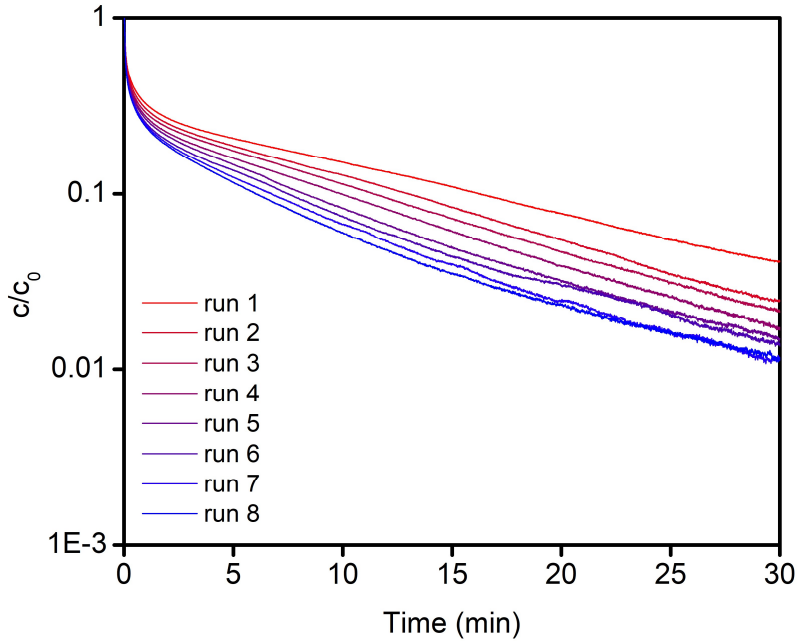

Figure 4.9. Subsequent adsorption/desorption cycles at the same temperature display a loss of material capacity over time. With better o-rings and water-scavenging sieves in the bubbler, the curves overlay perfectly.

Development and Design of ZLC-Gen. 2. Despite these advancements, several factors spurred the development of a dedicated instrument for the technique. Controlling the flow rate for ZLC-Gen. 1 was accomplished through changing a pressure set-point on the instrument. However, even the instrument specifications only promised a steady flow rate within 5%. Figure 4.S4 displays an example of non-overlaying runs arising from an apparent variation of the flow rate during equilibration. Indeed, using a flowmeter to measure the flow rate at set points, it was found to be inconsistent within about 5%. Instead of using a pressure set-point, dedicated mass flow controllers should be used to control the stream flow rate. For gas phase measurements, the instrument needs two gas inlets.

Further, CO_2 is an adsorbate of considerable interest to our lab. As it cannot be combusted, only the TCD may be used to detect it. However, the TCD has a significantly higher detection limit than the FID does: the lower limit for the TCD is around 100–300 ppm, while the FID can detect molecules at 0.5 ppm. This is quite a disadvantage, as traditional ZLC analysis uses the lower concentration section of the graph to glean diffusion constants (see Chapter 1 for more details).

Any future work on kinetics in materials for direct air capture of CO_2 would be best done with high resolution at hundreds of ppm down to two to three orders of magnitude lower. Another option would be to include a mass-spectrometer as a detection tool, which has its own advantages. However, including a mass spectrometer would nearly double the cost of the instrument. Instead, I decided on an FID that included a methanizer unit. The flame ionization detector is preceded by a hydrogenating reactor, which converts CO_2 and CO into methane. This lowers the concentration detectable by at least two orders of magnitude and enables study on materials designed for direct air capture of CO_2.

Finally, it is standard practice to compare the response of a blank column to that of the sample adsorbent column. The last improvement made to instrument design at this point was to include the ability to switch between two different columns, i.e. one blank and one sample column, for easier trouble-shooting and analysis. A schematic of the instrument as-designed is in Figure 4.10.

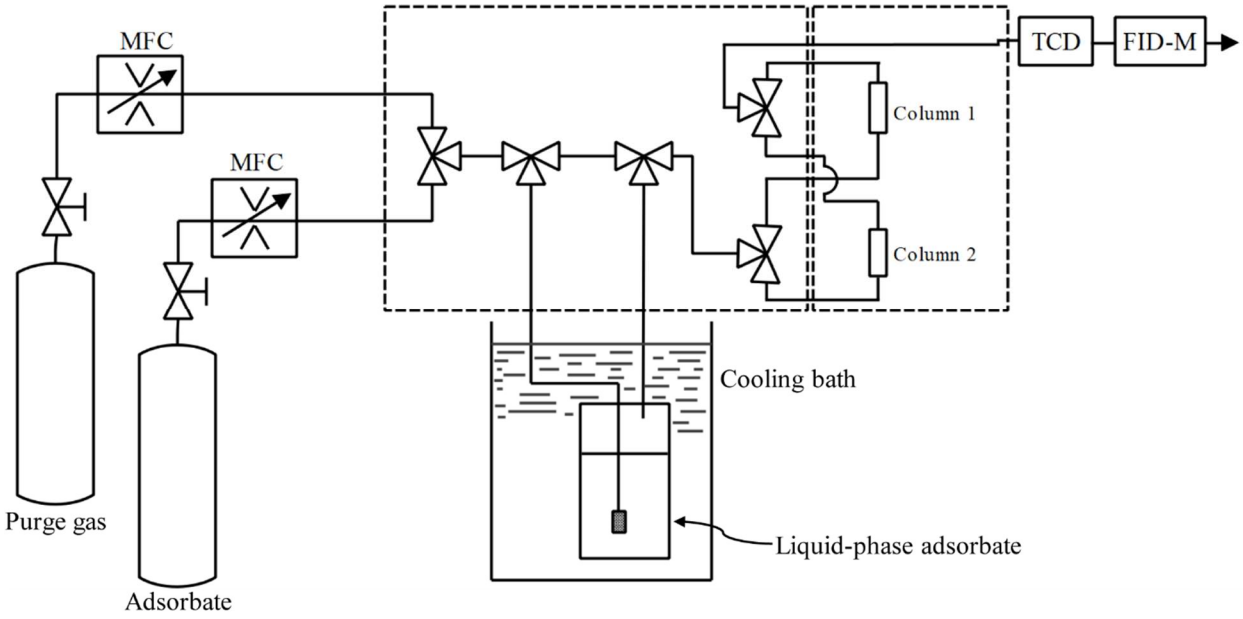

Figure 4.10. The ZLC-Gen. 2 as designed. Both gas cylinders are controlled by mass flow controllers. The stream may be directed through a bubbler or directed around it. At any time, the flow will go through either Column 1 or Column 2.

Of note, the liquid phase adsorbate may also be used to add a co-adsorbate, if desired, such as water. Carbon capture under humid conditions is one example of an experiment that could benefit from this configuration.

Thermal Equilibration in ZLC-Gen. 2. A final description of design criteria corresponding to stream thermal equilibration for this instrument is described in this section. Each dashed line in Figure 4.11 denotes a separate oven which may be heated up to 220 °C. The helium cylinder sits at room temperature. The xylenes bubbler is contained within a cooling (or heating) bath. By controlling the temperature of the bath, the vapor-liquid equilibrium of the gas/liquid mixture is controlled. The vapor pressure of a liquid is the equilibrium pressure of the vapor above the liquid: that is, the pressure of the vapor resulting from evaporation of a liquid above the liquid in a closed container. As temperature increases, the vapor pressure increases. This is a convenient way to control stream concentration of an adsorbate if and only if the desired concentration is accessible, the temperature may be controlled well, and the stream can be fully equilibrated.

Although initial experiments began with *p*-xylene, its liquid characteristics are non-ideal for these experiments. As discussed in Chapter 1, it is often helpful to run desorption kinetics experiments with a low initial concentration: ideally, within the linear region of the isotherm for a given material, adsorbate, and temperature. Examination of the material isotherm allows a range of vapor pressures at which the amount of adsorbate on the surface should be linearly related to the vapor pressure. For effective use of a bubbler, this vapor pressure should correspond to a temperature range that is easily held steady. For materials with relatively weak adsorption, this is an easy criterion to meet, as the linear region of the isotherm encompasses a large range of vapor pressures. However, for open-metal site containing framework, the heat of adsorption can be quite strong, leading to a small linear region at low pressures.

For the case of *p*-xylene, the liquid freezes at 13 °C. The vapor pressure of this liquid at room temperature, about 13 mbar, is well above saturation for the framework. A similar adsorbate with

better physical characteristics for these purposes is *m*-xylene, which has a freezing point of −48 °C. The minimum vapor pressure readily achievable for *m*-xylene is correspondingly much lower than that of *p*-xylene, and a large range of vapor pressures may be held at temperature more easily without freezing. The lowest temperature baths attempted were obtained using ethylene glycol/ethanol dry ice baths to reach temperatures of −45 °C to −40 °C. Given the gas inlet is at room temperature and the sample columns are within an oven at 140 °C, the intermediate diversion to a -40 C liquid requires two subsequent temperature swings.

As originally built, the thermal equilibration tubing present did not allow enough heat transfer area. Figure 4.11 contains the results of a desorption experiment before fixing thermal equilibration. The conditions included a -42 °C ethylene glycol/ethanol dry ice bath, intended to saturate the helium stream with a very small amount of m-xylene, such that the experiment stays within the linear regime of the isotherm during equilibration and desorption. The problem with this lack of thermal equilibration is only obvious by careful examination of the very low concentration (10^{-5} of the original concentration) region. Clearly, the data goes to a minimum and then increases. Under proper conditions, this should never happen: at desorption, the instrument switches to pure purge gas, and the concentration should only decrease as the adsorbate is flushed out of the system. The results of this experiment indicate that the concentration of adsorbate is increasing as purge gas flows out.

This errant concentration increase arises from insufficient stream heating from -42°C to 140 °C before coming out of the bubbler loop in Figure 4.10. The stream then cooled the apparatus itself, allowing for additional xylene adsorption within the instrument. As the instrument tubing heats up during the desorption instrument, when the stream bypasses the cooling bath, additional xylene concentration slowly comes from the instrument heating up. It is of rather low concentration, 10^{-6} to 10^{-5} of the original signal voltage, but most diffusional information for kinetic experiments is contained in the long-time asymptote that covers this range. This problem was solved through the addition of extra thermal equilibration columns before and after the cooling bath originally depicted in Figure 4.10, allowing a flat baseline post-desorption (Fig. 4.11). The final configuration of the instrument, in Figure 4.12, allows for reproducible desorption kinetics with either gas-phase or vapor-phase adsorbates.

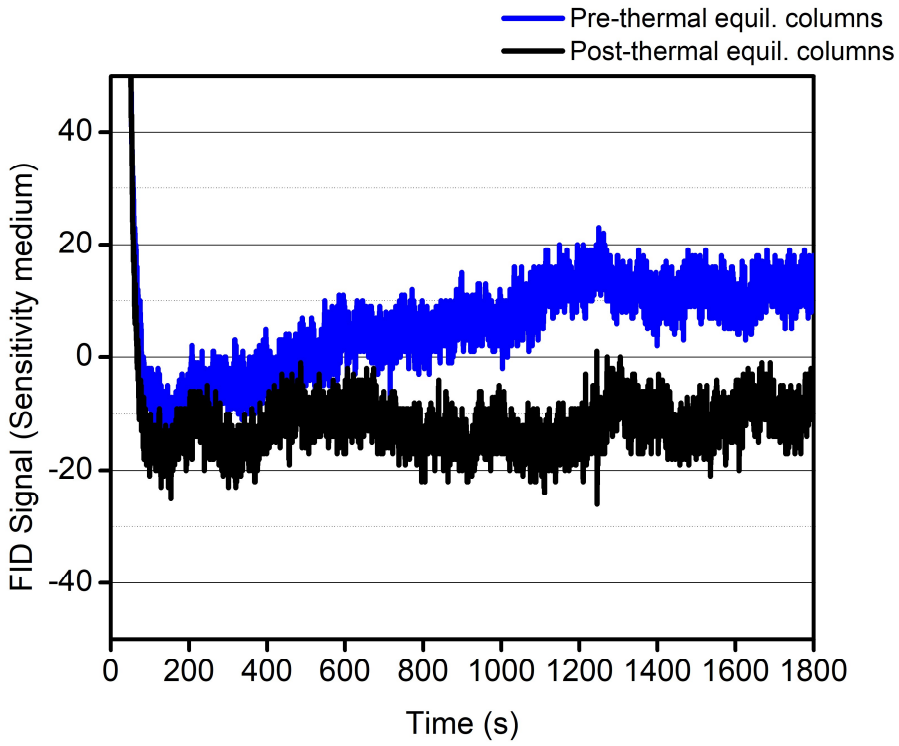

Figure 4.11. Before adding thermal equilibration, the signal gradually rises over time; after adding thermal equilibration columns, the signal remains flat.

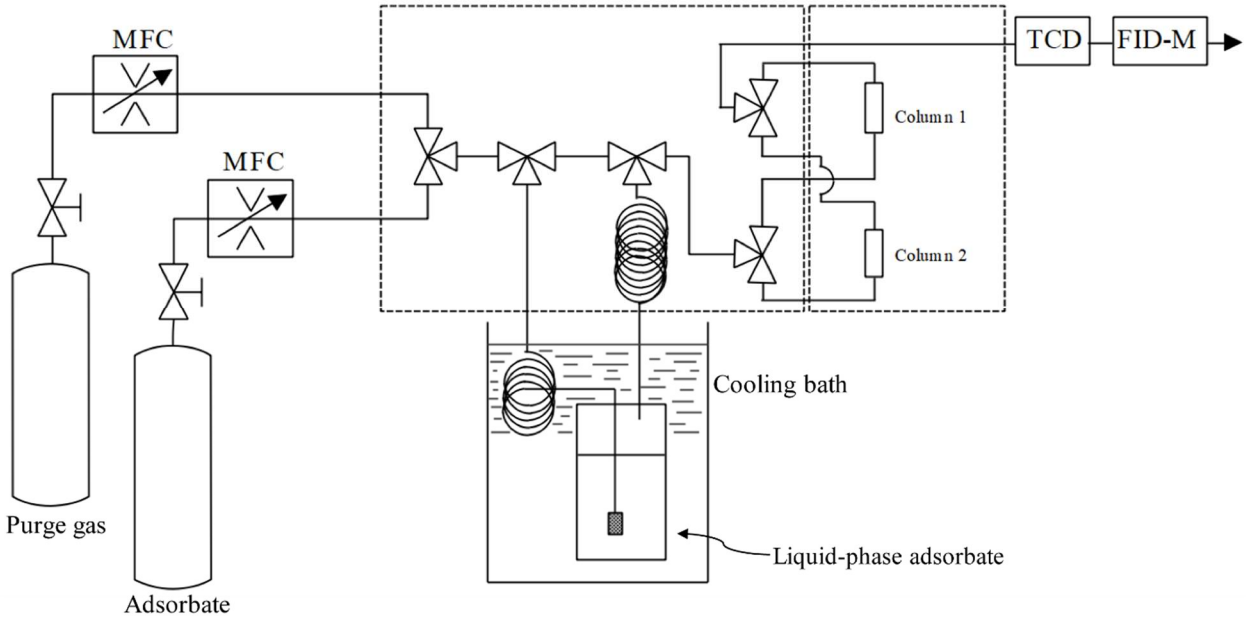

Figure 4.12. The final ZLC-Gen. 2 design includes the ability to switch between two gas columns, both controlled by mass flow controllers. The stream may go through the bubbler or bypass. A six-foot column is included for thermal

equilibration pre-bubbler and two columns bring the temperature back up to oven temperature for equilibration and desorption.

Case Study 1: CO_2 Transport Diffusion in Zn_2(dobdc). Metal–organic frameworks have been heavily studied as potential energy-efficient adsorbents for carbon dioxide capture from post-combustion processes. The M_2(dobdc) and M_2(dobpdc) family of materials have been studied extensively as CO_2-selective materials for CO_2/N_2 separations. However, little is known about gas diffusion within these materials. Previous PFG-NMR studies on the behavior of CO_2 within the expanded-pore Zn_2(dobpdc) suggested high diffusion anisotropy within the material. At 1 bar CO_2, the diffusivity along the pore direction was measured to be around 6×10^{-9} m^2/s and diffusivity perpendicular to the pore was measured to be around 4×10^{-11} m^2/s.[15,16] This non-zero diffusivity through the pore walls was attributed to the presence of defects.

The measurement of these materials using ZLC is of interest for several reasons. For one, ZLC measurements probe transport diffusion across the entire sample in the cell. This is diffusion in response to a concentration gradient, as at time zero the environment surrounding the crystals changes from the equilibration stream to a purge stream containing no adsorbate. While the self-diffusivity can be equal to the transport diffusion, this is not necessarily true. Indeed, in measurements of zeolite diffusion, different methods of measuring diffusion have led to dramatically different values measured. In general, different techniques lead to a trend in diffusivity measured, where macroscopic uptake methods (gravimetric or volumetric) lead to particularly low estimates of diffusivity, while PFG-NMR can be up to five orders of magnitude higher in diffusivity. This is an incredible spread of values. Diffusivities measured using ZLC, which is a macroscopic method, tend to be higher than the larger-scale gravimetric or volumetric measurement but are still often lower than the PFG-NMR values. Diffusion in MOFs using ZLC has not yet been reported, as the technique has instead measured the materials at equilibrium, not under kinetic control. This presents a unique opportunity to compare transport and self-diffusion. Using the zinc analogue of M_2(dobdc) or M_2(dobpdc) allows for facile comparison to PFG-NMR, as the metal cations are diamagnetic.

Notably, very large crystals needed to be synthesized for either PFG-NMR or ZLC measurements. This was accomplished through using control over surfaces described in Chapter 3, leading to crystals up to 700 microns in length (Fig. 4.13). These are the largest crystals reported for Zn_2(dobdc). PFG-NMR experiments run by a collaborator, Dr. Alex Forse, yielded highly anisotropic self-diffusivities near 1 bar. The diffusivity along the pore direction ($D_\parallel$) for CO_2 within Zn_2(dobdc) is 1×10^{-9} m^2/s, while the diffusivity perpendicular to the pore direction was lower than instrument limits. The resulting diffusion anisotropy ($D_\parallel/D_\perp$) is at least 10,000, indicating that diffusion is overwhelmingly one-dimensional along the pores.

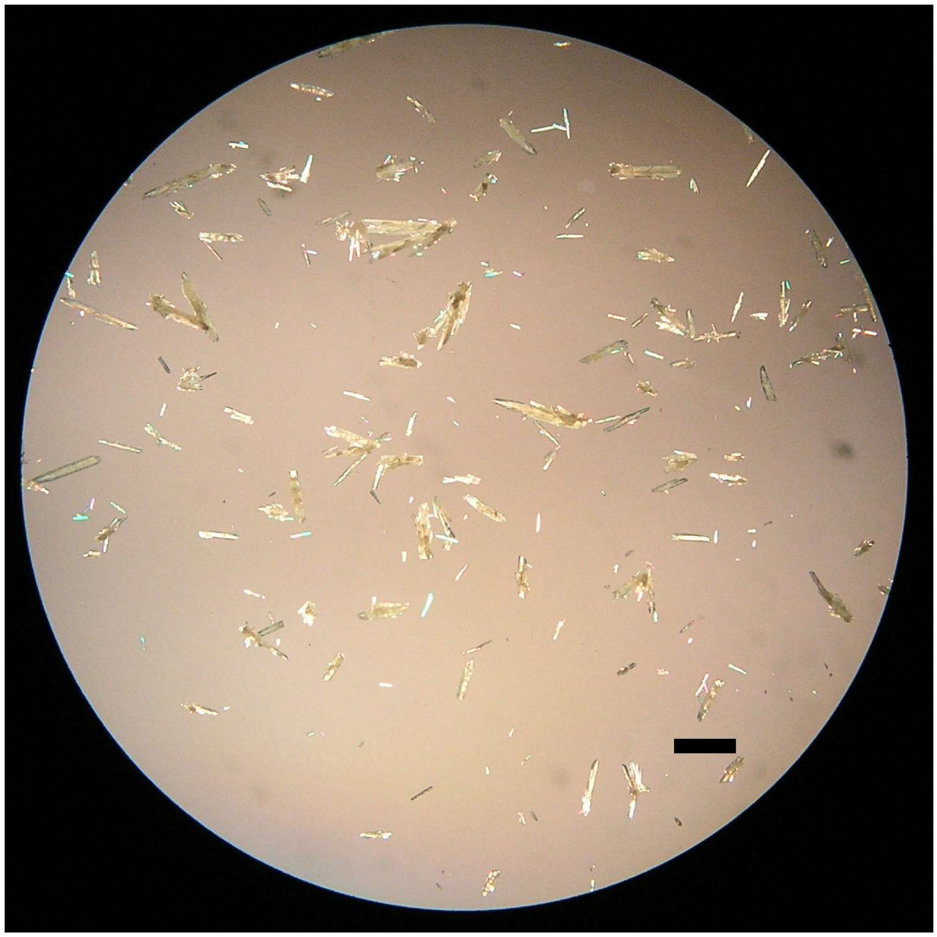

Figure 4.13. Optical microscope image of Zn_2(dobdc) synthesized using Reaction 3.1. Scale bar is 500 microns.

The same set of crystallites (post PFG-NMR) were used to measure diffusion using zero-length column chromatography. For these measurements, about 1 mg of the material was placed into the cell and activated at 180 °C for twelve hours. The adsorbate stream was 4% CO_2/96% N_2. High flow rates were chosen (20 mL/min versus 40 mL/min) to maximize the controlling non-dimensional parameter L and achieve kinetic control (see Chapter 1). The experiment temperature was 30 °C, as lower temperatures could not be controlled well within the oven. As expected, the overall desorption is faster at the higher flow rate (Fig. 4.S5). The simple graphical check of plotting concentration versus flow rate multiplied by time $(F \times t)$[14] was employed to differentiate between kinetic and equilibrium measurements (Fig. 4.14). This plot clearly indicates that Zn_2(dobdc) is under diffusive control, as the curves cross and the higher flow rate has an asymptotic tail characteristic of diffusion.

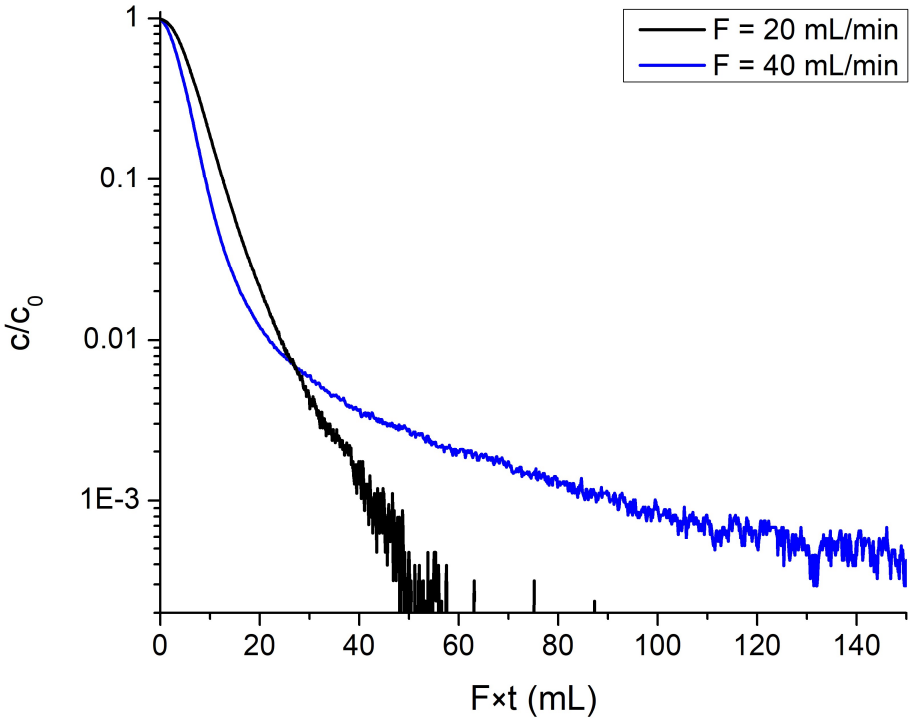

Figure 4.14. The F×t plot clearly displays the crossover behavior indicative of kinetic control at high flow rates for CO_2 within large crystallites of Zn_2(dobdc).

These desorption curves may then be used to calculate diffusivity. The cell is very close to the detector and resulting pressure drop after the cell has been minimized, so the pressure within the cell may be well-approximated as 1 bar.[17] The equilibrium pressure of CO_2 is within the linear part of the CO_2 isotherm at 30 °C.[18] Extracting CO_2 diffusivity from these plots was done using a version of the long-time asymptote technique using an experimentally-measured crystal size distribution and assuming one-dimensional diffusion. As displayed in Figure 4.14, the crystal size ranges from a few microns to hundreds of microns. Because the time constant is related to l^2/D, a range of crystal lengths leads to a range of time constants, which imparts curvature to the long-time asymptote.[19,20] Failing to include this leads to underestimation of the diffusivity.[20]

Similarly, one-dimensional diffusion is used rather than spherical diffusion as PFG-NMR indicates that diffusion is essentially one-dimensional. While previous studies on equilibrium in M_2(dobdc) have used the concept of the effective spherical diameter to be able to apply three-dimensional spherical diffusion equations,[17] the crystals used here are much larger and under diffusional control. As one-dimensional diffusion and spherical diffusion deviate in the long-time asymptote, using an effective sphere would introduce some avoidable error into this analysis.[21]

Simultaneous regression was used on both curves to minimize the mean-squared error of fits to the long-time asymptotic region, including nine different size fractions (Table 4.1) ranging from 390 microns to 10 microns in characteristic length (the characteristic length is the half-length of the crystallite, following the model of one-dimensional slab diffusion[22]). These size fractions are weighted by volume, determined experimentally by measuring crystal size and width across as set of 650 crystallites and calculating approximate cylindrical volume. Each individual small crystallite contributes significantly less than the very large crystallites, which contain the bulk of

the diffusive lengths. The size fractions are defined by the longest length represented, following normal crystal size distribution handling.[20]

Table 4.1. List of path lengths and corresponding volume fractions in Zn_2(dobdc) crystallites used for zero-length column CO_2 diffusion measurements.

Characteristic path length (μm)	Volume fraction
390	0.1
340	0.2
290	0.1
265	0.1
210	0.1
190	0.1
170	0.1
140	0.1
108	0.1

The best fit to the simultaneous regression is a diffusivity of 7×10^{-11} m^2/s, which is about an order of magnitude and a half lower than that measured for the exact same crystallites using PFG-NMR. The highest flow rate overlaid with the fit is displayed in Figure 4.15. This is both intriguing and in line with previous experimental results for zeolites. The effective transport diffusivity here is lower than the self-diffusivity measured at higher pressures. Since the isotherm is linear in this region, the Darken equation predicts a constant diffusivity,[23] so the discrepancy is not predicted by thermodynamics. It is extremely unlikely that this arises from heat effects at such a small amount of adsorbate and such high flow rates. I must therefore conclude that I am measuring the effect of additional mass transfer resistances relative to the PFG-NMR measurements.

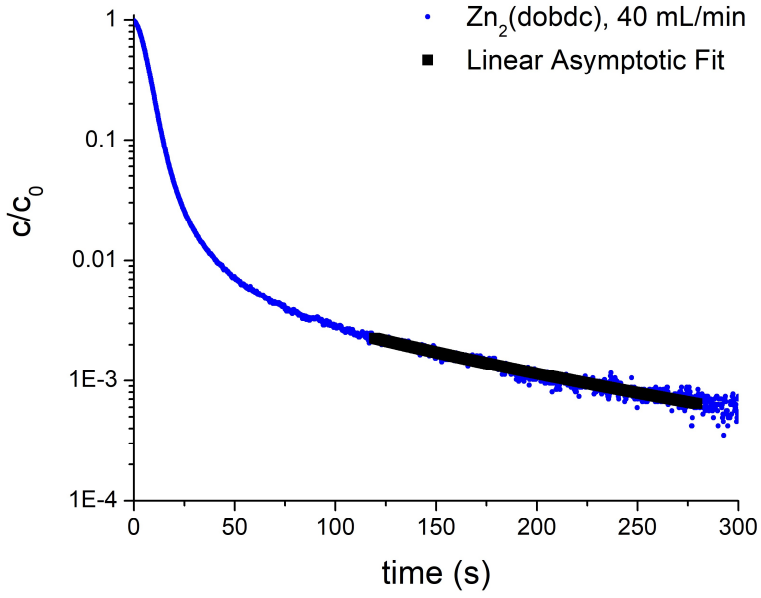

Figure 4.15. The highest flow rate desorption curve overlaid by the linear fit to the asymptote with calculated diffusivity.

The diffusion times used for the PFG-NMR analysis were 40 ms; the root mean square displacements measured using the Einstein equation were therefore about 9 microns, assuming the measured diffusivity of 1×10^{-9} m^2/s. This is significantly smaller than the average volume-weighted crystallite length, indicating that self-diffusion within the crystallite was probed, but surface effects were likely largely avoided on this length scale. However, the measurement of transport diffusion using ZLC necessarily arises from the entire length of the crystallite across the entire sample. It is likely that the additional barriers arise from defects, crystalline fault planes, and surface barriers. One-dimensional pores are particularly susceptible to these barriers, as any pore blockage can significantly hinder diffusion and/or material capacity. Because these crystallites were also used for PFG-NMR, they have undergone extensive handling and air transport. Future work should be done to determine if the defects are native or introduced through handling. In addition, it is imperative to study the effects of different crystallization conditions to minimize these barriers for optimal material performance.

Case Study 2: *m*-Xylene Transport Diffusion in Co_2(dobdc). I also used ZLC to examine the effect of changing the path length within Co_2(dobdc). Using different anions as described in Chapter 2, the aspect ratio can be tuned from short to moderate aspect ratio crystallites. These Co_2(dobdc) crystallites vary in path length from less than a micron to ten microns. Measuring diffusion along these shorter path lengths requires correspondingly lower diffusivity. One way to accomplish this is by choosing a larger adsorbate. One particularly interesting set of molecules for study is the C_8 isomers *o*-xylene, *m*-xylene, *p*-xylene, and ethylbenzene (Table 4.2). While these isomers are produced as a mixture through reformates or pyrolysis, industrial demand is far higher for some isomers than others.[24] The combined energy cost of separating benzene and its related derivatives adds up to about 50 GW per year.[5] It is thus of great interest to find materials which can be used in less energy-intensive processes, such as adsorbents.

One such material demonstrating the ability to distinguish between all four C_8 isomers of interest is Co_2(dobdc).[25] Each molecule has a different amount of interaction with the framework, and this differentiation can be used to fractionate a mixture of C_8 xylenes. In fact, several of the isomers can interact with multiple metal sites at once, leading to particularly strong binding within the framework. As listed in Table 4.2, all four C_8 isomers have significantly higher kinetic diameter than CO_2. This is expected to lead to slower diffusion within the pores of M_2(dobdc). Thus, xylenes presented an intriguing goal for demonstrating successful path length control within Co_2(dobdc).

Table 4.2. Selected physical properties of the C_8 alkylaromatics[24,26]

C_8 isomer	boiling point (°C)	kinetic diameter (Å)	melting point (°C)
o-xylene	144.4	6.8	−25
m-xylene	139.1	6.8	−48
p-xylene	138.4	5.8	13
ethylbenzene	136.2	5.8	−95

Unlike CO_2, the xylenes isomers are liquid at room temperature. While liquid phase ZLC is certainly possible, the set-up does add some complications. The hold-up in the fluid phase (amount of adsorbate retained in the fluid phase) becomes quite important, as it can be comparable or even greater than the hold-up in the adsorbed phase, reducing data sensitivity. For this reason, vapor-phase xylenes experiments were conducted, requiring the use of a bubbler. In this scenario, during equilibration, the purge gas is directed through a bubbler containing the liquid adsorbate. The

temperature and vapor-liquid equilibrium dictate the saturation pressure of the adsorbate, which can be predicted using semi-empirical correlations such as the Antoine equation.

Effective use of a bubbler thus demands precise control over liquid adsorbate temperature. The first adsorbate tested, *p*-xylene, proved to be challenging for this reason. The freezing point of *p*-xylene is 13 °C, so the bubbler temperature must be above that. Room temperature can vary as much as five degrees Celsius, which can lead to substantial variation in the initial stream concentration. Within the linear part of the isotherm, this is not a huge concern, because the material will have a proportional amount adsorbed regardless of the initial stream concentration. However, as mentioned, the differential enthalpies of adsorption are quite high for all four xylenes isomers, ranging from −63 ± 4 kJ/mol for ethylbenzene to −77 ± 6 kJ/mol for *o*-xylene in Co_2(dobdc).[25] Correspondingly, the linear part of the isotherm is at quite low pressures for all four adsorbates. For *p*-xylene, this region is physically inaccessible using a bubbler without stream dilution, as the vapor pressure just above the freezing point is 5 mbar,[27] well above framework saturation.[25]

Using a different xylene isomer with a lower freezing point allows for mitigation of stream concentration by going to lower bubbler temperatures. Of the isomers, *m*-xylene has the lowest freezing point (−47.9 °C) and the highest kinetic diameter (6.8 Å). I targeted this molecule for diffusion studies within the monodisperse Co_2(dobdc). While ZLC analysis is easier when the starting vapor pressure is within the linear regime of the isotherm, using the bubbler temperature to control this requires that the bubbler be kept around −42 °C or below. This proved difficult to achieve. Several cooling baths were attempted, including ethylene glycol/ethanol/dry ice and acetonitrile/dry ice. However, the mixtures are very hygroscopic and difficult to control. The baths only control the temperature within a few degrees, which led to unacceptable levels of concentration variation during equilibration. As a result, equilibration was done within a non-linear region of the isotherm, at 0 °C. As discussed in Chapter 1, with a non-linear isotherm, the initial drop in concentration is steeper, and the time to reach the linear asymptote is longer; nonetheless, under diffusional control, the limiting slope is the same. During desorption, as concentration goes from the initial amount adsorbed to zero, the concentration will at some point pass through the low-pressure region where quantity adsorbed is proportional to stream concentration. Thus, the long-time analysis method may still be used to extract diffusivity under equilibrium control.

The particularly strong binding of *m*-xylene within the material increases the difficulty of the measurements. Consider the non-dimensional parameter *L*:

$$L = \left(\frac{F}{\mathrm{K}V_s}\right)\left(\frac{l^2}{D}\right)$$

In using *m*-xylene as an adsorbate, I hoped to take advantage of a larger kinetic diameter to reach measurable diffusivities with micron-scale crystallites. However, the strong affinity of the molecules is also included in *L* within the equilibrium term: as the dimensionless Henry's law constant K goes up, the non-dimensional parameter *L* goes down, towards equilibrium control.

This has led to a very strong dependence on V_s, the volume of crystallites within the cell. If the sample included is too high in mass, it is impossible to reach kinetic control. The system has a stringent upper limit on the flow rate F, as above 40 mL/min the flame of the FID detector is extinguished. For particularly strong-binding adsorbates, the sample mass must be minimized.

For a comparison between long aspect ratio and short aspect ratio Co_2(dobdc), I used a microbalance to weigh out precise amounts of adsorbent: 0.19 mg in a 1/8" diameter machined

stainless steel cup. It takes significant manual dexterity to transfer this cup into the Swagelok ZLC cell without upending it and losing the sample. Further, as these materials are highly hydrophilic, both samples were methanol-exchanged and treated identically. Over time, the methanol is replaced with water, so mass measurements are done as quickly as possible. Previous thermogravimetric analysis done using this method found that this treatment led to repeatable activated sample mass and subsequent kinetics. The masses do not need to be identical, but the flow rate must be scaled to the mass, such that the ratio F/KV_s is constant between materials. The L value is then only a function of the controlled path length.

For the long-aspect ratio crystallites (characteristic length 2.5 microns), desorption rate increases with increasing flow rate (Fig. 4.16). The F×t plot indicates kinetic control, and the long-time asymptotes contain diffusional information (Fig. 4.17). Simultaneous regression on both flow rates yields a diffusivity of 3×10^{-14} m^2/s.

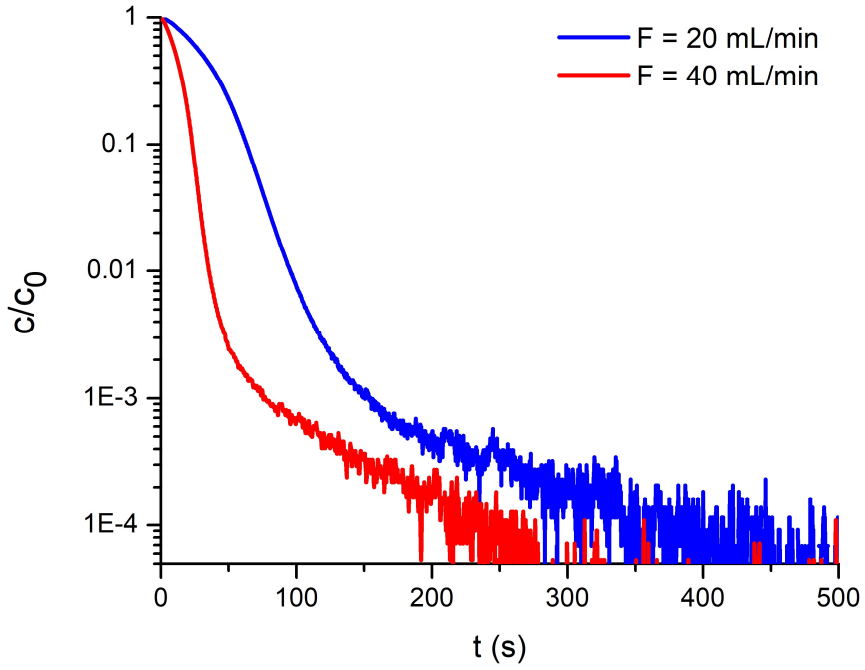

Figure 4.16. A comparison of desorption curves at different flow rates for long aspect ratio Co_2(dobdc) path length 2.5 microns.

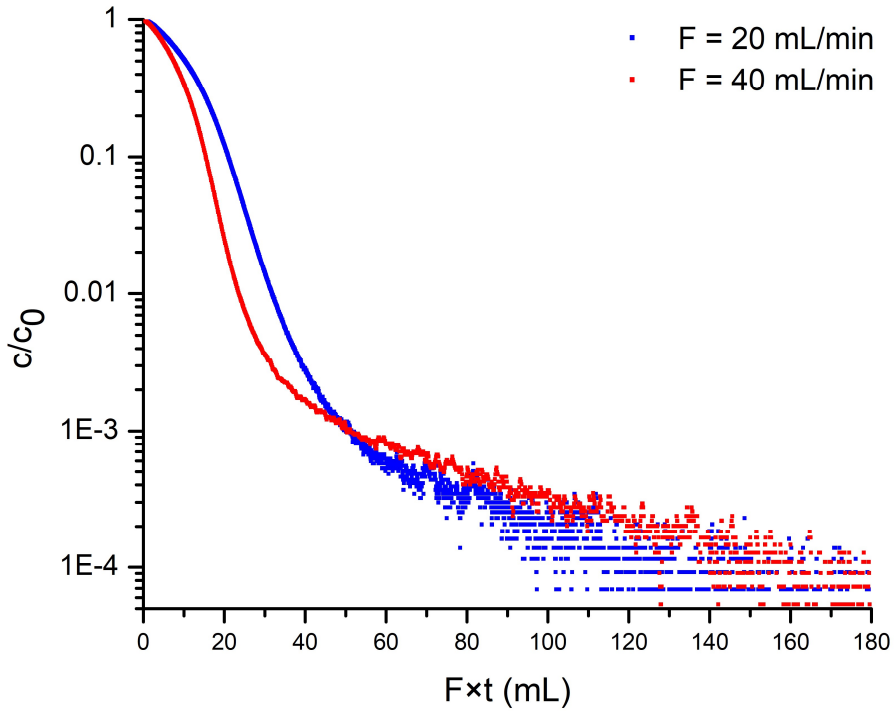

Figure 4.17. The volume-normalized F×t plot indicates diffusional control for high flow rates in the long aspect ratio Co_2(dobdc) crystallites, path length 2.5 microns.

A comparison under identical conditions (that is, the same F/KV_s) for the short aspect ratio crystallites instead indicates equilibrium control (Fig. 4.18 and Fig. 4.19). Shortening the path lengths by a factor of 5 has decreased the diffusional time constant by a factor of 25, such that I can no longer achieve kinetic control. This indicates that the short aspect ratio crystallites are better-suited for process use, as the material has equal selectivity but higher flux due to a decrease in diffusional path length.

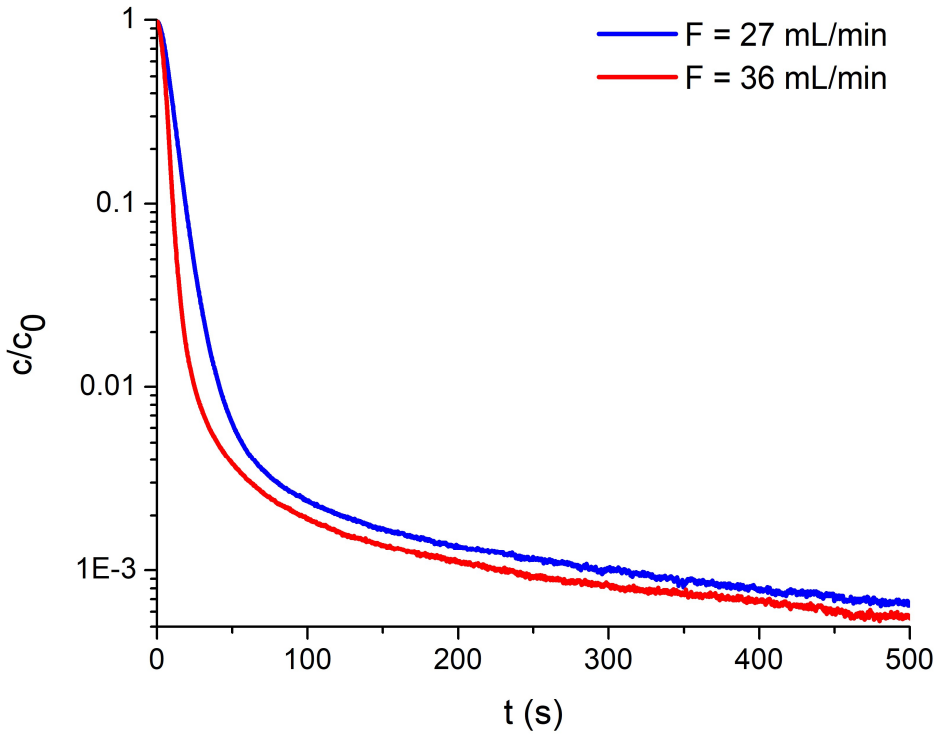

Figure 4.18. The desorption curves at high flow rates within the short aspect ratio Co_2(dobdc) have a steep drop-off due to the highly non-linear isotherm.

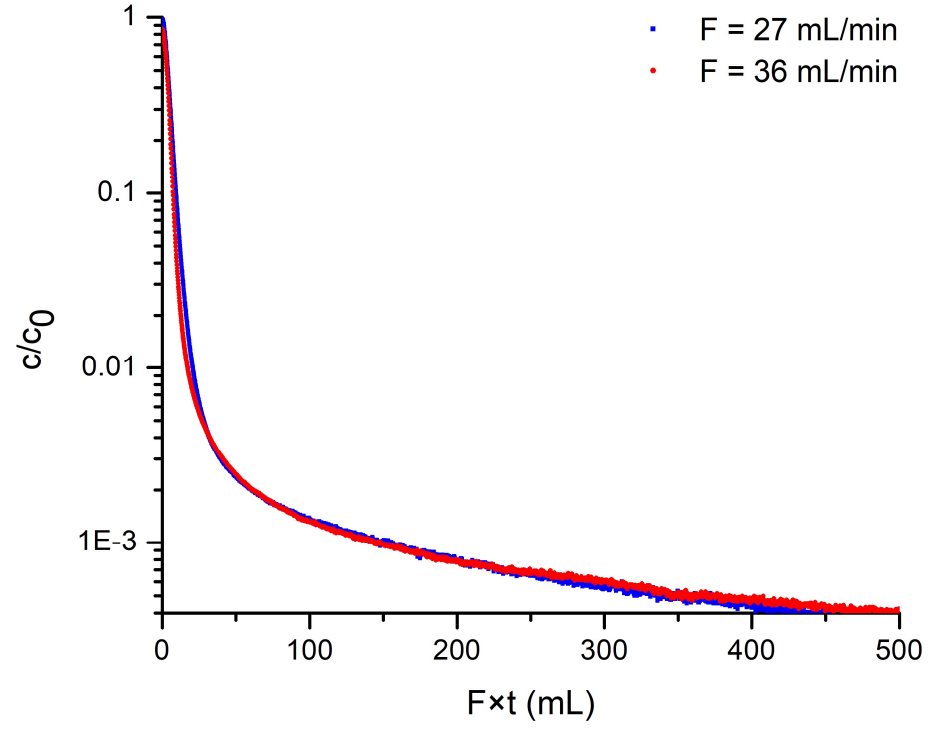

Figure 4.19. The F×t plot for the short aspect ratio crystallite under identical conditions indicates equilibrium control: diffusive limitations have been removed.

4.4 Conclusions and Outlook

Two different strategies for building a zero-length column chromatography instrument have been presented here. Retrofitting a gas chromatography instrument is a possible way to run ZLC measurements. In this case, care must be taken that flow rate is well-controlled, as it is the main differentiating test between equilibrium and kinetic regimes of analysis for desorption curves. Additional care must be taken to enforce the necessary thermal equilibration, or slow adsorbate/system interactions can introduce steady error into desorption curves. The designed system can measure both gas and vapor phase desorption experiments from room temperature up to 220 °C. For hydrocarbons, CO_2, and CO, the detection limit is less than 1 ppm, allowing for good signal for the calculation of limiting diffusivities.

Very large crystallites of Zn_2(dobdc) allow the measurement of CO_2 effective diffusivity within the pores. The D_0 value measured is lower than that measured on the same crystallites using PFG-NMR and additionally is lower than that simulated using molecular dynamics. The very small sample size and high flow rates rules out the encroachment of heat transfer effects. Instead, the lower effective diffusivity is likely to stem from surface resistances and defects. These barriers are not apparent from X-ray diffraction or surface area measurements.

Interestingly, this trend in diffusion constants across techniques is well-represented in the literature for zeolites, and similar conclusions about the encroachment of surface barriers have arisen. The defects and barriers in Zn_2(dobdc) here may be either native to the material or have developed through handling. Two potentially illuminating follow-up tests are suggested: the ZLC measurements could be redone with brand-new crystallites and tested over time, to see if barriers and defects are native or static. The PFG-NMR can also be extended with longer time intervals to test longer length scales. If there are surface barriers present, these longer length scales will lead more molecules to sample the surfaces and the measured diffusion should drop to become closer to the effective overall diffusivity measured via ZLC. The use of these techniques in parallel potentially utilizing different frameworks and adsorbates presents an intriguing way to study the presence of defects in metal–organic frameworks. In one-dimensional frameworks, even small amounts of pore blockages can introduce substantial diffusional resistances, which may or may not be obvious in equilibrium measurements.

The use of *m*-xylene as an adsorbate in Co_2(dobdc) may also be used to show the effect of increasing pore length through crystallization control. One substantial challenge in studying this adsorbate is how strong the binding is within the framework. As demonstrated in previous literature, *m*-xylene can bind to two different metal sites at once and has a correspondingly high binding enthalpy. Because the non-dimensional parameter L is a ratio of equilibrium to kinetics, having strongly bound species drives this parameter to equilibrium, making it harder to reach the kinetic regime. Very slight variations in the amount of adsorbent can change the apparent kinetics from minutes to hours. Despite these challenges, the longest monodisperse crystallites display kinetic control at high flow rates. Under analogous conditions of flow rate to crystal volume, the shortest aspect ratio crystallites are instead at equilibrium. In effect, shortening the path length has lowered the diffusional time constant to the point where diffusion no longer controls apparent kinetics. This is an important step towards process application, as it fulfills the desired goal set out at the beginning of this chapter: to maximize flux through the material without diminishing capacity. While there is no conclusive evidence yet of defects, as it has proved challenging to measure self-diffusion in Co_2(dobdc) using PFG-NMR due to the presence of paramagnetic Co^{2+},

there is correspondingly no definitive absence of defects. Certainly, any defects present could induce a lower effective diffusivity in the material.

Future work would most easily be done using gas-phase adsorbates that are slow-diffusing but weakly-bound and monodisperse crystallites. These can be challenging criteria to fulfill. In the first case study, the relatively fast diffusion of CO_2 within Zn_2(dobdc) required the synthesis of very large crystallites to enable measurement. The strong binding of *m*-xylene within the material presented its own challenge, as very small amounts of crystallites were required to get to kinetic regimes of measurement. Reducing the crystallite length is an effective tool for removing intracrystalline diffusion barriers, as the time constant is related to the square of the crystal length. Optimizing materials for application will thus require not only control over crystallization and resulting size and morphology but also understanding and control over defects and surface barriers, as these may play an inordinate role in controlling process sorption kinetics.

4.5 Acknowledgments

The work described in this chapter was supported by ExxonMobil Research and Engineering Company. The new custom-built ZLC instrument was designed in-house and purchased from SRI Instruments through the Center for Gas Separations Relevant to Clean Energy Technologies, an Energy Frontier Research Center funded by the US Department of Energy, Office of Science, Office of Basic Energy Sciences under award DE-SC0001015. I thank Miguel Gonzalez and Rebecca Siegelman for help retrofitting the gas chromatography instrument and Rodolfo Torres-Gavosto for assistance in running and debugging both instruments. I thank Peter Ravikovitch, Simon Weston and Joe Falkowski for the suggestion of using zero-length column chromatography and help with the technique. Additionally, I thank Alex Forse and Jeff Reimer for the PFG-NMR collaboration in the CO_2 diffusion work, and Sudi Jawahery and Berend Smit for molecular dynamics simulations of the same.

4.6 References and Supplementary Figures

(1) Kärger, J.; Vasenkov, S.; Auerbach, S. M. *Handbook of Zeolite Science and Technology*; 2003.
(2) Davis, M. E. *Ind. Eng. Chem. Res* **1991**, *30*, 34.
(3) Ruthven, D. M. *Principles of Adsorption and Adsorption Processes*; Wiley, 1984.
(4) Eic, M.; Ruthven, D. M. *Zeolites* **1988**, *8*, 40.
(5) Sholl, D. S.; Lively, R. P. *Nature* **2016**, *532* 435.
(6) Canivet, J.; Fateeva, A.; Guo, Y.; Coasne, B.; Farrusseng, D. *Chem. Soc. Rev.* **2014***, 43,* 5594.
(7) Kärger, J.; Ruthven, D. M.; Theodorou, D. N. *Diffusion in Nanoporous Materials*; Weinheim, Germany, 2012.
(8) Ismail, A. F.; Khulbe, K. C.; Matsuura, T. *Gas Separation Membranes: Polymeric and Inorganic*; Springer International Publishing: Cham, 2015.
(9) Matteucci, S.; Yampolskii, Y.; Freeman, B. D.; Pinnau, I. Transport of Gases and Vapors in Glassy and Rubbery Polymers. In *Materials Science of Membranes for Gas and Vapor Separation*; John Wiley & Sons, Ltd: Chichester, UK, 2006.
(10) Haldoupis, E.; Nair, S.; Sholl, D. S. *J. Am. Chem. Soc.* **2010**, *132*, 7528.
(11) Bu, L.; Nimlos, M. R.; Robichaud, D. J.; Kim, S. *J. Phys. Chem. C* **2017**, *121*, 500.

(12) Li, Y.; Wang, X.; Xu, D.; Chung, J. D.; Kaviany, M.; Huang, B. *J. Phys. Chem. C* **2015**, *119*, 13021.
(13) *Practical Gas Chromatography*; Dettmer-Wilde, K., Engewald, W., Eds.; Springer Berlin Heidelberg: Berlin, Heidelberg, 2014.
(14) Brandani, S. *Chem. Eng. Technol.* **2016**, *39*, 1194.
(15) Forse, A. C.; Altobelli, S. A.; Benders, S.; Conradi, M. S.; Reimer, J. A. *J. Phys. Chem. C* **2018**, *122*, 15344.
(16) Forse, A. C.; Gonzalez, M. I.; Siegelman, R. L.; Witherspoon, V. J.; Jawahery, S.; Mercado, R.; Milner, P. J.; Martell, J. D.; Smit, B.; Blümich, B.; Long, J. R.; Reimer, J. A. *J. Am. Chem. Soc.* **2018**, *140*, 1663.
(17) Hu, X.; Brandani, S.; Benin, A. I.; Willis, R. R. *Ind. Eng. Chem. Res.* **2015**, *54*, 6772.
(18) Queen, W. L.; Hudson, M. R.; Bloch, E. D.; Mason, J. A.; Gonzalez, M. I.; Lee, J. S.; Gygi, D.; Howe, J. D.; Lee, K.; Darwish, T. A.; James, M.; Peterson, V. K.; Teat, S. J.; Smit, B.; Neaton, J. B.; Long, J. R.; Brown, C. M. *Chem. Sci.* **2014**, *5*, 4569.
(19) Loos, J.-B. B. W. P.; Verheijen, P. J. T.; Moulijn, J. A. *Chem. Eng. Sci.* **2000**, *55*, 51.
(20) Duncan, W. L.; Möller, K. P. *Chem. Eng. Sci.* **2002**, *57*, 2641.
(21) Cavalcante, C. L.; Brandani, S.; Ruthven, D. M. *Zeolites* **1997**, *18*, 282.
(22) Crank, J. The Mathematics of Diffusion, Second Edition. *Oxford Univ. Press* **1975**.
(23) Brandani, S.; Jama, M. A.; Ruthven, D. M. *Chem. Eng. Sci.* **2000**, *55* (7), 1205.
(24) *Ullmann's Encyclopedia of Industrial Chemistry*; Wiley, 2000.
(25) Gonzalez, M. I.; Kapelewski, M. T.; Bloch, E. D.; Milner, P. J.; Reed, D. A.; Hudson, M. R.; Mason, J. A.; Barin, G.; Brown, C. M.; Long, J. R. *J. Am. Chem. Soc.* **2018**, *140*, 3412.
(26) Li, J.-R.; Kuppler, R. J.; Zhou, H.-C. *Chem. Soc. Rev.* **2009**, *38*, 1477.
(27) Osborn, A. G.; Douslin, D. R. *J. Chem. Eng. Data* **1974**, *19* (2), 114.

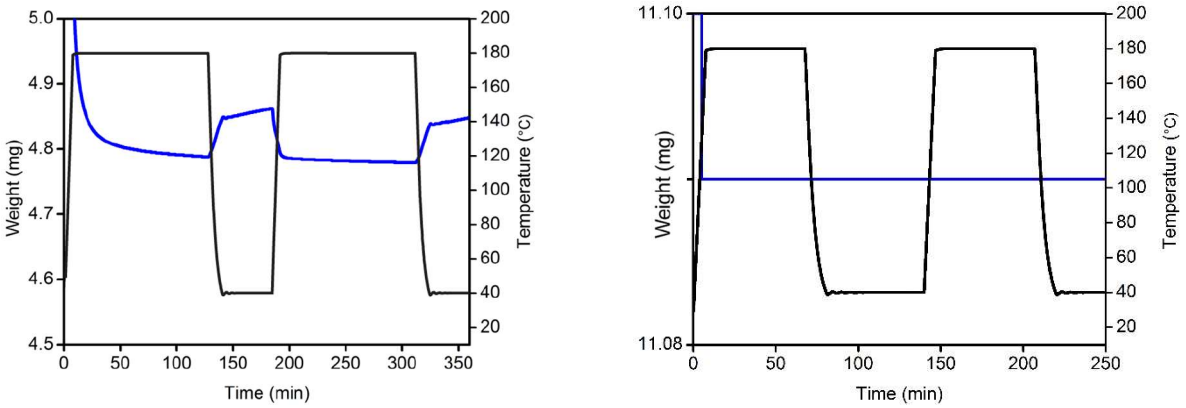

Figure 4.S1. At left, Co_2(dobdc) cycled between 40 °C and 180 °C under nitrogen; at right, PVDF. The Co_2(dobdc) particles increase weight during cooling under nitrogen, while the PVDF sample (and indeed a bare pan) does not.

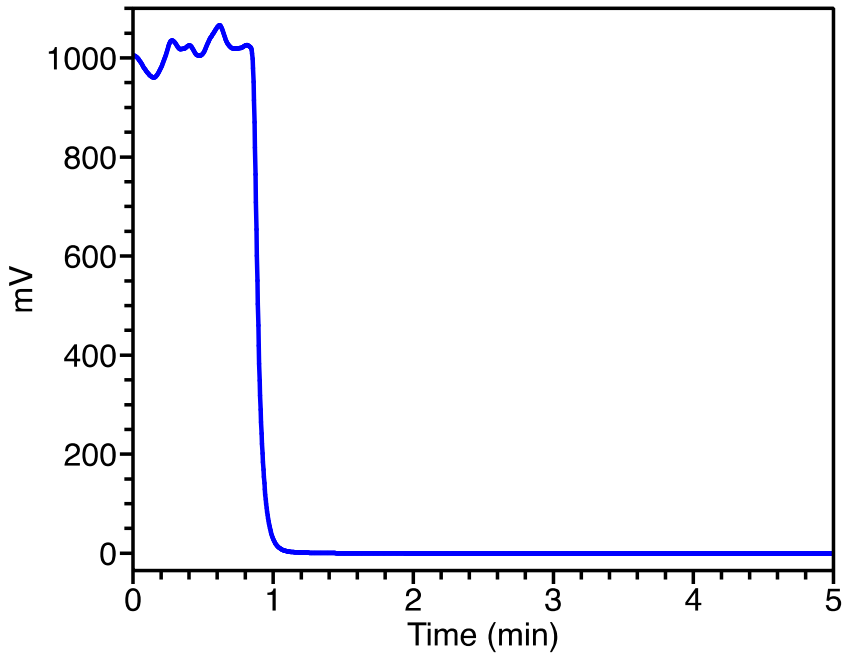

Figure 4.S2. TCD desorption response (from equilibrated CO_2/He to pure He) at 40 °C with a flow rate of 10 mL/min for a blank cell.

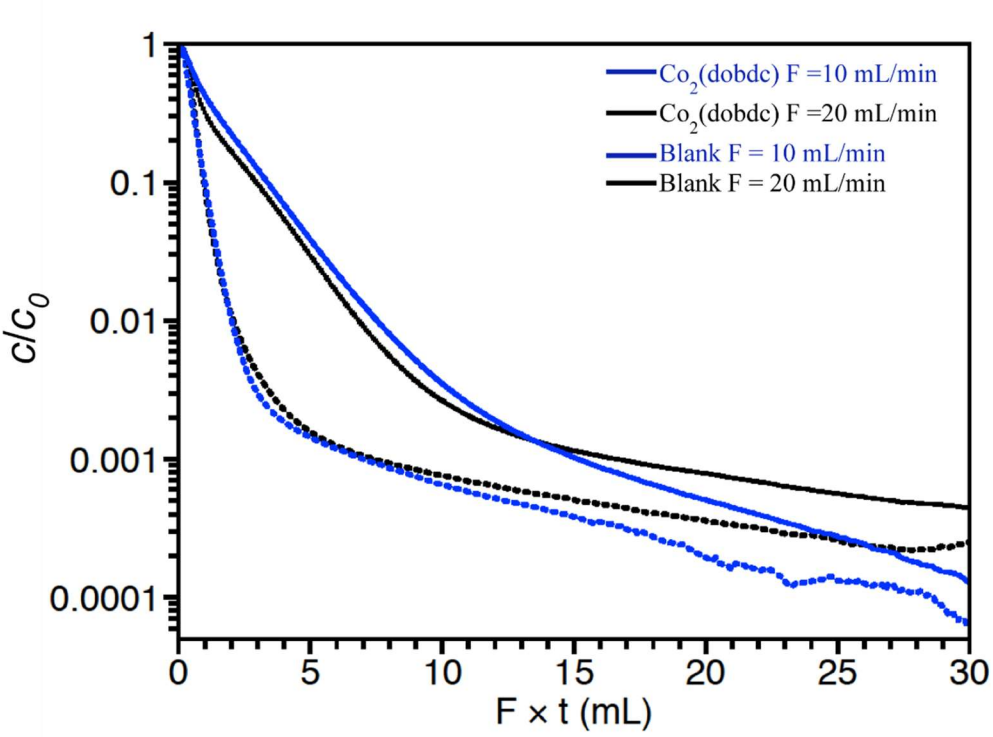

Figure 4.S3. Desorption of CO_2 from Co_2(dobdc) at different flow rates, plotted as a function of gas volume passed through the cell.

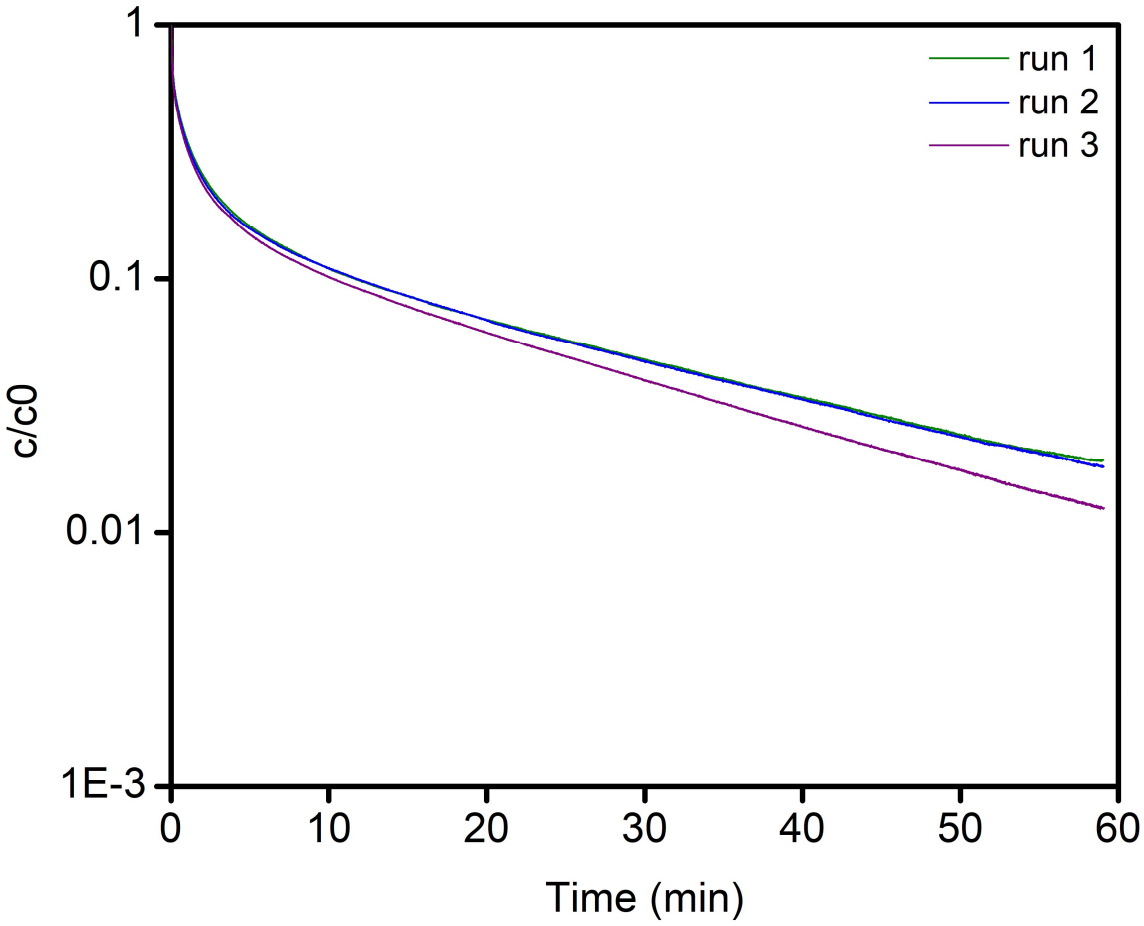

Figure 4.S4. This set at F = 20 ml/min and T = 140 °C is a huge improvement, after many major fixes. However, a variation in the flow rate has led the flow rate in run 3 to be slightly higher, leading to a higher initial concentration and resultant lower scaled curve.

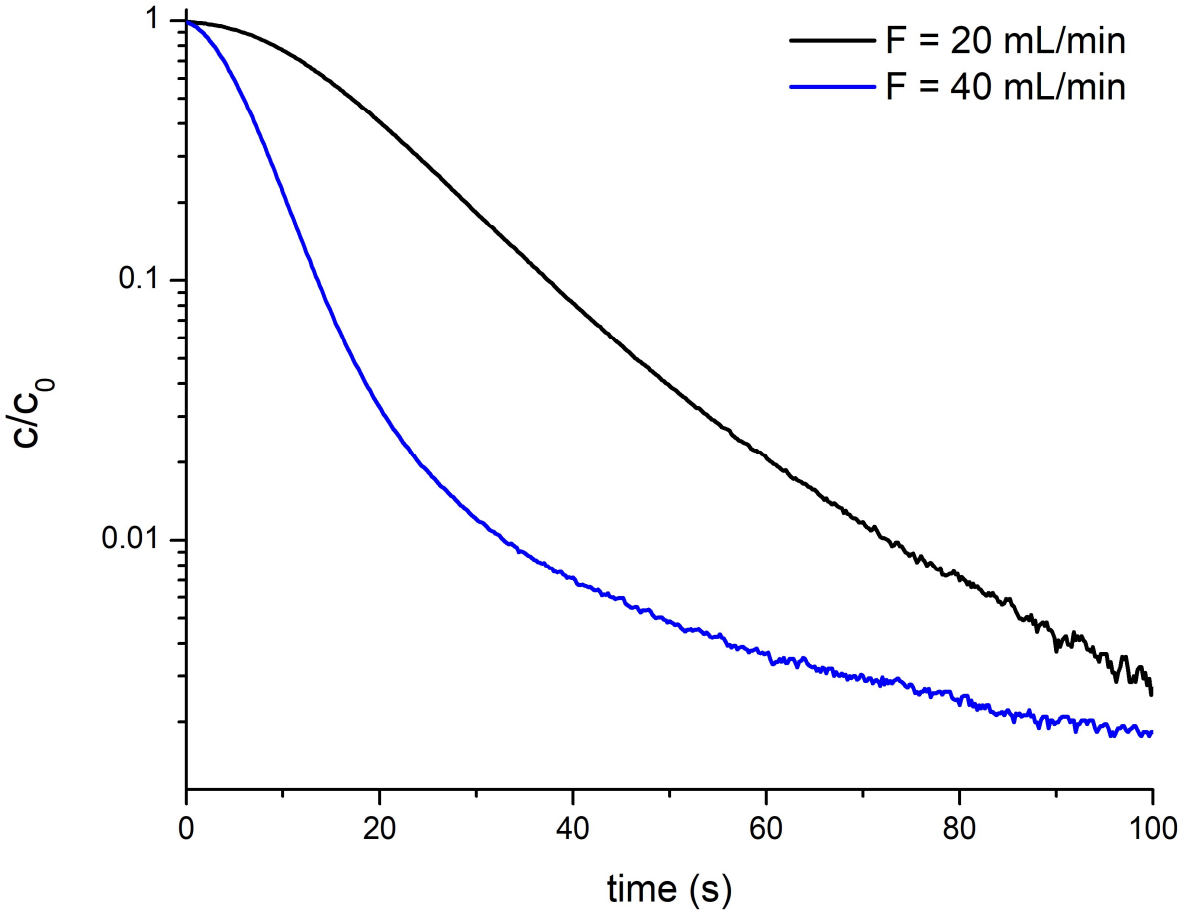

Figure 4.S5. Desorption curves for CO_2 in Zn_2(dobdc) as a function of flow rate. Overall curve is faster for the higher flow rate.